SEISMIC WAVE ANALYSIS GROUP

Tariq Alkhalifah, Sergey Fomel, Xuxin Ma, Christos Saragiotis, and Paul Sava

Selected papers

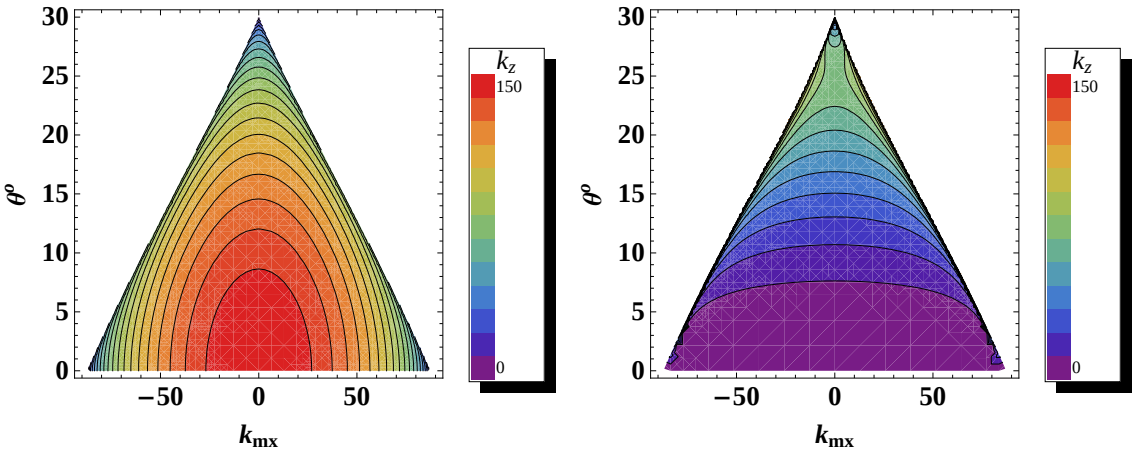

Copyright © 2012-13

by KAUST

SWAG — TABLE OF CONTENTS

Tariq Alkhalifah, Traveltime approximations for transversely isotropic media with an inhomogeneous background 1

Tariq Alkhalifah and Sergey Fomel, Angle gathers in wave-equation imaging for transversely isotropic media 27

Tariq Alkhalifah and Paul Sava, A transversely isotropic medium with a tilted symmetry axis normal to the reflector 43

Tariq Alkhalifah, Acoustic wavefield evolution as function of source location perturbation 57

Tariq Alkhalifah and Sergey Fomel, An eikonal based formulation for traveltime perturbation with respect to the source location 73

Xuxin Ma and Tariq Alkhalifah, Wavefield extrapolation in pseudodepth domain 89

Christos Saragiotis, Tariq Alkhalifah, and Sergey Fomel, Automatic traveltime picking using the instantaneous traveltime 109

Traveltime approximations for transversely isotropic media with an inhomogeneous background

Tariq Alkhalifah[1]

ABSTRACT

A transversely isotropic model with a tilted symmetry axis (TI) is regarded as one of the most effective approximations to the Earth subsurface, especially for imaging purposes. However, we commonly utilize this model by setting the axis of symmetry normal to the reflector. This assumption may be accurate in many places, but deviations from this assumption will cause errors in the wavefield description. Using perturbation theory and Taylor's series, I expand the solutions of the eikonal equation for 2D transversely isotropic media with respect to the independent parameter θ, the angle the tilt of the axis of symmetry makes with the vertical, in a generally inhomogeneous TI background with a vertical axis of symmetry (VTI). I do an additional expansion in terms of the independent (anellipticity) parameter η in a generally inhomogeneous elliptically anisotropic background medium. These new TI traveltime solutions are given by expansions in η and θ with coefficients extracted from solving linear first-order partial differential equations. Pade approximations are used to enhance the accuracy of the representation by predicting the behavior of the higher-order terms of the expansion. A simplification of the expansion for homogenous media provides nonhyperbolic moveout descriptions of the traveltime for TI models that are more accurate than other recently derived approximations. In addition, for 3D media, I develop traveltime approximations using Taylor's series type of expansions in the azimuth of the axis of symmetry. The coefficients of all these expansions can also provide us with the medium sensitivity gradients (Jacobian) for nonlinear tomographic-based inversion for the tilt in the symmetry axis.

[1]**e-mail:** tariq.alkhalifah@kaust.edu.sa

INTRODUCTION

The nature of sedimentation and thin layering in the Earth subsurface induces wave propagation characteristics that can be better described by considering the medium to be anisotropic. Specifically, since the layering has a general preferred direction, we find that the transversely isotropic (TI) assumption to be the most practical type of anisotropy to represent big parts of the subsurface. The tilt in this case is naturally set in the direction normal to the layering (Alkhalifah and Bednar, 2000; Audebert et al., 2006; Behera and Tsvankin, 2009; Alkhalifah and Sava, 2010). Thus, this type of model approximates a big portion of the anisotropy resulting from the thin layering. Developing simple traveltime formulations for such a model helps in many applications, including traveltime tomography and integral-based Kirchhoff imaging. The vertical symmetry axis (VTI) medium is a special case of TI in which the symmetry axis is normal to the typically horizontal acquisition surface, and thus results in simpler formulations.

Traveltimes are conventionally evaluated by solving a nonlinear partial differential equation (PDE), better known as the eikonal equation. Among the most known methods for solving this equation are ray tracing and the finite-difference approximations. Finite-difference solutions of the eikonal equation have been recognized as one of the most efficient means of traveltime calculations (Vidale, 1990; van Trier and Symes, 1991; Popovici, 1991; Alkhalifah and Fomel, 2001). Some of main advantages of this method in comparison to ray tracing include the ability to directly provide solutions on regular grids, a complete coverage of the solution space, and a high numerical robustness. On the down side, finite-difference based solutions typically include only the first arrivals, which might not be even the most energetic ones (Cerveny, 2001). In anisotropic media, traveltime computation is dependent on more than one parameter field. However, through careful parametrization of the TI medium, P-wave traveltimes in 3D, under the acoustic assumption, become dependent on only three parameter fields and two angles. These parameters include the tilt-direction velocity, v_t, the normal-moveout equivalent velocity, $v = v_t\sqrt{1+2\delta}$ [where δ corresponds to the symmetry direction (Tsvankin, 1997)], and the anellipticity parameter $\eta = \frac{\epsilon-\delta}{1+2\delta}$ (with ϵ also defined with respect to the symmetry direction). This is evident in the eikonal equation for TI media developed by Alkhalifah (1998, 2000a). If the symmetry axis is not vertical, two additional parameters are needed to describe the tilt in 3D, the angle θ that the symmetry axis makes with the vertical and the azimuth ϕ of the vertical symmetry-axis plane with respect the x-axis [Tsvankin (1997)].

The process of finding a stable solution for the TI (or even the VTI) eikonal equation using finite-difference schemes is generally hard, especially since such a process requires finding the root of a quartic equation at each computational step (Wang et al., 2006). However, traveltime computation for a slightly more simplified, but not practical, elliptically anisotropic model is far more efficient. The reason for the high efficiency is that elliptical anisotropy has the same order of complexity (nonlinearity) in the eikonal equation as does the isotropic equation. Thus, though elliptical anisotropy represents an uncommon model in practice, it provides some flexibility in

treating the difference between vertical and horizontal velocities, or in other words, the flexibility of stretching the depth axis to obtain accurate reflection depths in imaging (Peng and Steenson, 2001; Ball, 1995; Ohlsen and MacBeth, 1999). However, elliptical anisotropy does not provide accurate focusing for media of typical non-elliptical TI anisotropy (Alkhalifah and Larner, 1994). It will be used here however as the background medium for the perturbation expansions.

The forward problem, whether it is traveltime calculation or wavefield modeling, is a major component of the inversion process. If we model wavefields, we can use those wavefields to generate synthetic data and compare them with measured data as part of what we refer to as wavefield inversion. Likewise, forward traveltime calculation is used to measure the traveltime misfit with those extracted from the data in what is referred to as traveltime tomography. If we assume that one or two of the parameters are constant, the gradient of the objective function with respect to these parameters can be calculated analytically and that usually helps the inversion process. In this paper, I develop simplified formulations for traveltime calculation that can help in resolving anisotropy parameters, specifically the tilt angle.

Alkhalifah (2010) developed an eikonal-based scanning scheme to search for the anisotropy parameter η that can provide the best traveltime fit to the data in a general inhomogeneous background medium. In this earlier paper, I derived first-order linear partial differential equations (PDEs) governing the coefficients of expanding the traveltime solution for VTI media in terms of the independent parameter η from a background elliptical anisotropic model. I use the Shanks transform [Bender and Orszag (1978)] to enhance the accuracy of the expansion to a point in which the homogeneous-medium versions of it provided exceptional accuracy in describing the traveltime compared to other well-known published moveout equations (Alkhalifah, 2000b). I also suggested a simple angle transformation to make the method work for a tilted symmetry axis with a known tilt direction (i.e. in the direction normal to the layering). However, if the tilt direction is unknown, the η estimation will certainly suffer from this limitation.

In this paper, I derive multi-parameter expansions of traveltime as a function of the symmetry-axis angles and η with coefficients estimated using linearized forms of the eikonal equation. The accuracy of such an expansion is again further enhanced using Shanks transform and Pade approximations to obtain higher-order representation. I use a homogeneous-background medium version of the approximation to test its accuracy and then examine the 3D case where the axis direction is described by azimuth as well.

THE TI EIKONAL AND EXPANSION IN θ

In VTI media, the eikonal equation (Alkhalifah, 1998) in the acoustic approximation has the form:

$$v^2(1+2\eta)\left(\left(\frac{\partial\tau}{\partial x}\right)^2+\left(\frac{\partial\tau}{\partial y}\right)^2\right)+{v_t}^2\left(\frac{\partial\tau}{\partial z}\right)^2\left(1-2\eta v^2\left(\left(\frac{\partial\tau}{\partial x}\right)^2+\left(\frac{\partial\tau}{\partial y}\right)^2\right)\right)=1, \quad (1)$$

where $\tau(x,y,z)$ is the traveltime (eikonal) measured from the source to a point with the coordinates (x,y,z), and v_t and v are the velocity and NMO velocity ($=v_t\sqrt{1+2\delta}$), respectively, described with respect to the symmetry direction at that point. To formulate a well-posed initial-value problem for equation 1, it is sufficient to specify τ at some closed surface and to choose one of the two solutions: the wave going from or toward the source. The level of nonlinearity in this quartic (in terms of τ) equation is higher than that for the isotropic or elliptically anisotropic eikonal equations. This results in much more complicated finite-difference approximations of the VTI eikonal equation.

For a tilted TI medium, the traveltime derivatives in equation 1 are taken with respect to the tilt direction, and thus, we have to rotate the derivatives in equation 1 using the following Jacobian in 3D:

$$\begin{pmatrix} \cos\phi\cos\theta & \sin\phi\cos\theta & \sin\theta \\ -\sin\phi & \cos\phi & 0 \\ -\cos\phi\sin\theta & -\sin\phi\sin\theta & \cos\theta \end{pmatrix}, \quad (2)$$

to obtain an eikonal equation corresponding to the conventional computational coordinates governed by the acquisition surface. In equation 2, θ is the angle of the symmetry axis measured from the vertical and ϕ corresponds to the azimuth of the vertical plane that contains the symmetry axis measured from the x-axis (the axis of the source-receiver direction). Setting initially ϕ=0, for simplicity, allows us to obtain the eikonal equation for 2D TI media given by:

$$\begin{aligned} &v^2(1+2\eta)\left(\cos\theta\frac{\partial\tau}{\partial x}+\sin\theta\frac{\partial\tau}{\partial z}\right)^2+ \\ &{v_t}^2\left(\cos\theta\frac{\partial\tau}{\partial z}-\sin\theta\frac{\partial\tau}{\partial x}\right)^2\left(1-2\eta v^2\left(\cos\theta\frac{\partial\tau}{\partial x}+\sin\theta\frac{\partial\tau}{\partial z}\right)^2\right)=1. \end{aligned} \quad (3)$$

The full 3D version of this equation is stated in Appendix D.

Solving equation 3 numerically requires solving a quartic equation (instead of the quadratic in the isotropic and elliptical anisotropic case) at each computational step. Alternatively, it can be solved using perturbation theory (Bender and Orszag, 1978) by approximating equation 3 with a series of simpler linear equations. Considering θ constant and small, we can represent the traveltime solution as a series expansion in θ. This will result in a solution that is globally representative in the space domain

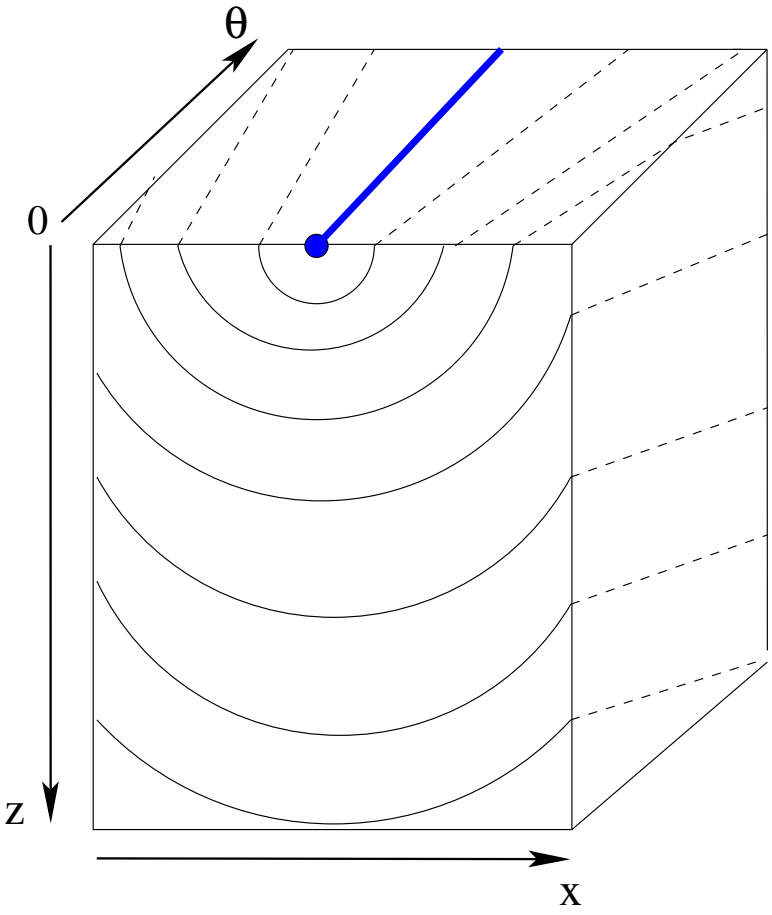

Figure 1: A schematic plot showing the relation between a background traveltime field for θ=0 and that when θ is larger than zero. The round dot at the top of the $\theta = 0$ plane represents a source. thetaScan/XFig scanTheta

and, despite the approximation of small θ, the accuracy for even large θ, as we will see later, is high. The constant-θ assumption assumes a factorized medium (Alkhalifah, 1995) in θ (useful for smooth θ estimation applications). However, all other velocities and parameters including v_t, v (or δ) and η are allowed to vary. Figure 1 illustrates the concept of the global expansion as we predict the traveltime for any θ from its behavior at $\theta = 0$ for the full traveltime field using, in this case, a quadratic approximation. Specifically, we substitute the following trial solution,

$$\tau(x,z) \approx \tau_0(x,z) + \tau_1(x,z)\sin\theta + \tau_2(x,z)\sin^2\theta, \tag{4}$$

where τ_0, τ_1, and τ_2 are coefficients of the expansion with dimensions of traveltime, into the eikonal equation 3. For practical purposes, I consider here only three terms of the expansion. As a result (as shown in Appendix A), τ_0 satisfies the eikonal equation for VTI anisotropy, while τ_1 and τ_2 satisfy linear first-order partial differential equations having the following general form (see Appendix A):

$$v^2(1+2\eta)\frac{\partial\tau_0}{\partial x}\frac{\partial\tau_i}{\partial x} + {v_t}^2\frac{\partial\tau_0}{\partial z}\frac{\partial\tau_i}{\partial z} - 2\eta v^2 v_t^2\frac{\partial\tau_0}{\partial z}\frac{\partial\tau_0}{\partial x}\left(\frac{\partial\tau_0}{\partial z}\frac{\partial\tau_i}{\partial x} + \frac{\partial\tau_0}{\partial x}\frac{\partial\tau_i}{\partial z}\right) = f_i(x,z), \tag{5}$$

with $i = 1, 2$. The functions $f_i(x,z)$ get more complicated for larger i and depend on terms that can be evaluated only sequentially. Therefore, these linear partial differential equations must be solved in the order of increasing i starting with $i = 1$.

EXPANSION IN TERMS OF θ AND η

Though the expansion in terms of θ in the previous section allowed us to estimate traveltimes for a tilted symmetry axis, it also required that we solve the eikonal equation for a VTI medium, which is relatively challenging. For inversion purposes, it also required knowledge of η, which might not be possible in TI media using initially a VTI approximation, especially if the tilt is large. However, an expansion in η, in addition to θ (from their zero values), will result in an elliptically anisotropic background medium and it will allow us to search for both η and θ, simultaneously, considering that the elliptical anisotropy model is known.

The two-parameter expansion can be obtained by substituting the following trial solution:

$$\tau(x,z) \approx \tau_0(x,z)+\tau_\eta(x,z)\eta+\tau_\theta(x,z)\sin\theta+\tau_{\eta_2}(x,z)\eta^2+\tau_{\eta\theta}(x,z)\eta\sin\theta+\tau_{\theta_2}(x,z)\sin^2\theta \tag{6}$$

into equation 3 resulting in linear first-order partial differential equations having the following general form:

$$v_t^2\frac{\partial\tau_0}{\partial z}\frac{\partial\tau_i}{\partial z} + v^2\frac{\partial\tau_0}{\partial x}\frac{\partial\tau_i}{\partial x} = f_i(x,z), \tag{7}$$

with $i = \eta, \theta, \eta_2, \eta\theta, \theta_2$, and τ_0 satisfies the eikonal equation for an elliptical anisotropic background model. Again, the function $f_i(x,z)$ gets more complicated for i corresponding to the second-order term and it depends on terms for the first order and

background medium solutions. Therefore, these linear partial differential equations also must be solved in succession starting with $i = \eta$ and $i = \theta$. As soon as the τ_η, and τ_{η_2} coefficients are evaluated, they can be used, as Alkhalifah (2010) showed, to estimate the traveltime using the first-sequence of Shanks transform (Bender and Orszag, 1978), and as shown in Appendix B, has the form:

$$\tau(x,z) \approx \tau_0(x,z)+\tau_\theta(x,z)\sin\theta+\tau_{\theta_2}(x,z)\sin^2\theta+\frac{\eta\left(\tau_\eta(x,z)+\tau_{\eta\theta}(x,z)\sin\theta\right)^2}{\tau_\eta(x,z)+\tau_{\eta\theta}(x,z)\sin\theta-\eta\tau_{\eta_2}(x,z)}. \tag{8}$$

The θ expansion does not adapt well to the Shanks transform requirements for predicting the behavior of the higher-order terms in θ. In this case, the second-order approximation in the θ expansion is sufficient.

For η and θ scan applications, the coefficients (τ_0, τ_η, τ_θ, τ_{η_2}, $\tau_{\eta\theta}$, and τ_{θ_2}) need to be evaluated only once and can be used with equation 8 to search for the best traveltime fit to those traveltimes extracted from the data.

A HOMOGENEOUS MODEL TEST

Though the equations above are developed for a general inhomogeneous background medium, I examine their accuracy in representing TI traveltime and traveltime moveout in the homogeneous case. This is convenient since most parameter scan-type applications (i.e. semblance velocity analysis) are performed considering an effective homogeneous medium.

As shown in Appendix C, I use the simple traveltime relation for an elliptically anisotropic homogeneous background to recursively solve for the coefficients of the traveltime expansion in θ and η, and thus, obtain analytical representations for coefficients τ_0, τ_θ, τ_η, τ_{θ_2}, τ_{η_2}, and $\tau_{\eta\theta}$. Setting $\eta = 0$, to allow for a simplified presentation, I obtain an analytical representation of traveltime for tilted elliptical anisotropy given by

$$\tau(x,z) = \sqrt{\frac{x^2}{v^2}+\frac{z^2}{v_t^2}}\left(1+\frac{(v_t^2-v^2)\,xz\sin\theta}{v^2z^2+v_t^2x^2}+\right.$$
$$\left.\frac{\sin^2\theta\left(-v^4z^4+v^2v_t^2\left(x^4+z^4\right)-v_t^4x^4\right)}{2\left(v^2z^2+v_t^2x^2\right)^2}\right), \tag{9}$$

where the source is located at $x = 0$ and $z = 0$.

This formula type (equation 9) basically represents a moveout equation for traveltime in TI media as a function of offset (or x) and can be compared with equations developed explicitly to represent the moveout in TI media. Pech et al. (2003) derived the exact quartic moveout coefficient (i.e., the fourth-order term of the Taylor series expansion for squared traveltime) for pure (nonconverted) reflections in arbitrarily anisotropic, heterogeneous media. They also linearized the P-wave quartic coefficient

in the anisotropy parameters for homogeneous tilted TI media above a horizontal and dipping reflector. For a horizontal TI layer, the P-wave fourth-order Taylor series with linearized expressions for both the NMO velocity (Grechka and Tsvankin, 2000) and the quartic coefficient (Pech et al., 2003) is given by:

$$t^2(X) = t_0^2 + \frac{\left(1 - 2\delta + 2\epsilon \sin^2\theta - 14(\epsilon - \delta)\sin^2\theta\cos^2\theta\right)}{v_t^2} X^2 + A_4 X^4, \tag{10}$$

where

$$A_4 = -\frac{2\eta\cos^4\theta}{v_t^4 t_0^2}, \tag{11}$$

t_0 is the two-way zero-offset time and X is the offset ($= 2x$). For zero tilt, it reduces to

$$t^2(X, \theta = 0) = t_0^2 + \frac{(1 - 2\delta)}{v_t^2} X^2 - \frac{2\eta}{v_t^4 t_0^2} X^4, \tag{12}$$

which reveals the additional approximation involved in this equation as even the second-order term is linearized with respect to δ. Meanwhile, setting $\theta = 0$ in equation 9 yields an accurate description of the second-order term of the moveout with the NMO velocity in the denominator instead.

Grechka and Pech (2006) suggested rewriting equation 10 in the following form:

$$t^2(X) = t_0^2 + \frac{\left(1 - 2\delta + 2\epsilon \sin^2\theta - 14(\epsilon - \delta)\sin^2\theta\cos^2\theta\right)}{v_t^2} X^2 + \frac{2\eta A_4}{2\eta - v^2(1 + 2\eta)A_4 X^2} X^4, \tag{13}$$

which typically provides higher-order accuracy as the additional offset component in the denominator of the fourth-order term tends to predict the behavior at very large offsets.

Sena (1991) presented an anisotropic approximation of the group velocity as a function of symmetry angle. These velocities can serve to obtain moveout equations as well, and they are given by

$$t(X) = \frac{\sqrt{X^2 + 4z^2}\sqrt{2(\delta - \epsilon)\sin^4(\theta - \psi) - 2\delta\sin^2(\theta - \psi) + 1}}{v_t}, \tag{14}$$

where the ray angle, ψ, satisfies

$$\psi = \tan^{-1}\left(\frac{X}{2z}\right). \tag{15}$$

Using an elliptical anisotropic background model with axis-direction velocity equal to 2 km/s velocity, $\delta = 0.2$, and tilt angle θ=20°, I compare the traveltime errors of the moveout equations extracted from our eikonal based formulations with those that are used for pure moveout approximations, equations 13 and 14. For a reflector at

Figure 2: The relative traveltime error as a function of offset for an elliptically anisotropic model with v=2 km/s, $\delta = 0.2$, $\theta = 20^0$, and a reflector depth z=2 km for the new expansion in θ (solid black curve), the nonhyperbolic moveout equation 10 (solid gray curve), and for the Sena approximation (dashed black curve). thetaScan/Math errTEll3f

depth z=2 km, Figure 2 shows the percentage traveltime errors as a function of offset for the equations given above. Clearly, equations 13 and 14, given by the solid grey and dashed curves, respectively, are less accurate in describing the traveltime behavior overall than the new formula (solid black curve), equation 9. The moveout equations have faired well for the vertical direction but performed poorly for larger offset.

Moreover, for a more practical case of TI, in which η=0.2, the errors, as shown in Figure 3, are smaller overall for the new equation (solid black curve) than the other approximations. Despite the larger error of our approximation near vertical, the departure of the other approximations from the accurate value at large offset reflect their near-offset based expansion. In the new equation, the expansion is with respect to small tilt, and thus, has an unbiased representation of the traveltime with respect to offset. As a result, the accuracy of the new equation is higher over all.

Figure 3: The relative traveltime error as a function of offset for a model with v=2 km/s, η=0.2, $\theta = 20^0$, and a reflector depth z=2 km for the new expansion in θ (solid black curve), the nonhyperbolic moveout equation 10 (dashed gray curve), and 13 (solid gray curve) and for Sena's approximation (dashed black curve). thetaScan/Math errTTI3fNew

The analytical equations developed in this section were meant to test the accuracy of the perturbation theory approximations applied to the eikonal equation. Though they show high accuracy in representing the moveout, the general perturbation formulations are not meant to be only used as an alternative to other available

equations derived for the homogeneous case. Their perturbation from a background inhomogeneous model allows us to predict traveltime in more complex media.

THE VERTICAL DIRECTION

The vertical direction in the conventional seismic experiment is critical as the depth mistie (or vertical velocity) and the NMO velocity are typically measured with respect to the vertical direction regardless of the tilt in the symmetry angle. Specifically, the vertical velocity is extracted from the well check shots (typically vertical) and the moveout velocity given by the second derivative of traveltime with respect to phase angle, is measured in the vertical direction ($x = 0$). Setting $x = 0$ in equation 9, and considering the two-way traveltime, $t = 2\tau$, yields the following relation for the traveltime in the vertical direction:

$$t(x=0,z) = 2\frac{z}{v_t}\left(1 - \frac{1}{2}\sin^2\theta\left(1 - \frac{v_t^2}{v^2}\right)\right), \tag{16}$$

which includes terms related to the symmetry-axis direction. From Figure 2 we can see how well this approximation predicted the vertical traveltime. This equation is convenient to use along with well information to predict the velocities along the symmetry axis. Actually, for $\eta \neq 0$ (anelliptic TI media), applying Pade approximations (Bender and Orszag, 1978) to the η and $\sin\theta$ expansions, yields the following relation for traveltime in the vertical direction:

$$t(x=0,z) = 2\frac{z}{v_t}\frac{v^2}{v^2 + \frac{1}{2}\sin^2\theta\,(v^2 - v_t^2)}. \tag{17}$$

Note that this equation is independent of η, which implies that for small tilt angles, η has practically no influence on the vertical traveltime. This fact helps us better construct the background elliptical anisotropy, as η has little influence on this process for small tilt angles. Combine the above equations with those related to the NMO (stacking) velocity in the vertical direction:

$$\frac{1}{t_0 v_{nmo}^2} = \frac{1}{2}\frac{\partial^2 t}{\partial x^2}(x=0,z) = \frac{v_t}{z}\frac{v^2 + \frac{3}{2}\sin^2\theta\,(v^2 - v_t^2)}{v^4}, \tag{18}$$

where t_0 is given by equation 16. If we use Shanks transform again for higher-order accuracy, such an NMO velocity equation has the following form:

$$\frac{1}{t_0 v_{nmo}^2} = \frac{z}{v_t}\frac{8v_t^2v^4 - 2\,(4v^2 - 9v_t^2)\,(v^2 - v_t^2)^2\sin^4\theta + 24v_t^2\,(v^2 - v_t^2)\,v^2\sin^2\theta}{z^2\left(v^2\left(\sin^2\theta + 2\right) - v_t^2\sin^2\theta\right)^3}, \tag{19}$$

where t_0 is given by equation 18. Again, these equations are independent of η. The combination of equations 16 and 18 or equations 17 and 19 for a known tilt direction can be used to estimate the velocity along the symmetry axis as well as δ $(= \frac{v^2 - v_t^2}{2v_t^2})$.

Specifically, the above formulations provide a mechanism to evaluate the symmetry-direction (anisotropy) parameters from measurements obtained using the conventional seismic experiment, vertical and stacking velocities.

Focusing on the performance of approximation 8 for small offsets allows us to predict the accuracy of equations 16 and 18 as they are derived from equation 8. Figure 4 repeats the example of Figure 2 with a tilt of 5° (a), 10° (b), and 20° (c), and a focus on small offsets (near vertical). Of course, errors increase with the increase in the tilt angle as all approximations are for small tilt angles from vertical. Though the vertical direction error in the case of the new equations is higher, the slope of the error is almost zero indicating that the new equation should provide a good estimation of the NMO velocity (extracted from the second derivative of traveltime with respect to offset). This feature is critical since the errors associated with the other approximations (i.e. Sena (1991)) for the NMO representation are large. This also explains the higher accuracy of the new equations at higher offsets as the error gradient is small. It is also clear from Figure 4 that using Pade approximations to predict the higher-order terms of the expansion in θ did not increase the accuracy much (the difference between solid and dashed black curves). This is also observed for anelliptic TI as we will see next.

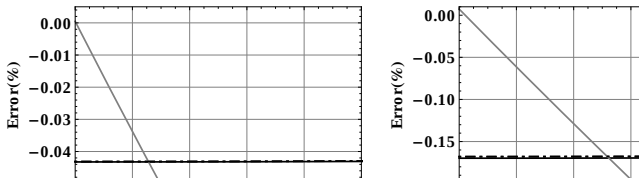

Figure 4: The relative traveltime error as a function of offset (near zero offset) for an elliptical anisotropic model with v=2 km/s, $\delta = \epsilon = 0.2$, $\theta = 20^0$, and a reflector depth z=2 km for the new expansion (equation 8) in θ (dashed black curve), the new expansion with Pade approximation in θ (solid black curve), and for the Sena approximation (solid gray curve). The plots correspond to (a) a 5 degree tilt, (b) a 10 degree tilt, and (c) a 20 degree tilt. thetaScan/Math verticaleta0

For anelliptic TI media with $\delta = 0.1$ and $\epsilon = 0.2$, I obtain similar results. Figure 5 shows the traveltime error over a limited offset for three symmetry tilt angles: (a) 5°, (b) 10°, and (c) 20°. Again, the accuracy of the new equations is apparent in the slope of the error near zero offset, implying that the NMO velocity representation is highly accurate. The errors in the vertical velocity, though, are the largest for the new equations. However, the vertical velocity genrally has less influence than the NMO velocity on time processing objectives.

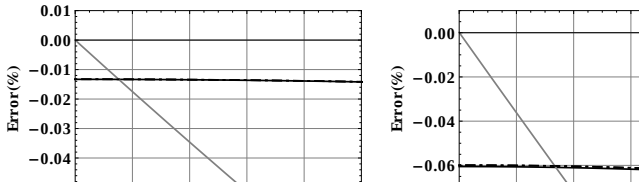

Figure 5: The relative traveltime error as a function of offset (near zero offset) for a TI model with v=2 km/s, $\delta = 0.1$, $\epsilon = 0.2$, $\theta = 20^0$, and a reflector depth z=2 km for the new expansion (equation 8) in θ (dashed black curve), the new expansion with Pade approximation in θ (solid black curve), and for the Sena approximation (solid gray curve). The plots correspond to (a) a 5 degree tilt, (b) a 10 degree tilt, and (c) a 20 degree tilt. thetaScan/Math vertical

Finally, for a TI medium with $\delta = 0.0$ and $\epsilon = 0.2$ (Figure 6) we observe similar behavior with smaller overall relative errors compared to Figures 4 and 5. As δ decreases, the anisotropy influence near the vertical direction decreases, and the effect of the tilt is less pronounced. However, when the tilt is larger, Figure 6c, the errors are large and comparable to those in Figures 4c and 5c as the influence of η starts to appear.

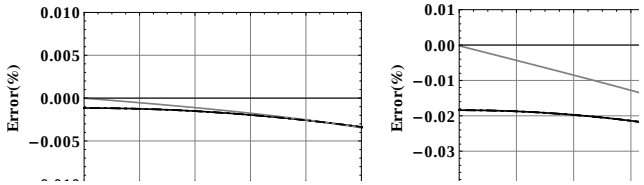

Figure 6: The traveltime error as a function of offset (near zero offset) for a TI anisotropic model with v=2 km/s, $\delta = 0.0$, $\epsilon = 0.2$, $\theta = 20^0$, and a reflector depth z=2 km for the new expansion (equation 8) in θ (dashed black curve), the new expansion with Pade approximation in θ (solid black curve), and for the Sina approximation (solid gray curve). The plots correspond to (a) a 5 degree tilt, (b) a 10 degree tilt, and (c) a 20 degree tilt. thetaScan/Math verticaleta2

In the above examples we note that despite the inferior accuracy of equations 16 and 18 in representing the vertical traveltime, with relative errors that could reach

0.3 percent for the 20 degree tilt case, it has superior qualities in predicting the NMO velocity. This phenomenon is explained by the fact that the new equations are expansions with respect to tilt angle, while the other equations are expansions with respect to offset (or anisotropy parameters), thus they provide better accuracy near zero offset. In contrast, the new equations tend to be more offset independent and better represent the moveout over larger offsets.

THE SYMMETRY-AXIS AZIMUTH AND THE 3-D CASE

In 3D, the tilt of the symmetry axis is defined by an angle, θ, measured from vertical, and the azimuth, ϕ, of the vertical plane that contains the symmetry axis. Thus, ϕ is an angle measured in the horizontal plane from a given axis within that plane. To implement an expansion with respect to ϕ, we must consider ϕ to be generally small. Since seismic acquisition is often performed in the dip direction of the structure, and we anticipate that the tilt is influenced by the presumed subsurface structure (folding), it would be reasonable to measure ϕ from the acquisition direction. In this case, I can consider ϕ to be small, and thus, approximate the traveltime solution of the eikonal equation with the following expansion:

$$\tau(x,y,z) \approx \tau_0(x,y,z) + \tau_1(x,y,z)\sin\phi + \tau_2(x,y,z)\sin^2\phi, \tag{20}$$

to be inserted in the acoustic eikonal equation for TI in 3D given by

$$a_4 v_t^4 \left(\frac{\partial \tau}{\partial z}\right)^4 + a_3 v_t^3 \left(\frac{\partial \tau}{\partial z}\right)^3 + a_2 v_t^2 \left(\frac{\partial \tau}{\partial z}\right)^2 + a_1 v_t \frac{\partial \tau}{\partial z} + a_0 = 0, \tag{21}$$

where a_0, a_1, a_2, a_3, and a_4 are stated in Appendix D. This is a complicated eikonal equation that is highly nonlinear, and thus, justifies our effort to simplify it through perturbation theory.

Substituting the trial solution, equation 20, into the eikonal equation for 3D TI media, equation 21, yields a polynomial expansion in the powers of $\sin\phi$. The zero-order term of this polynomial represents the eikonal equation for TI media for the zero-azimuth case (the 2-D result). The coefficient of the $\sin\phi$ term yields a first-order PDE for τ_1. For simplicity, it is shown here for the case of elliptical anisotropy ($\eta = 0$) as

$$\begin{aligned}
& \left(\left(v^2\cos^2\theta + v_t^2\sin^2\theta\right)\frac{\partial \tau_0}{\partial x} + \left(v^2 - v_t^2\right)\sin\theta\cos\theta\frac{\partial \tau_0}{\partial z}\right)\frac{\partial \tau_1}{\partial x} \\
+ \quad & v^2\frac{\partial \tau_0}{\partial y}\frac{\partial \tau_1}{\partial y} \\
+ \quad & \left(\left(v^2\sin^2\theta + v_t^2\cos^2\theta\right)\frac{\partial \tau_0}{\partial z} + \left(v^2 - v_t^2\right)\sin\theta\cos\theta\frac{\partial \tau_0}{\partial x}\right)\frac{\partial \tau_1}{\partial z} \\
= \quad & \left(v^2 - v_t^2\right)\sin\theta\frac{\partial \tau_0}{\partial y}\left(\cos\theta\frac{\partial \tau_0}{\partial z} - \sin\theta\frac{\partial \tau_0}{\partial x}\right).
\end{aligned} \tag{22}$$

We can obtain similar PDEs for the other coefficients of the expansion, but obtaining the 2D background TI model will be a challenging task. We can use the 2D version of the equation, developed earlier, to manage this task; however, the influence of ignoring the azimuth on that process could be critical.

A more realistic implementation is achieved by expanding from an elliptically anisotropic background with a vertical symmetry axis background in terms of η, θ, and ϕ, simultaneously. However, since a vertical symmetry axis has no particular azimuth (a singularity), I replace the tilt and azimuth by n_x and n_y ($n_x = \sin\theta\cos\phi$ and $n_y = \sin\theta\sin\phi$). For simplicity and to be able to include the resulting equations in this paper, I only consider first-order terms of the Taylor's series expansion, and thus, consider the following trial solution:

$$\tau(x,y,z) \approx \tau_0(x,y,z) + \tau_\eta(x,y,z)\eta + \tau_{n_x}(x,y,z)n_x + \tau_{n_y}(x,y,z)n_y. \tag{23}$$

In Appendix D, we look at higher-order expansions in η to take advantage of the Shanks transform properties, which considerably helps in the η case. Inserting equation 23 into equation 21 and equating terms of similar powers of the independent parameters (η, n_x, and n_y) yields an elliptically anisotropic eikonal equation with a vertical symmetry axis from the zeroth-order term and first order PDEs from the other terms that have the same form as equation 7. The source functions are shown in Appendix D.

Assuming a homogeneous-medium background yields an analytic relation, as shown in Appendix D [equation D-13]:

$$\begin{aligned}\tau(x,y,z) &\approx \sqrt{\frac{x^2}{v^2}+\frac{y^2}{v^2}+\frac{z^2}{v_t^2}} - \frac{v_t^4\eta\left(x^2+y^2\right)^2\sqrt{\frac{x^2+y^2}{v^2}+\frac{z^2}{v_t^2}}}{\left(v^2z^2+v_t^2\left(x^2+y^2\right)\right)^2} \\ &+ \frac{\left(v_t^2-v^2\right)z\sin\theta}{v^2v_t^2\sqrt{\frac{x^2+y^2}{v^2}+\frac{z^2}{v_t^2}}}\left(x\cos\phi+y\sin\phi\right).\end{aligned} \tag{24}$$

From this first-order approximation in all three parameters (η, n_x, and n_y), we can see that by setting $v_t = v$ ($\delta = 0$), the last term in the equation, that contains the tilt component, equals zero. This happens also if $\theta = 0$ (axis is vertical), and the traveltime is dependent only on η. The η-term (second on the right hand side) in this first-order approximation has no dependence on symmetry angle. Also, note that this equation has a complex variation with offset (i.e. nonhyperbolic), however, reducing to a hyperbolic equation if η and the symmetry angle are equal to zero.

DISCUSSION

The main objective of the newly developed expressions is parameter estimation in complex media. Specifically, the perturbation PDEs developed here are with respect to a background generally inhomogeneous, and possibly anisotropic, medium. If a

generally inhomogeneous isotropic velocity field is available (for example from conventional migration velocity analysis), in addition to a map of the well-to-seismic misties, which can be used to develop a vertical velocity field, then an elliptical anisotropic model with a vertical symmetry axis can be constructed. We can use this model to solve for traveltimes in elliptically anisotropic media as a background model, as well as to solve for the expansion coefficients using equations 7. These coefficients can be used with, for example, equation 23 to search explicitly for the η, and tilt angles θ and ϕ in 3D that provides the best traveltime fit to the data. This process can be implemented in a semblance-type search or incorporated as part of a tomographic inversion. Though the scans are based on an underline factorized assumption in the perturbation parameters, η and the tilt angles, we can allow them to vary smoothly with location, and thus, produce effective values. The conversion of these effective values to interval ones in generally inhomogeneous media is not trivial and might require a tomographic treatment of its own.

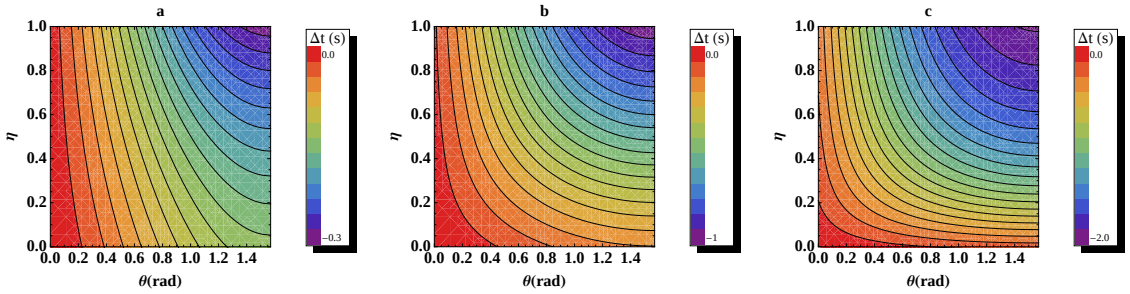

Figure 7: The traveltime difference between the TTI model computed using equation 9 and the elliptically anisotropic with a vertical symmetry axis background model for (a) an offset of 1 km, (b) an offset of 2 km, and (c) an offset of 4 km. The medium has v_t=2 km/s, v=2 km/s ($\delta = 0$), and a reflector depth, z=2 km. thetaScan/Math etaTheta

In 3D, the search for η and the symmetry direction angles can be applied either sequentially or to all the parameters at once. A sequential search, though faster and easier, may propagate some of the errors of an initial (wrong) tilt into the estimation of the parameter η (Behera and Tsvankin, 2009). The search for all three parameters simultaneously would reduce such errors, but it will suffer from a null space based on the tradeoff between η and the tilt angles. Conventionally, the information for η could be extracted, especially for small tilt angles from vertical, which is assumed here, from long offsets and dipping reflectors. The tilt information resolution in 3D requires a 3D coverage (i.e. wide azimuth or even narrow azimuth for small tilt azimuth). There is also a general tradeoff, even in 2D media, between η and the tilt angle, which may require some a priori information for η or constraining the tilt angle to be normal to the reflector dip (Alkhalifah and Bednar, 2000). Figure 7 shows the dependence of traveltime in the 2D case, based on equation 9, on the parameters η and θ. For a single offset, clearly there are combinations of η and θ (given by the contour lines) that provide equal traveltimes. Nevertheless these curves clearly vary

from one offset to another. Specifically, near offsets (Figure 7a, where $x/z = 0.5$), for mostly small tilt angles, show little dependence of traveltime on η, and more dependence on θ. On the other hand, as the tilt angle increases the resolution of η increases as its influence starts to affect even the shorter offsets. The dependence of the traveltime on η increases for $x/z = 1$ (Figure 7b) and $x/z = 2$ (Figure 7c), which implies that η is better resolved at large offsets for small tilt angles. However, it is resolved even better for large tilt angles in all cases. Meanwhile, larger offsets with reasonable η values result in less dependence of the traveltime on tilt angle.

The availability of multi-offset data will increase our chances in resolving both η and the tilt angle in 2D. The addition of multi azimuth should help resolve the tilt in 3D. Of course, the accuracy of resolving these parameters will depend mainly on how well we estimate the original elliptically anisotropic background medium. However, we can always go back and improve on our velocity picks once an approximate effective η and tilt-angle fields are estimated. There are probably many other more sophisticated ways to explore this parameter matrix, however, the equations introduced here provides the basis for doing so.

CONCLUSIONS

Expanding the traveltime solutions of the TI eikonal equation in a power series in terms of independent parameters, like the tilt angle θ in 2D, provides an efficient tool to estimate θ in a generally inhomogeneous background medium. Additional expansions from a background elliptical anisotropic medium with a vertical symmetry axis allows us to search for the anisotropy parameter η and the tilt angles simultaneously, even in 3D media. For a homogeneous background, I obtain analytic nonhyperbolic moveout equations for anisotropic media that are generally simple, and yet accurate. Nevertheless, the formulations provide η and tilt-angles estimation capabilities for a general inhomogeneous background medium.

ACKNOWLEDGMENTS

I am grateful to KAUST for its financial support. I also thank Andrej Bona, Ilya Tsvankin, Ivan Psencik, and Andres Pech for their critical and helpful reviews of the paper.

REFERENCES

Alkhalifah, T., 1995, Efficient syntheticseismogram generation in transversely isotropic, inhomogeneous media: Geophysics, **60**, 1139–1150.

———, 1998, Acoustic approximations for processing in transversely isotropic media: Geophysics, **63**, 623–631.

———, 2000a, An acoustic wave equation for anisotropic media: Geophysics, **65**, 1239–1250.

———, 2000b, The offset-midpoint traveltime pyramid in transversely isotropic media: Geophysics, **65**, 1316–1325.

———, 2010, Scanning anisotropy parameters in general inhomogeneous media: submitted to Geophysics.

Alkhalifah, T., and J. Bednar, 2000, Building a 3-D anisotropic model: Its implications to traveltime calculation and velocity analysis: 70th Ann. Internat. Mtg, Soc. of Expl. Geophys., 965–968.

Alkhalifah, T., and S. Fomel, 2001, Implementing the fast marching eikonal solver: spherical versus Cartesian coordinates: Geophys. Prosp., **49**, 165–178.

Alkhalifah, T., and K. Larner, 1994, Migration error in transversely isotropic media: Geophysics, **59**, 1405–1418.

Alkhalifah, T., and P. Sava, 2010, A transversely isotropic medium with a tilted symmetry axis normal to the reflector: Geophysics, **75**, A19–A24.

Audebert, F. S., A. Pettenati, and V. Dirks, 2006, TTI anisotropic depth migration - which tilt estimate should we use?: EAGE, Expanded Abstracts, P185.

Ball, G., 1995, Estimation of anisotropy and anisotropic 3-D prestack depth migration, offshore Zaire: Geophysics, **60**, 1495–1513.

Behera, L., and I. Tsvankin, 2009, Migration velocity analysis for tilted transversely isotropic media: Geophysical Prospecting, **57**, 13–26.

Bender, C. M., and S. A. Orszag, 1978, Advanced mathematical methods for scientists and engineers: McGraw-Hill.

Cerveny, V., 2001, Seismic ray theory: Cambridge University Press.

Grechka, V., and A. Pech, 2006, Quartic reflection moveout in a weakly anisotropic dipping layer: Geophysics, **71**, no. 1, D1–D13.

Grechka, V., and I. Tsvankin, 2000, Inversion of azimuthally dependent NmO velocity in transversely isotropic media with a tilted axis of symmetry: Geophysics, **65**, 232–246.

Ohlsen, F., and C. MacBeth, 1999, Elliptical anisotropy: Regression or advance?: SEG, Expanded Abstracts, **18**, 1600–1603.

Pech, A., I. Tsvankin, and V. Grechka, 2003, Quartic moveout coefficient: 3D description and application to tilted Ti media: Geophysics, **68**, 1600–1610.

Peng, C., and K. Steenson, 2001, 3-D prestack depth migration in anisotropic media: A case study at the Lodgepole reef play in North Dakota: The Leading Edge, **20**, 524–527.

Popovici, M., 1991, Finite difference travel time maps, *in* SEP-70: Stanford Exploration Project, 245–256.

Sena, A. G., 1991, Seismic traveltime equations for azimuthally anisotropic and isotropic media: Estimation of interval elastic properties: Geophysics, **56**, 2090–2101.

Tsvankin, I., 1997, Moveout analysis for tranversely isotropic media with a tilted symmetry axis: Geophysical Prospecting, **45**, 479–512.

van Trier, J., and W. W. Symes, 1991, Upwind finite-difference calculation of traveltimes: Geophysics, **56**, 812–821.

Vidale, J. E., 1990, Finite-difference calculation of traveltimes in three dimensions: Geophysics, **55**, 521–526.

Wang, Y., T. Nemeth, and R. T. Langan, 2006, An expanding-wavefront method for solving the eikonal equations in general anisotropic media: Geophysics, **71**, T129–T135.

APPENDIX A: EXPANSION IN θ

To derive a traveltime equation in terms of perturbations in θ, we first establish the form for the governing equation for TI media given by the eikonal representation. The eikonal equation for p-waves in TI media in 2D (for simplicity) is given by

$$v^2(1+2\eta)\left(\cos\theta\frac{\partial\tau}{\partial x}+\sin\theta\frac{\partial\tau}{\partial z}\right)^2+$$
$$v_t{}^2\left(\cos\theta\frac{\partial\tau}{\partial z}-\sin\theta\frac{\partial\tau}{\partial x}\right)^2\left(1-2\eta v^2\left(\cos\theta\frac{\partial\tau}{\partial x}+\sin\theta\frac{\partial\tau}{\partial z}\right)^2\right)=1. \quad \text{(A-1)}$$

To solve equation A-1 through perturbation theory, we assume that θ is small, and thus, a trial solution can be expressed as a series expansion in $\sin\theta$ given by

$$\tau(x,z)\approx\tau_0(x,z)+\tau_1(x,z)\sin\theta+\tau_2(x,z)\sin^2\theta, \quad \text{(A-2)}$$

where τ_0, τ_1 and τ_2 are coefficients of the expansion given in units of traveltime, and, for practicality, terminated at the second power of $\sin\theta$. Inserting the trial solution, equation A-2, into equation A-1 yields a long formula, but by setting $\sin\theta=0$, I obtain the zeroth-order term given by

$$v^2(1+2\eta)\left(\frac{\partial\tau_0}{\partial x}\right)^2+v_t{}^2\left(\frac{\partial\tau_0}{\partial z}\right)^2\left(1-2\eta v^2\left(\frac{\partial\tau_0}{\partial x}\right)^2\right)=1, \quad \text{(A-3)}$$

which is the eikonal formula for VTI anisotropy. By equating the coefficients of the powers of the independent parameter $\sin\theta$, in succession, we end up first with the coefficients of first-power in $\sin\theta$, simplified by using equation A-3, and given by

$$v^2\frac{\partial\tau_1}{\partial x}\left((2\eta+1)\frac{\partial\tau_0}{\partial x}-2v_t^2\eta\frac{\partial\tau_0}{\partial x}\left(\frac{\partial\tau_0}{\partial z}\right)^2\right)+v_t^2\frac{\partial\tau_1}{\partial z}\left(\frac{\partial\tau_0}{\partial z}-2v^2\eta\left(\frac{\partial\tau_0}{\partial x}\right)^2\frac{\partial\tau_0}{\partial z}\right)=$$
$$2v^2v_t^2\eta\left(\frac{\partial\tau_0}{\partial x}\left(\frac{\partial\tau_0}{\partial z}\right)^3-\left(\frac{\partial\tau_0}{\partial x}\right)^3\frac{\partial\tau_0}{\partial z}\right)-v^2(2\eta+1)\frac{\partial\tau_0}{\partial x}\frac{\partial\tau_0}{\partial z}+v_t^2\frac{\partial\tau_0}{\partial x}\frac{\partial\tau_0}{\partial z}. \quad \text{(A-4)}$$

which is a first-order linear partial differential equation in τ_1. The coefficient of $\sin\theta^2$, with some manipulation, has the following form

$$2v^2\frac{\partial\tau_2}{\partial x}\left((2\eta+1)\frac{\partial\tau_0}{\partial x}-2v_t^2\eta\frac{\partial\tau_0}{\partial x}\left(\frac{\partial\tau_0}{\partial z}\right)^2\right)+2v_t^2\frac{\partial\tau_2}{\partial z}\left(\frac{\partial\tau_0}{\partial z}-2v^2\eta\left(\frac{\partial\tau_0}{\partial x}\right)^2\frac{\partial\tau_0}{\partial z}\right)=$$
$$v^2(2\eta+1)\left(\frac{\partial\tau_0}{\partial x}\right)^2+2v^2v_t^2\eta\left(\frac{\partial\tau_0}{\partial z}\right)^4+2v_t^2\frac{\partial\tau_1}{\partial x}\frac{\partial\tau_0}{\partial z}-v_t^2\left(\frac{\partial\tau_1}{\partial z}-\frac{\partial\tau_0}{\partial x}\right)^2+v_t^2\left(\frac{\partial\tau_0}{\partial z}\right)^2$$
$$+4v^2v_t^2\eta\frac{\partial\tau_1}{\partial x}\left(\frac{\partial\tau_0}{\partial z}\right)^3-12v^2v_t^2\eta\left(\frac{\partial\tau_0}{\partial x}\right)^2\left(\frac{\partial\tau_0}{\partial z}\right)^2+2v^2v_t^2\eta\left(\frac{\partial\tau_1}{\partial x}\right)^2\left(\frac{\partial\tau_0}{\partial z}\right)^2$$
$$+12v^2v_t^2\eta\frac{\partial\tau_0}{\partial x}\frac{\partial\tau_1}{\partial z}\left(\frac{\partial\tau_0}{\partial z}\right)^2-12v^2v_t^2\eta\left(\frac{\partial\tau_0}{\partial x}\right)^2\frac{\partial\tau_1}{\partial x}\frac{\partial\tau_0}{\partial z}+8v^2v_t^2\eta\frac{\partial\tau_0}{\partial x}\frac{\partial\tau_1}{\partial x}\frac{\partial\tau_1}{\partial z}\frac{\partial\tau_0}{\partial z}$$
$$-v^2(2\eta+1)\left(\frac{\partial\tau_1}{\partial x}+\frac{\partial\tau_0}{\partial z}\right)^2+2v^2v_t^2\eta\left(\frac{\partial\tau_0}{\partial x}\right)^2\left(\frac{\partial\tau_1}{\partial z}-\frac{\partial\tau_0}{\partial x}\right)^2-2v^2(2\eta+1)\frac{\partial\tau_0}{\partial x}\frac{\partial\tau_1}{\partial z}, \quad \text{(A-5)}$$

which is again a first-order linear partial differential equation in τ_2 with an obviously more complicated source function given by the right-hand side. Though the equation seems complicated, many of the variables of the source function (right-hand side) can be evaluated during the evaluation of equations A-3 and A-4 in a fashion that will not add much to the cost.

APPENDIX B: EXPANSION IN θ AND η

For an expansion in θ and η, simultaneously, I use the following trial solution:

$$\tau(x,z)\approx\tau_0(x,z)+\tau_\eta(x,z)\eta+\tau_\theta(x,z)\sin\theta+\tau_{\eta_2}(x,z)\eta^2+\tau_{\eta\theta}(x,z)\eta\sin\theta+\tau_{\theta_2}(x,z)\sin^2\theta, \quad \text{(B-1)}$$

in terms of the coefficients τ_i, where the i corresponds to $\eta,\theta,\eta_2,\eta\theta$, and θ_2. Inserting the trial solution, equation B-1, into equation A-1 yields again a long formula, but by setting both $\sin\theta=0$ and $\eta=0$, I obtain the zeroth-order term given by

$$v^2(x,y,z)\left(\frac{\partial\tau_0}{\partial x}\right)^2+v_t^2(x,y,z)\left(\frac{\partial\tau_0}{\partial z}\right)^2=1\ , \quad \text{(B-2)}$$

which is simply the eikonal formula for elliptical anisotropy. By equating the coefficients of the powers of the independent parameter $\sin\theta$ and η, in succession starting with first powers of the two parameters, we end up first with the coefficients of first-power in $\sin\theta$ and zeroth power in η, simplified by using equation B-2, and given by

$$v^2\frac{\partial\tau_0}{\partial x}\frac{\partial\tau_\theta}{\partial x}+v_t^2\frac{\partial\tau_0}{\partial z}\frac{\partial\tau_\theta}{\partial z}=-\left(v^2-v_t^2\right)\frac{\partial\tau_0}{\partial x}\frac{\partial\tau_0}{\partial z}, \quad \text{(B-3)}$$

which is a first-order linear partial differential equation in τ_θ. The coefficients of zero-power in $\sin\theta$ and the first-power in η is given by

$$v^2\frac{\partial\tau_0}{\partial x}\frac{\partial\tau_\eta}{\partial x}+v_t^2\frac{\partial\tau_0}{\partial z}\frac{\partial\tau_\eta}{\partial z}=-\left(v^2\left(\frac{\partial\tau_0}{\partial x}\right)^2-v^2v_t^2\left(\frac{\partial\tau_0}{\partial x}\right)^2\left(\frac{\partial\tau_0}{\partial z}\right)^2\right), \quad \text{(B-4)}$$

The coefficients of the square terms in $\sin\theta$, with some manipulation, results in the following relation

$$2v^2\frac{\partial\tau_0}{\partial x}\frac{\partial\tau_{\theta_2}}{\partial x}+2v_t^2\frac{\partial\tau_0}{\partial z}\frac{\partial\tau_{\theta_2}}{\partial z}=v^2\left(\frac{\partial\tau_0}{\partial x}\right)^2-v^2\left(\frac{\partial\tau_\theta}{\partial x}\right)^2- 2\left(v^2-v_t^2\right)\frac{\partial\tau_\theta}{\partial x}\frac{\partial\tau_0}{\partial z}-2\left(v^2-v_t^2\right)\frac{\partial\tau_0}{\partial x}\frac{\partial\tau_\theta}{\partial z}- v_t^2\left(\frac{\partial\tau_0}{\partial x}\right)^2-v_t^2\left(\frac{\partial\tau_\theta}{\partial z}\right)^2-\left(v^2-v_t^2\right)\left(\frac{\partial\tau_0}{\partial z}\right)^2, \tag{B-5}$$

which is again a first-order linear partial differential equation in τ_{θ_2} with an obviously more complicated source function given by the right hand side. The coefficients of the square terms in η, with also some manipulation, results in the following relation

$$2v^2\frac{\partial\tau_0}{\partial x}\frac{\partial\tau_{\eta_2}}{\partial x}+2v_t^2\frac{\partial\tau_0}{\partial z}\frac{\partial\tau_{\eta_2}}{\partial z}=4v_t^2v^2\frac{\partial\tau_0}{\partial x}\frac{\partial\tau_0}{\partial z}\left(\frac{\partial\tau_\eta}{\partial x}\frac{\partial\tau_0}{\partial z}+\frac{\partial\tau_0}{\partial x}\frac{\partial\tau_\eta}{\partial z}\right)- v^2\left(\frac{\partial\tau_\eta}{\partial x}\right)^2-4v^2\frac{\partial\tau_0}{\partial x}\frac{\partial\tau_\eta}{\partial x}-v_t^2\left(\frac{\partial\tau_\eta}{\partial z}\right)^2, \tag{B-6}$$

which is again a first-order linear partial differential equation in τ_{η_2} with a again complicated source function.

Finally, the coefficients of the first-power terms in both $\sin\theta$ and η results also in a first-order linear partial differential equation in $\tau_{\eta\theta}$ given by

$$\begin{aligned}&2v^2\frac{\partial\tau_0}{\partial x}\frac{\partial\tau_{\eta\theta}}{\partial x}+2v_t^2\frac{\partial\tau_0}{\partial z}\frac{\partial\tau_{\eta\theta}}{\partial z}=\\&4v_t^2v^2\frac{\partial\tau_0}{\partial x}\frac{\partial\tau_0}{\partial z}\left(\frac{\partial\tau_0}{\partial z}\left(\frac{\partial\tau_\theta}{\partial x}+\frac{\partial\tau_0}{\partial z}\right)+\frac{\partial\tau_0}{\partial x}\left(\frac{\partial\tau_\theta}{\partial z}-\frac{\partial\tau_0}{\partial x}\right)\right)\\&-2v^2\frac{\partial\tau_0}{\partial x}\frac{\partial\tau_\eta}{\partial z}-4v^2\frac{\partial\tau_0}{\partial x}\left(\frac{\partial\tau_\theta}{\partial x}+\frac{\partial\tau_0}{\partial z}\right)-2v^2\frac{\partial\tau_\eta}{\partial x}\left(\frac{\partial\tau_\theta}{\partial x}+\frac{\partial\tau_0}{\partial z}\right)\\&+2v_t^2\frac{\partial\tau_\eta}{\partial x}\frac{\partial\tau_0}{\partial z}-2v_t^2\frac{\partial\tau_\eta}{\partial z}\left(\frac{\partial\tau_\theta}{\partial z}-\frac{\partial\tau_0}{\partial x}\right).\end{aligned} \tag{B-7}$$

Though the equation seems complicated, many of the variables of the source function (right hand side) can be evaluated during the evaluation of equations B-3 and B-4 in a fashion that will not add much to the cost.

Using Shanks transforms (Bender and Orszag, 1978) we can isolate and remove the most transient behavior of the expansion B-1 in η (the θ expansion did not improve with such a treatment) by first defining the following parameters:

$$\begin{aligned}A_0&=\tau_0+\tau_\theta\sin\theta+\tau_{\theta_2}\sin^2\theta\\A_1&=A_0+\left(\tau_\eta+\tau_{\eta\theta}\sin\theta\right)\eta\\A_2&=A_1+\tau_{\eta_2}\eta^2\end{aligned} \tag{B-8}$$

The first sequence of Shanks transforms uses A_0, A_1, and A_2, and thus, is given by

$$\tau(x,z) \approx \frac{A_0A_2 - A_1^2}{A_0 - 2A_1 + A_2} = \tau_0(x,z) + \tau_\theta(x,z)\sin\theta + \tau_{\theta_2}(x,z)\sin^2\theta + \frac{\eta\left(\tau_\eta(x,z) + \tau_{\eta\theta}(x,z)\sin\theta\right)^2}{\tau_\eta(x,z) + \tau_{\eta\theta}(x,z)\sin\theta - \eta\tau_{\eta_2}(x,z)}. \quad \text{(B-9)}$$

APPENDIX C: THE HOMOGENEOUS MEDIUM CASE

To develop analytical traveltime representation for TI media, I start with a background velocity model that is homogeneous. The expansion here will be with respect to η and θ from a background elliptical anisotropic model. In this case, the traveltime from a point source at $x = 0$ and $z = 0$ is given by the following simple relation in 2-D:

$$\tau_0(x,z) = \sqrt{\frac{x^2}{v^2} + \frac{z^2}{v_t^2}}, \quad \text{(C-1)}$$

which satisfies the eikonal equation B-2. Using equation C-1, I evaluate $\frac{\partial\tau_0}{\partial x}$ and $\frac{\partial\tau_0}{\partial z}$ and insert them into equation B-3 to solve the first-order linear equation to obtain

$$\tau_\theta(x,z) = \frac{\left(v_t^2 - v^2\right)xz\sqrt{\frac{x^2}{v^2} + \frac{z^2}{v_t^2}}}{v^2z^2 + v_t^2x^2}, \quad \text{(C-2)}$$

as well as insert them into equation B-4 and solve the equation to obtain

$$\tau_\eta(x,z) = -\frac{v_t^4x^4\sqrt{\frac{x^2}{v^2} + \frac{z^2}{v_t^2}}}{\left(v^2z^2 + v_t^2x^2\right)^2}, \quad \text{(C-3)}$$

I now evaluate $\frac{\partial\tau_\theta}{\partial x}$ and $\frac{\partial\tau_\theta}{\partial z}$ and use them to solve equation B-5. After some tedious algebra, I obtain

$$\tau_{\theta_2}(x,z) = \frac{\sqrt{\frac{x^2}{v^2} + \frac{z^2}{v_t^2}}\left(-v^4z^4 + v^2v_t^2\left(x^4 + z^4\right) - v_t^4x^4\right)}{2\left(v^2z^2 + v_t^2x^2\right)^2}. \quad \text{(C-4)}$$

I also evaluate $\frac{\partial\tau_\eta}{\partial x}$ and $\frac{\partial\tau_\eta}{\partial z}$ and use them to solve equation B-6 to obtain

$$\tau_{\eta_2}(x,z) = \frac{3v_t^6x^6\sqrt{\frac{x^2}{v^2} + \frac{z^2}{v_t^2}}\left(4v^2z^2 + v_t^2x^2\right)}{2\left(v^2z^2 + v_t^2x^2\right)^4}. \quad \text{(C-5)}$$

Finally, I solve equation B-7. After some tedious algebra once again, I obtain

$$\tau_{\eta\theta}(x,z) = -\frac{v_t^4x^3z\sqrt{\frac{x^2}{v^2} + \frac{z^2}{v_t^2}}\left(\left(3v^2 + v_t^2\right)x^2 + 4v^2z^2\right)}{\left(v^2z^2 + v_t^2x^2\right)^3}. \quad \text{(C-6)}$$

Using the first sequence of Shanks transform, equation B-9, applied to the Taylor's series expansion, we obtain an analytical equation that describes traveltime as a function of η and θ.

For 3-D media, I include the azimuth angle as we will see next.

APPENDIX D: EXPANSION IN 3D

The eikonal equation for P-waves in a TI medium with a tilt in the symmetry axis satisfies the following relation,

$$a_4 v_t^4 \left(\frac{\partial\tau}{\partial z}\right)^4 + a_3 v_t^3 \left(\frac{\partial\tau}{\partial z}\right)^3 + a_2 v_t^2 \left(\frac{\partial\tau}{\partial z}\right)^2 + a_1 v_t \frac{\partial\tau}{\partial z} + a_0 = 0, \tag{D-1}$$

where

$$\begin{aligned}
a_0 &= 2v^2 v_t^2 \eta \sin^2\theta\cos^2\theta \left(\cos\phi\frac{\partial\tau}{\partial x} - \sin\phi\frac{\partial\tau}{\partial y}\right)^4 - v^2(2\eta+1)\cos^2\theta\left(\cos\phi\frac{\partial\tau}{\partial x} - \sin\phi\frac{\partial\tau}{\partial y}\right)^2 \\
&+ 2v^2 v_t^2 \eta \sin^2\theta \left(\sin\phi\frac{\partial\tau}{\partial x} + \cos\phi\frac{\partial\tau}{\partial y}\right)^2 \left(\cos\phi\frac{\partial\tau}{\partial x} - \sin\phi\frac{\partial\tau}{\partial y}\right)^2 \\
&- v^2(2\eta+1)\left(\sin\phi\frac{\partial\tau}{\partial x} + \cos\phi\frac{\partial\tau}{\partial y}\right)^2 - v_t^2\sin^2\theta\left(\cos\phi\frac{\partial\tau}{\partial x} - \sin\phi\frac{\partial\tau}{\partial y}\right)^2 + 1, \qquad \text{(D-2)} \\
a_1 &= -\frac{2}{v_t}\sin\theta\cos\theta\left(\cos\phi\frac{\partial\tau}{\partial x} - \sin\phi\frac{\partial\tau}{\partial y}\right)\left(v_t\left(2v^2\eta\left(\sin^2\theta\cos\phi\frac{\partial\tau}{\partial x}\left(2v_t\sin\phi\frac{\partial\tau}{\partial y} - 1\right)\right.\right.\right. \\
&+ v_t\left(\frac{\partial\tau}{\partial x}\right)^2\left(\cos^2\theta\cos^2\phi + \sin^2(\phi)\right) + \frac{\partial\tau}{\partial y}\left(v_t\frac{\partial\tau}{\partial y}\left(\cos^2\theta\sin^2\phi + \cos^2(\phi)\right)\right. \\
&+ \left.\left.\left.\sin^2\theta\sin\phi\right)\right) - v_t\right) + v^2(2\eta+1)\Big), \qquad \text{(D-3)} \\
a_2 &= \frac{1}{4}\left(v^2\eta\left(-4\sin^2\theta(3\cos(2\theta)+2)\cos(2\phi)\left(\left(\frac{\partial\tau}{\partial x}\right)^2 - \left(\frac{\partial\tau}{\partial y}\right)^2\right) + 8\sin^2\theta(3\cos(2\theta)+2)\right.\right. \\
&\left.\left.\sin(2\phi)\frac{\partial\tau}{\partial x}\frac{\partial\tau}{\partial y} + (2\cos(2\theta) + 3\cos(4\theta) + 3)\left(\left(\frac{\partial\tau}{\partial x}\right)^2 + \left(\frac{\partial\tau}{\partial y}\right)^2\right)\right) - 4\cos^2\theta\right) \\
&- \frac{v^2(2\eta+1)\sin^2\theta}{v_t^2}, \qquad \text{(D-4)} \\
a_3 &= \frac{v^2\eta\sin(4\theta)\left(\cos\phi\frac{\partial\tau}{\partial x} - \sin\phi\frac{\partial\tau}{\partial y}\right)}{v_t}, \qquad \text{(D-5)} \\
a_4 &= \frac{v^2\eta\sin^2\theta\cos^2\theta}{v_t^2}. \qquad \text{(D-6)}
\end{aligned}$$

To develop equations for the coefficients of a traveltime expansion in 3D from a background elliptical anisotropy with a vertical symmetry axis I use vector notations

(n_x and n_y) to describe the tilt angles, where the components of this 2D vector describe the projection of the symmetry axis on each of the $x-z$ and $y-z$ planes, respectively. As a result,

$$n_x = \sin\theta\cos\phi, \tag{D-7}$$

and

$$n_y = \sin\theta\sin\phi. \tag{D-8}$$

Using these two equations to solve for $\sin\theta$ and $\sin\phi$ and plugging them into equation D-1 yields an eikonal for TTI media in terms of n_x and n_y. Thus, inserting the following trial solution

$$\tau(x,y,z) \approx \tau_0(x,y,z) + \tau_\eta(x,y,z)\eta + \tau_{\eta_2}(x,y,z)\eta^2 + \tau_{n_x}(x,y,z)n_x + \tau_{n_y}(x,y,z)n_y, \tag{D-9}$$

where η, n_x, and n_y are independent parameters and small, into the eikonal equation yields an extremely long equation. Again, setting the coefficients of the independent parameters (η, n_x, and n_y) to zero in the equation gives the eikonal equation for elliptical anisotropy with vertical symmetry axis. On the other hand, the coefficients of the first power of the independent parameters yield:

$$\begin{aligned}
v^2\frac{\partial\tau_0}{\partial x}\frac{\partial\tau_\eta}{\partial x} + v^2\frac{\partial\tau_0}{\partial y}\frac{\partial\tau_\eta}{\partial y} + v_t^2\frac{\partial\tau_0}{\partial z}\frac{\partial\tau_\eta}{\partial z} &= v^2\left(\left(v_t^2\left(\frac{\partial\tau_0}{\partial z}\right)^2 - 1\right)\left(\left(\frac{\partial\tau_0}{\partial x}\right)^2 + \left(\frac{\partial\tau_0}{\partial y}\right)^2\right)\right),\\
v^2\frac{\partial\tau_0}{\partial y}\frac{\partial\tau_{n_x}}{\partial y} + v^2\frac{\partial\tau_0}{\partial x}\frac{\partial\tau_{n_x}}{\partial x} + v_t^2\frac{\partial\tau_0}{\partial z}\frac{\partial\tau_{n_x}}{\partial z} &= -\left(v^2 - v_t^2\right)\frac{\partial\tau_0}{\partial x}\frac{\partial\tau_0}{\partial z},\\
v^2\frac{\partial\tau_0}{\partial y}\frac{\partial\tau_{n_y}}{\partial y} + v^2\frac{\partial\tau_0}{\partial x}\frac{\partial\tau_{n_y}}{\partial x} + v_t^2\frac{\partial\tau_0}{\partial z}\frac{\partial\tau_{n_y}}{\partial z} &= -\left(v^2 - v_t^2\right)\frac{\partial\tau_0}{\partial y}\frac{\partial\tau_0}{\partial z},
\end{aligned} \tag{D-10}$$

corresponding to η, n_x, and n_y, respectively.

The coefficient of the η^2 term, for higher accuracy in η, is given by

$$\begin{aligned}
&2v^2\frac{\partial\tau_0}{\partial x}\frac{\partial\tau_{\eta_2}}{\partial x} + 2v^2\frac{\partial\tau_0}{\partial y}\frac{\partial\tau_{\eta_2}}{\partial y} + 2v_t^2\frac{\partial\tau_0}{\partial z}\frac{\partial\tau_{\eta_2}}{\partial z} = 4v_t^2v^2\left(\frac{\partial\tau_0}{\partial z}\right)^2\left(\frac{\partial\tau_0}{\partial x}\frac{\partial\tau_\eta}{\partial x} + \frac{\partial\tau_0}{\partial y}\frac{\partial\tau_\eta}{\partial y}\right)\\
+\;& 4v_t^2v^2\frac{\partial\tau_0}{\partial z}\left(\left(\frac{\partial\tau_0}{\partial x}\right)^2 + \left(\frac{\partial\tau_0}{\partial y}\right)^2\right)\frac{\partial\tau_\eta}{\partial z} - v^2\left(\left(\frac{\partial\tau_\eta}{\partial x}\right)^2 + \left(\frac{\partial\tau_\eta}{\partial y}\right)^2\right) - 4v^2\left(\frac{\partial\tau_0}{\partial x}\frac{\partial\tau_\eta}{\partial x} + \frac{\partial\tau_0}{\partial y}\frac{\partial\tau_\eta}{\partial y}\right)\\
-\;& v_t^2\left(\frac{\partial\tau_\eta}{\partial z}\right)^2.
\end{aligned} \tag{D-11}$$

These first-order PDEs, when solved, provide traveltime approximations using equation D-9 for 3D TI media in a generally inhomogeneous elliptical anisotropic background.

For a homogeneous medium simplification, the traveltime is given by the following analytical relation in 3-D elliptical anisotropic media:

$$\tau_0(x,y,z) = \sqrt{\frac{x^2+y^2}{v^2} + \frac{z^2}{v_t^2}}, \tag{D-12}$$

which satisfies the eikonal equation B-2 in 3D. Using equation D-12, I evaluate $\frac{\partial \tau_0}{\partial x}$, $\frac{\partial \tau_0}{\partial y}$ and $\frac{\partial \tau_0}{\partial z}$ and insert them into equations D-10 to solve these first-order linear equations to obtain

$$\begin{aligned}
\tau_\eta(x,y,z) &= -\frac{v_t^4\left(x^2+y^2\right)^2\sqrt{\frac{x^2+y^2}{v^2}+\frac{z^2}{v_t^2}}}{\left(v^2z^2+v_t^2\left(x^2+y^2\right)\right)^2},\\
\tau_{n_x}(x,y,z) &= \frac{\left(v_t^2-v^2\right)xz}{v^2v_t^2\sqrt{\frac{x^2+y^2}{v^2}+\frac{z^2}{v_t^2}}},\\
\tau_{n_y}(x,y,z) &= \frac{\left(v_t^2-v^2\right)yz}{v^2v_t^2\sqrt{\frac{x^2+y^2}{v^2}+\frac{z^2}{v_t^2}}},
\end{aligned} \tag{D-13}$$

respectively.

I now evaluate $\frac{\partial \tau_\eta}{\partial x}$, $\frac{\partial \tau_\eta}{\partial y}$, and $\frac{\partial \tau_\eta}{\partial z}$ and use them to solve equation D-11. After some tedious algebra, I obtain

$$\tau_{\eta_2}(x,y,z)=\frac{3v_t^6\left(x^2+y^2\right)^3\sqrt{\frac{x^2+y^2}{v^2}+\frac{z^2}{v_t^2}}\left(4v^2z^2+v_t^2\left(x^2+y^2\right)\right)}{2\left(v^2z^2+v_t^2\left(x^2+y^2\right)\right)^4}. \tag{D-14}$$

The application of Pade approximation on the expansion in η, by finding a first order polynomial representation in the denominator, yields a TI equation that is accurate for large η (Alkhalifah, 2010), as well as small tilt, given by

$$\begin{aligned}
\tau(x,y,z) \approx\ & \frac{1}{v^2v_t^2\sqrt{\frac{x^2+y^2}{v^2}+\frac{z^2}{v_t^2}}\left(2v^4z^4+4v^2v_t^2z^2(3\eta+1)\left(x^2+y^2\right)+v_t^4(3\eta+2)\left(x^2+y^2\right)^2\right)}\\
&\Big(2v^6z^5(z-\sin\theta\left(x\cos\phi+y\sin\phi\right))-2v_t^2v^4z^3\left(\left((6\eta+2)\left(x^2+y^2\right)-z^2\right)\right.\\
&\left.(\sin\theta\left(x\cos\phi+y\sin\phi\right))-3z(2\eta+1)\left(x^2+y^2\right)\right)-v_t^4v^2z\left(x^2+y^2\right)\\
&\left(\left((3\eta+2)\left(x^2+y^2\right)-4z^2(3\eta+1)\right)\sin\theta\left(x\cos\phi+y\sin\phi\right)-z(13\eta+6)\left(x^2+y^2\right)\right)\\
&+v_t^6\left(x^2+y^2\right)^2\left(x^2(\eta+2)+z(3\eta+2)\sin\theta\left(x\cos\phi+y\sin\phi\right)+y^2(\eta+2)\right)\Big).
\end{aligned} \tag{D-15}$$

Angle gathers in wave-equation imaging for transversely isotropic media

Tariq Alkhalifah, King Abdullah University for Science and Technology,
Sergey Fomel, The University of Texas at Austin[1]

ABSTRACT

In recent years, wave-equation imaged data are often presented in common-image angle-domain gathers as a decomposition in scattering angle at the reflector, which provide a natural access to analyzing migration velocities and amplitudes. In the case of anisotropic media, the importance of angle gathers is enhanced by the need to properly estimate multiple anisotropic parameters for a proper representation of the medium. We extract angle gathers for each downward-continuation step from converting offset-frequency planes into angle-frequency planes simultaneously with applying the imaging condition in a transversely isotropic with a vertical symmetry axis (VTI) medium. The analytic equations, though cumbersome, are exact within the framework of the acoustic approximation. They are also easily programmable and show that angle gather mapping in the case of anisotropic media differs from its isotropic counterpart, with the difference depending mainly on the strength of anisotropy. Synthetic examples demonstrate the importance of including anisotropy in the angle gather generation as mapping of the energy is negatively altered otherwise. In the case of a titled axis of symmetry (TTI), the same VTI formulation is applicable but requires a rotation of the wavenumbers.

INTRODUCTION

Angle gathers have gained prominence as they provide wave equation imaging methods with an outlet to perform velocity analysis. Angle gathers also alleviate the limitations that offset gathers have in handling multi pathing (de Bruin et al., 1990; Mosher and Foster, 2000; Stolk and de Hoop, 2006). An angle gather decomposition for anisotropic media will allow us to export these features to the anisotropic world, and this is especially important considering the number of parameters we need to deal with in anisotropic media and the prevalent multi-pathing that takes place in such media.

Downward wave extrapolation provides an accurate method of seismic imaging in structurally complex areas. Downward wave extrapolation is also naturally formulated to produce angle gathers (de Bruin et al., 1990; Mosher and Foster, 2000; Rickett

[1]**e-mail:** tariq.alkhalifah@kaust.edu.sa

and Sava, 2002; Xie and Wu, 2002; Sava and Fomel, 2003; Soubaras, 2003; Biondi and Symes, 2004; Sava and Fomel, 2005). Fomel (2004) showed that structural dependence can be removed in a depth-slice approach to extracting angle gathers. Specifically, one can generate gathers at each depth level, converting offset-space-frequency planes into angle-space planes and applying simultaneously the imaging condition. The improved mapping retains velocity dependence but removes the effect of the structure. Because of its ray-parameter-based (Fourier) formulation, this approach lends itself naturally to an anisotropic phase-velocity extension.

Migration velocity analysis in anisotropic media remains a challenging and open issue. Multiple parameters are needed to represent the anisotropic model. For a transversely isotropic medium with vertical axis of symmetry (VTI media), only NMO velocity (v) and the non-elliptic parameter (η) predominantly influence imaging (Alkhalifah and Tsvankin, 1995; Alkhalifah et al., 2001). Vertical velocity (v_z) controls mainly placement of the image in depth. Nevertheless, estimating even two parameters that can vary laterally and vertically from image gathers is difficult. Angle gathers provide an opportunity to use residual moveout to help update anisotropic parameters. Biondi (2007) suggested an approach to extracting angle gathers in anisotropic media from post-migration data. Biondi's formulation is based on numerical calculation of angle gathers and relies on ray information that is hard to examine analytically.

In this paper, we develop an analytical formulation for extracting angle gathers in VTI 2D media. We use the depth-slice approach to angle gathers as a platform for the extension to VTI. Angle gather mapping depends strongly on anisotropic parameters. We analyze this dependency using numerical computations. Next, we show synthetic data examples that confirm the theoretical analysis. Finally, we explain the possible extension of our approach to TTI (tilted transversely isotropic) media. An extension to 3D can be achieved along the lines of Fomel (2004).

THE DEPTH SLICE APPROACH FOR VTI MEDIA

Relations between image coordinates and reflection (scattering) angles at reflecting interfaces can be extracted by analyzing the geometry of reflections in the simple case of a dipping reflector in a locally homogeneous medium (Fomel, 2004). The geometry of the reflection ray paths in 2-D is depicted in Figure 1(a).

According to elementary rules of geometry for the ray configuration in Figures 1(a) and 3, with the wavenumber vector given by $\mathbf{k} = \omega\,\mathbf{p}$ as it relates to the ray-parameter vector for a given angular frequency ω, opening (scattering) phase angle θ is represented by the following relation (Fomel, 2004; Sava and Fomel, 2005)

$$k_{\rm hx}^2 + k_{\rm hz}^2 = k_s^2 + k_r^2 - 2k_r k_s \cos(\theta)\ , \tag{1}$$

where $k_{\rm hx}$ and $k_{\rm hz}$ are horizontal and vertical components of the offset wave number, and k_s and k_r are source and receiver wavenumber amplitudes related to their components as follows: $k_s^2 \equiv k_{\rm sx}^2 + k_{\rm sz}^2$, $k_r^2 \equiv k_{\rm rx}^2 + k_{\rm rz}^2$, with $k_{\rm hx} \equiv k_{\rm rx} - k_{\rm sx}$, $k_{\rm mx} \equiv k_{\rm rx} + k_{\rm sx}$,

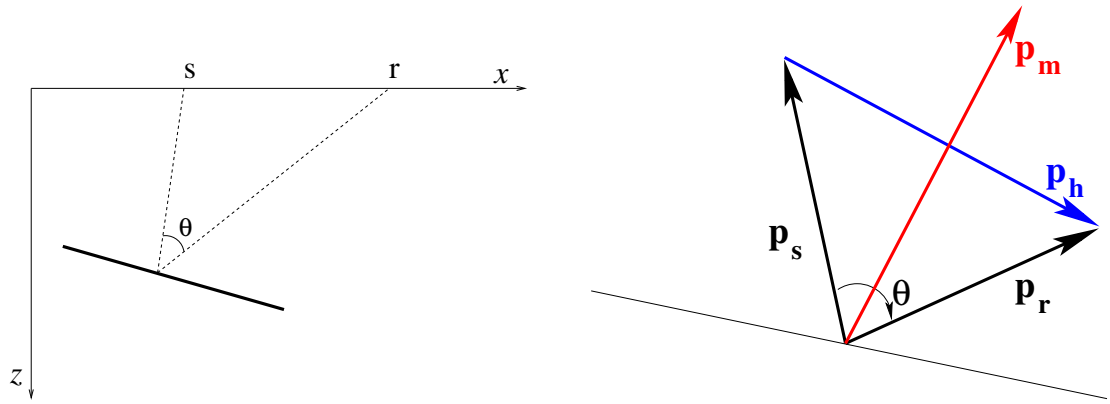

Figure 1: (a) A schematic plot showing angle θ. Although the model depicts a homogeneous setting, the development will rely on the ray parameters defined in the immediate vicinity of the the reflection point, as shown in b. (b) A schematic plot depicting the relation between the source and receiver ray-parameter vectors ($\mathbf{p}_s$ and $\mathbf{p}_g$) and the offset and midpoint vectors ($\mathbf{p}_h$ and $\mathbf{p}_m$) anisogath/XFig raysr,rayparameters

as suggested by Figure 3, where $k_{\rm mx}$ is the horizontal component of the midpoint wavenumber.

To complete the system of equations necessary to relate angle θ to midpoint and offset horizontal wavenumbers, we use the dispersion relation developed by Alkhalifah (1998) to define each of $k_{\rm sz}$ and $k_{\rm rz}$ as follows:

$$k_{\rm sz}^2 \equiv (\omega \frac{\partial t_{\rm s}}{\partial z})^2 = \frac{\omega^2}{v_z^2} - \frac{v^2\omega^2(k_{\rm hx}-k_{\rm mx})^2}{2v_z^2(2\omega^2-v^2\eta(k_{\rm hx}-k_{\rm mx})^2)}\ , \tag{2}$$

$$k_{\rm rz}^2 \equiv (\omega \frac{\partial t_{\rm r}}{\partial z})^2 = \frac{\omega^2}{v_z^2} - \frac{v^2\omega^2(k_{\rm hx}+k_{\rm mx})^2}{2v_z^2(2\omega^2-v^2\eta(k_{\rm hx}+k_{\rm mx})^2)}\ , \tag{3}$$

where v is the NMO velocity. Using equation (1) in its expanded form and after some manipulation and collecting terms with the same power of $\cos\theta$, we end up with the following quadratic equation:

$$a\cos^4(\theta) + b\cos^2(\theta) + c = 0, \tag{4}$$

with solutions given by

$$\theta = \cos^{-1}\left(\pm\sqrt{\frac{-b \pm \sqrt{b^2-4ac}}{2a}}\right)\ . \tag{5}$$

Analytical representation of the coefficients is shown in Table 1. The four solutions of equation (5) are controlled by the sign of the offset wavenumber and its magnitude compared with the midpoint wavenumber. In the frequency-wavenumber domain, equation (5) can be used to map offset (horizontal) wavenumbers to angle gathers for a specific frequency, midpoint (horizontal) wavenumber, and depth slice. A description

of an algorithm to use with the mapping equation, in the case of an isotropic medium, is given by Fomel (2004).

Setting $\eta = 0$ yields mapping for elliptical anisotropy with coefficients of equation (5) given by Table 2. The coefficients are represented by much simpler formulas. In the isotropic case, $\eta = 0$ and $v_z = v$, Table 1 reduces to Table 3 and, if substituted into the mapping formula of equation (5), is equivalent to the corresponding mapping equation of Fomel (2004).

NUMERICAL TESTS: THE ANISOTROPY INFLUENCE

Using equation (5) we evaluated angle gathers as a function of offset and midpoint wavenumbers for a given frequency. We tested such mapping for various models using different strengths of anisotropy as we varied η, v_z, and the NMO velocity v.

Figures 2-3 show contour density plots of angle as a function of offset and midpoint wavenumbers, for a 60-Hz frequency slice. In Figure 2 the medium is isotropic, with a velocity of 2 km/s. Clearly, for $k_{\rm hx} = 0$, the angle is zero regardless of the midpoint wavenumber, which is expected, because for zero-offset the scattering or opening angle is equal to zero. Also, we observe that angles decrease with dip (or k_{mx}) for a given offset wavenumber, which is also expected, because for any offset a scattering angle becomes zero in the case of a vertical reflector. The areas given in white in the Figures 2-5 correspond to regions where the k_{sz} or k_{rz} become complex, and thus represent evanescent waves.

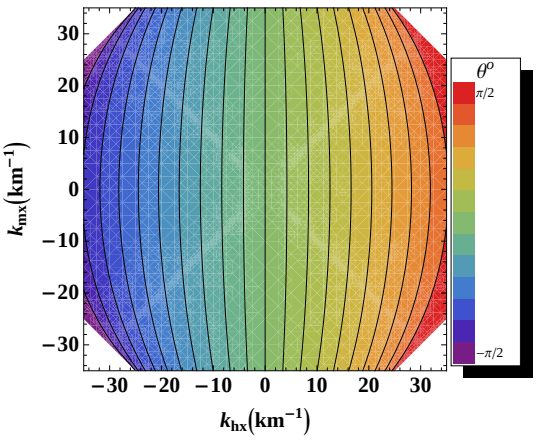

Figure 2: Constant-depth constant-frequency (60 Hz) slice mapped to opening angles for an isotropic medium with velocity equal to 2 km/s. Zero-offset wavenumber maps to zero (normal incidence) angle. The four blank corners represent evanescent regions. Negative angles correspond to a switch in the source-receiver direction, and thus, the result is symmetric based on the principal of reciprocity anisogath/Math AnglesEta0

In anisotropic media, as illustrated in Figure 3, for η equal to 0.1 and 0.3, the angles decrease with dip for a constant offset wavenumber faster than in the isotropic case. In the example, considering that v_z is lower in the anisotropic models, the

higher horizontal velocities given by the larger η resulted in smaller scattering angles because reflection occurs more updip for larger η.

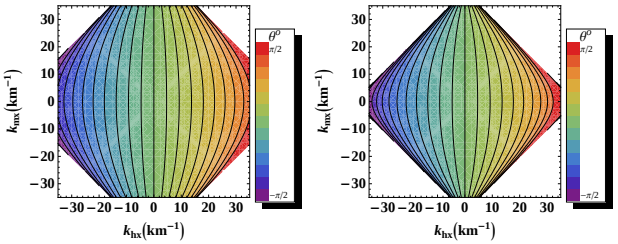

Figure 3: Constant-depth constant-frequency (60 Hz) slice mapped to opening angles as in Figure 2, but for a VTI model with v_z=1.8 km/s, v=2 km/s, and $\eta = 0.1$ (left) and $\eta = 0.3$ (right). anisogath/Math AnglesEta

Whereas the influence of η is clearly large, the change in vertical velocity has a minor influence on the angles as a function of the midpoint wavenumber (or dip), as demonstrated by the difference plot in Figure 4. A 0.6 km/s difference in vertical velocity of an elliptical isotropic model with η=0 (left) and a VTI model with η=0.3 resulted in differences mainly in the offset wavenumber direction, because depth change caused by the different vertical velocity provides variations in angles with offset.

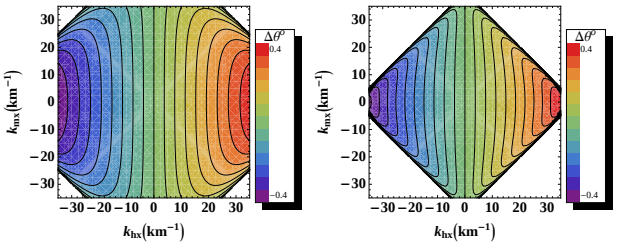

Figure 4: Left: The difference between opening angles for an elliptical anisotropic model with v_z=1.8 km/s, v=2 km/s and that of a similar model, with v_z=1.2 km/s. Right: The difference between opening angles for a VTI model of Figure 3 (right) for v_z=1.8 km/s, v=2 km/s, and $\eta = 0.3$ and that of a similar model, with v_z=1.2 km/s. anisogath/Math Anglesdiffvz

In comparison, if we change the NMO velocity, v, the angles hardly change at all, especially around small dips and small offsets. This fact is evident in Figure 5, where we change NMO velocity 0.6 km/s, and the general difference is small until we get to large offset and midpoint wavenumbers. This difference implies that the mapping is practically NMO-velocity independent. This is the case for $\eta = 0$ (left) and $\eta = 0.3$ (right) in Figure 5, which implies, that for a given elliptical anisotropic model one can find an isotropic model that produces similar mapping granted that the velocity of the isotropic model is equal to the vertical velocity for the elliptical anisotropy.

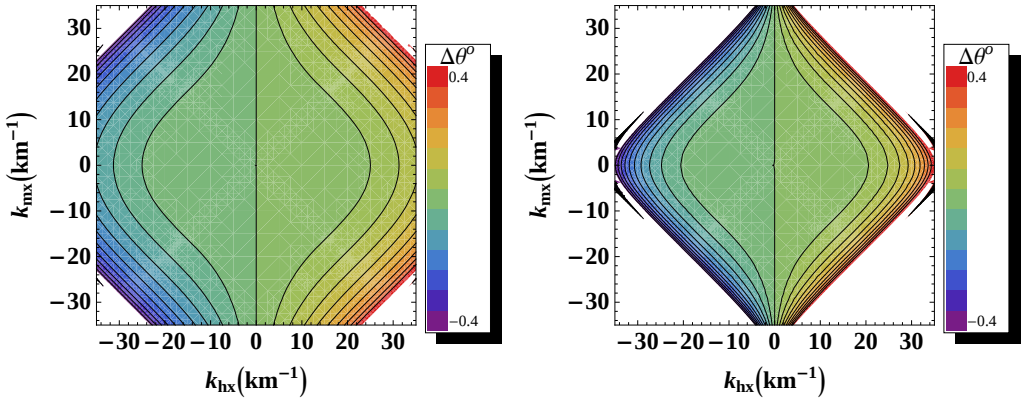

Figure 5: Left: The difference between reflection angles for an elliptical anisotropic model with v_z=1.8 km/s, v=2 km/s and that of a similar model, with v=1.4 km/s. Right: The difference between reflection angles for a VTI model of Figure 3 (right) for v_z=1.8 km/s, v=2 km/s, and $\eta = 0.3$ and that of a similar model, with v=1.4 km/s. anisogath/Math Anglesdiffv

SYNTHETIC EXAMPLE

In the following example, we use a homogeneous model for simplicity, although nothing in the development requires that. It is convenient so we can isolate the anisotropy influence on angle gathers decomposition. To follow convention, we display angle gathers in the following examples using half the opening (or scattering) angle ($= \frac{\theta}{2}$). We consider the reflector model in Figure 6, which is made up of a number of dome-like anticlines. This model allows us to focus on an angle gather located at 8 km that includes many dips. For a velocity of 2 km/s and $\eta = 0.2$, we generate the prestack synthetic dataset shown in Figure 7. We use Kirchhoff modeling to obtain the synthetic data (Alkhalifah, 1995). As a reference, we show in Figure 8 the isotropic migration of the isotropic version of the data. In this figure, we observe the extension of reflections that are acquired with a limited offset in the angle representation.

Conventional phase shift downward continuation requires that no lateral velocity variation is present. Since the synthetic model has no lateral (or even vertical) velocity variation, we use a VTI version of the DSR (double-square-root) phase-shift migration (Alkhalifah, 2000) to migrate the data. However, prior to applying the zero-time imaging condition we map the offset wavenumbers to angle, and thus, obtain angle gathers. Figure 9 shows the isotropically migrated section at near zero angle. It also shows on the right hand side the angle gather for an isotropic angle gather mapping. Clearly, the angle gather includes residuals resulting from ignoring anisotropy. These residuals start at the top with deviations at large angles with a fourth-order move-

out (known as nonhyperbolic) often associated with the semi-horizontal reflectors to second-order strong deviations typically associated with dipping reflectors (Alkhalifah and Tsvankin, 1995). The top plot in Figure 9 is a slice of a constant depth of 2 km and includes some residual information spanning other angle gathers.

If we downward continue using an anisotropic phase-shift migration followed by an isotropic angle gather mapping, we image the data accurately as shown in Figure 10. Even the angle gathers, despite using an isotropic mapping, show no residuals as we have imaged that data accurately. However, though not immediately obvious, most of the migrated energy is mapped to the wrong angle. On the other hand, an anisotropic mapping of angle gathers places reflections at their true angles (Figure 11). This fact can be realized from comparing the extension of angle gathers of Figures 10 and 11. The lower-than-actual horizontal velocity treatment in the isotropic mapping places energy at smaller reflection angle values. This phenomenon can be directly attributed to the difference between phase and group velocities. Specifically, for horizontal reflections, the isotropic angle gathers map phase angles (ignoring the difference), while anisotropic ones map ray angles. When the horizontal velocity is higher in a VTI medium, the ray angle, measured from vertical, tend to be higher than the phase angle.

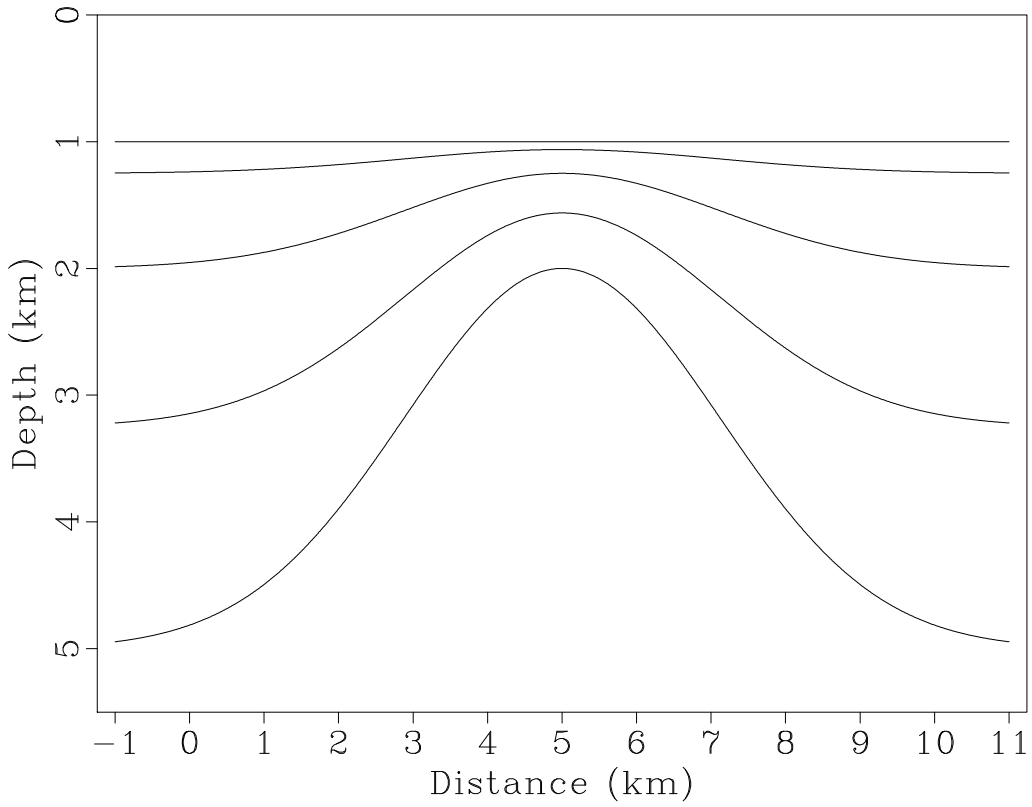

Figure 6: A reflector model containing 5 reflections in a dome like formation. We focus on angle gathers at location 8 km, at which several reflection dips are represented. anisogath/synth ref

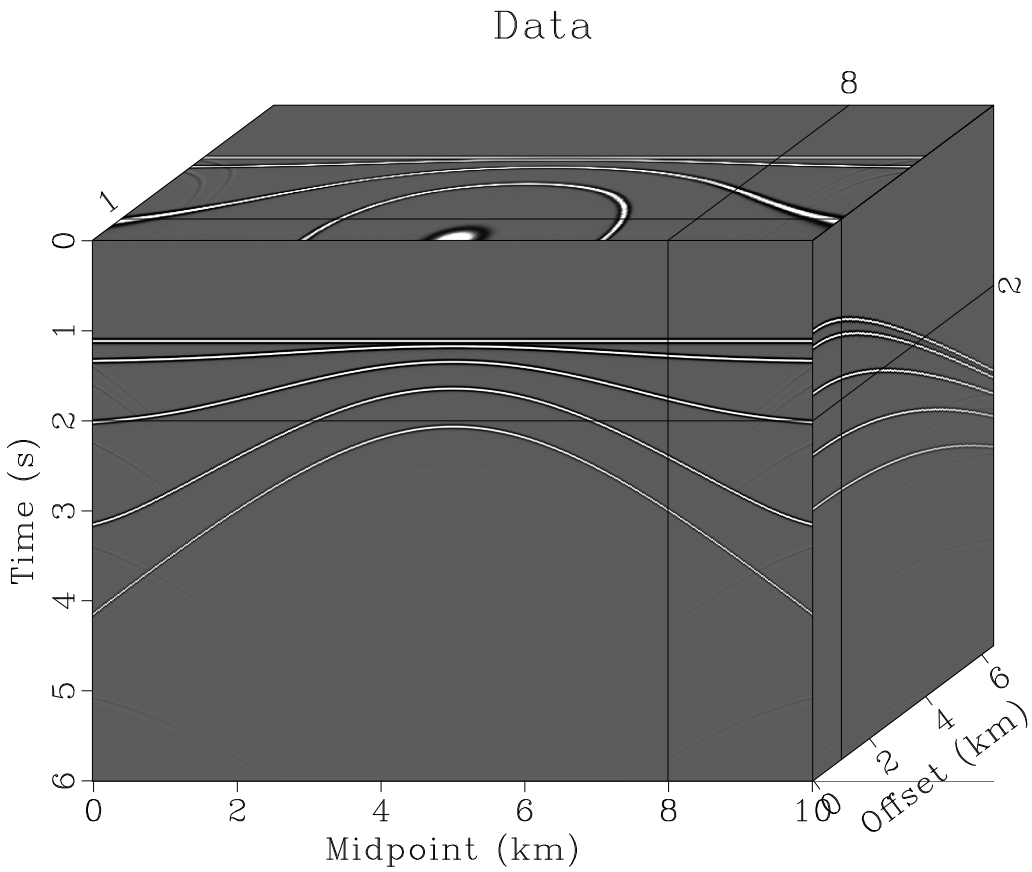

Figure 7: Prestack synthetic data generated using Kirchhoff modeling for a VTI model with velocity (NMO and vertical) equal 2 km/s and $\eta = 0.2$. anisogath/synth adata

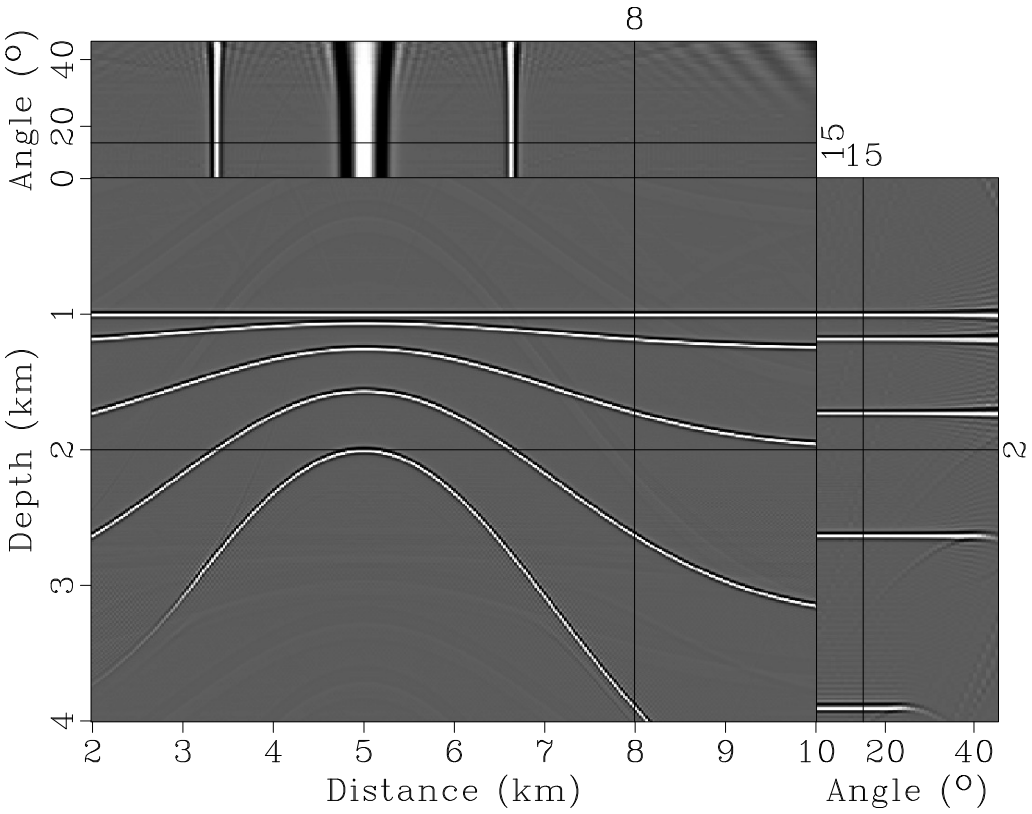

Figure 8: Migrated section after an isotropic migration with velocity of 2 km/s of an equivalent isotropic synthetic data. The angle gathers obtained using an isotropic mapping at 8 km location is displayed on the right. The top section shows a depth slice as a function of angle gather at depth 2 km. anisogath/synth agath

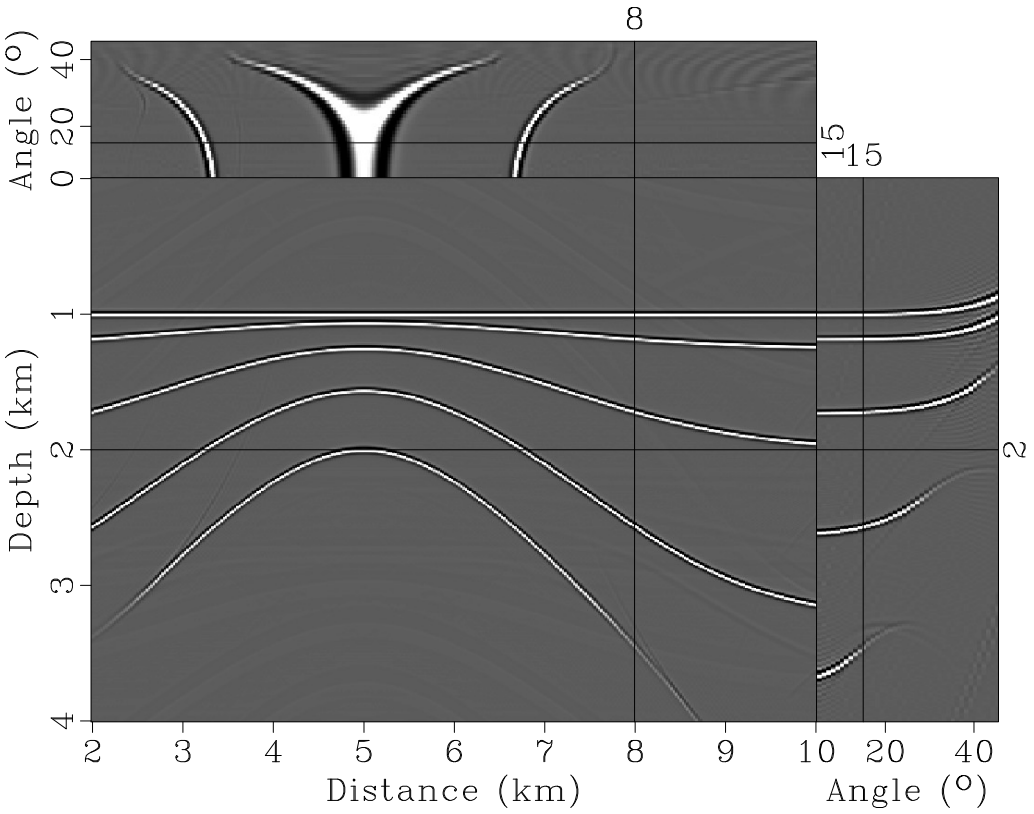

Figure 9: Migrated section after an isotropic migration with velocity of 2 km/s of the VTI synthetic data in Figure 7. Again, the angle gathers obtained using an isotropic mapping at 8 km location is displayed on the right, and the top section shows a depth slice as a function of angle gather at depth 2 km. anisogath/synth agath2

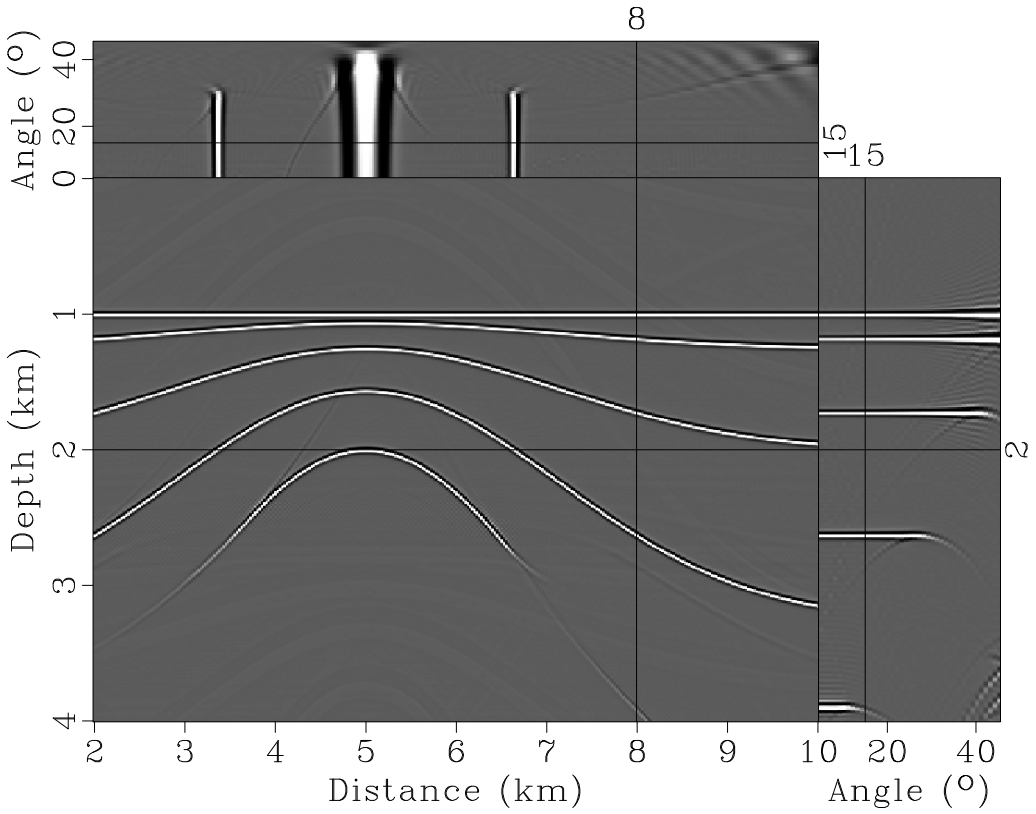

Figure 10: Migrated section after a VTI migration with velocity of 2 km/s and η=0.2 of the VTI synthetic data in Figure 7. Again, the angle gathers obtained using an isotropic mapping at 8 km location is displayed on the right, and the top section shows a depth slice as a function of angle gather at depth 2 km. anisogath/synth agath3

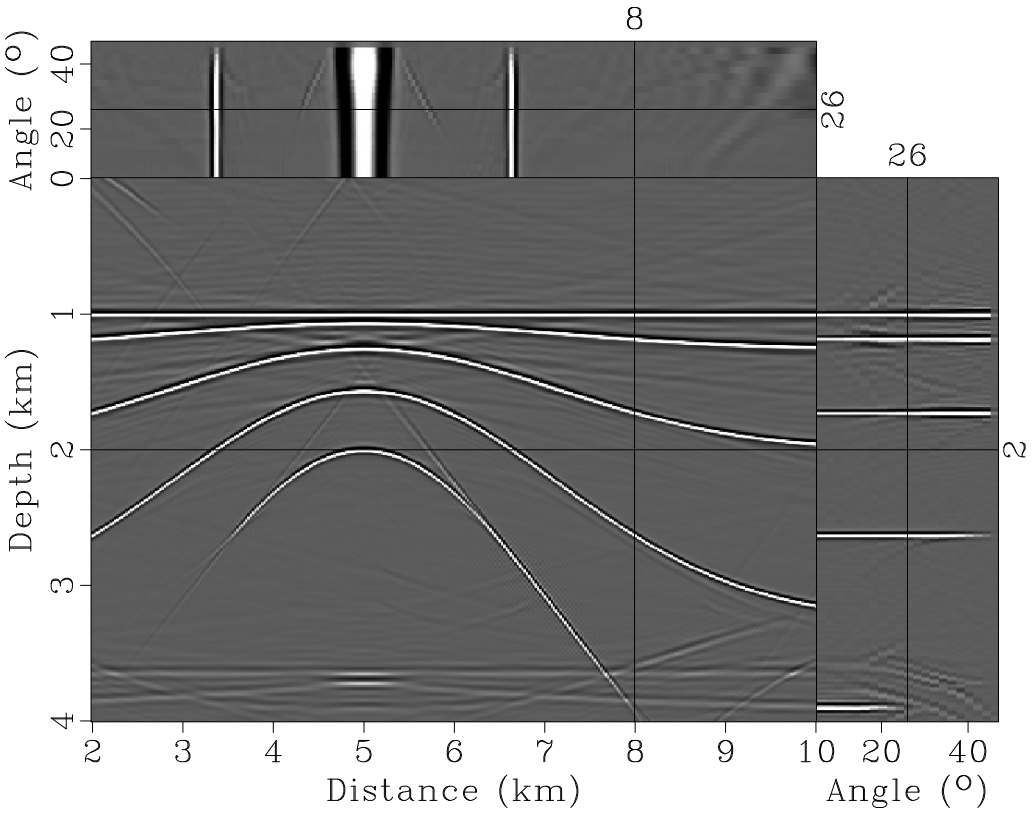

Figure 11: Migrated section after a VTI migration with velocity of 2 km/s and η=0.2 of the VTI synthetic data in Figure 7. The angle gathers obtained, now, using the VTI mapping at 8 km location is displayed on the right. The top section shows a depth slice as a function of angle gather at depth 2 km. anisogath/synth agath4

This synthetic test the importance of anisotropic angle gather mapping to place reflections at their true scattering angles. In practice, the velocity model building process uses residuals along angle gathers to estimate the required velocity update. Proper definition of the angle gather residuals will simplify the update process. This is especially true if the update is based on reflection tomography.

THE TTI CASE

In the case of a tilt in the angle of symmetry of the TI (TTI) medium, the dispersion relations 2 and 3 must be altered to reflect the tilt. Specifically, the wavenumbers should be transformed to the direction of the tilt. In fact, at the reflection point all equations used to develop the mapping in equation (4) hold regardless of the direction of tilt. This implies that the quadratic solution (5) applies with a, b, and c given by Table 1 granted that the wavenumbers are transformed in the direction of the tilt. Considering that ϕ is the tilt angle measured from vertical in 2-D, the horizontal (conventional) wavenumbers given by the surface-recorded data are given by

$$k_{sc} \equiv k_{sx} \cos\phi - k_{sz} \sin\phi, \tag{6}$$

and

$$k_{rc} \equiv k_{rx} \cos\phi - k_{rz} \sin\phi. \tag{7}$$

where k_{sx} and k_{rx} now correspond to the normal-to-the-tilt wavenumber direction and they are related to k_{sz} and k_{rz} (tilt direction wavenumbers), respectively using equations 2 and 3. Based on the above equations, to solve for k_{sx} and k_{rx} needed for the angle gather mapping, we are required to solve a quartic equation that can be represented, with pain, analytically or solved numerically. Alternatively, the formulations for a transversely isotropic medium with tilt constrained to the dip (DTI), introduced by Alkhalifah and Sava (2010), is simpler than those introduced here for a general TI medium, and thus can be used at the velocity model building stage. However, when the assumption of the tilt being normal to the reflector dip fails, for example at salt flank reflections where the tilt is generally not normal to the Salt flank, we will need a general formulation similar to the one developed here.

CONCLUSIONS

We have developed analytical relationships to generate angle gathers using wave-equation migration in VTI media. These relations are based on an approach for generating gathers at each depth level by converting offset-space-frequency planes into angle-space planes while simultaneously applying the imaging condition. Although the angle gathers depend on medium parameters, they are independent of the structure, which provides an opportunity for a simple and practical implementation. Comparing the mapping equation for VTI media with those for the isotropic case demonstrates the large influence that the anisotropy parameter η has on the mapping

process. On the other hand, the influence of vertical velocity is confined to the offset direction, and the influence of NMO velocity is small. Synthetic data applications demonstrate the importance of accurate mapping of energy in the angle domain. In the case of a TTI medium, the required modification to the mapping equations is given by the transformation of the wavenumbers in the dispersion relation to the direction of of the symmetry axis and, as a result, a similar analytic mapping exists.

ACKNOWLEDGMENTS

We are grateful to KACST, KAUST, and the Bureau of Economic Geology, University of Texas at Austin for their support. We thank Gilles Lambare, Jeff Shragge and Jun Cao for their critical and helpful review of the paper.

a	$\frac{1}{2}\left(k_h^2-k_m^2\right)^4\left(v^2\eta\left(k_h-k_m\right)^2-2\omega^2\right)^3\left(v^2(4\eta+1)\left(k_h-k_m\right)^2-4\omega^2\right)^2\left(v^2\eta\left(k_h+k_m\right)^2-2\omega^2\right)^4$ $\left[v_z^4\left(k_h^2-k_m^2\right)^2\left(-2v^2\eta k_h^2\left(v^2\eta k_m^2+2\omega^2\right)+v^4\eta^2k_h^4+\left(v^2\eta k_m^2-2\omega^2\right)^2\right)\right.$ $\left.+4\omega^4\left(2v^2(4\eta+1)k_h^2\left(v^2(4\eta+1)k_m^2+4\omega^2\right)-v^4(4\eta+1)^2k_h^4-\left(v^2(4\eta+1)k_m^2-4\omega^2\right)^2\right)\right]^2$
b	$\left(k_h^2-k_m^2\right)^4\left(-\left(v^2\eta\left(k_h-k_m\right)^2-2\omega^2\right)^3\right)\left(v^2(4\eta+1)\left(k_h-k_m\right)^2-4\omega^2\right)^2\left(v^2\eta\left(k_h+k_m\right)^2-2\omega^2\right)^4$ $\left[v_z^4\left(k_h^2-k_m^2\right)^2\left(-2v^2\eta k_h^2\left(v^2\eta k_m^2+2\omega^2\right)+v^4\eta^2k_h^4+\left(v^2\eta k_m^2-2\omega^2\right)^2\right)\right.$ $\left.+4\omega^4\left(-2v^2(4\eta+1)k_h^2\left(v^2(4\eta+1)k_m^2+4\omega^2\right)+v^4(4\eta+1)^2k_h^4+\left(v^2(4\eta+1)k_m^2-4\omega^2\right)^2\right)\right]$ $\left(\left(k_h-k_m\right)^2\left(v_z^2\left(v^2\eta\left(k_h-k_m\right)^2-2\omega^2\right)+2v^2(4\eta+1)\omega^2\right)-8\omega^4\right)$ $\left(\left(k_h+k_m\right)^2\left(v_z^2\left(v^2\eta\left(k_h+k_m\right)^2-2\omega^2\right)+2v^2(4\eta+1)\omega^2\right)-8\omega^4\right)$
c	$\frac{1}{2}\left(k_h^2-k_m^2\right)^4\left(v^2\eta\left(k_h-k_m\right)^2-2\omega^2\right)^3\left(v^2(4\eta+1)\left(k_h-k_m\right)^2-4\omega^2\right)^2\left(v^2\eta\left(k_h+k_m\right)^2-2\omega^2\right)^4$ $\left[v_z^4\left(k_h^2-k_m^2\right)^2\left(-2v^2\eta k_h^2\left(v^2\eta k_m^2+2\omega^2\right)+v^4\eta^2k_h^4+\left(v^2\eta k_m^2-2\omega^2\right)^2\right)\right.$ $\left.+4\omega^4\left(2v^2(4\eta+1)k_h^2\left(v^2(4\eta+1)k_m^2+4\omega^2\right)-v^4(4\eta+1)^2k_h^4-\left(v^2(4\eta+1)k_m^2-4\omega^2\right)^2\right)\right]^2$

Table 1: Exact analytical equations for the coefficients of equation (4).

a	$-\left(k_h^2-k_m^2\right)^4\left(vk_h-vk_m+2\omega\right)^2\left(-vk_h+vk_m+2\omega\right)^2$ $\left(-2k_h^2\left(k_m^2\left(v^4-v_z^4\right)+4v^2\omega^2\right)+k_h^4\left(v^4-v_z^4\right)+\left(v^2k_m^2-4\omega^2\right)^2-k_m^4v_z^4\right)^2$
b	$2\left(k_h^2-k_m^2\right)^4\left(vk_h-vk_m+2\omega\right)^2\left(-vk_h+vk_m+2\omega\right)^2\left(4\omega^2-\left(v^2-v_z^2\right)\left(k_h-k_m\right)^2\right)$ $\left(4\omega^2-\left(v^2-v_z^2\right)\left(k_h+k_m\right)^2\right)$ $\left(-2k_h^2\left(k_m^2\left(v^4+v_z^4\right)+4v^2\omega^2\right)+k_h^4\left(v^4+v_z^4\right)+\left(v^2k_m^2-4\omega^2\right)^2+k_m^4v_z^4\right)$
c	$-\left(k_h^2-k_m^2\right)^4\left(vk_h-vk_m+2\omega\right)^2\left(-vk_h+vk_m+2\omega\right)^2$ $\left(-2k_h^2\left(k_m^2\left(v^4-v_z^4\right)+4v^2\omega^2\right)+k_h^4\left(v^4-v_z^4\right)+\left(v^2k_m^2-4\omega^2\right)^2-k_m^4v_z^4\right)^2$

Table 2: Exact analytical equations for the coefficients of equation (4) in the case of elliptic anisotropy ($\eta = 0$).

a	$-\left(k_h^2-k_m^2\right)^4\left(vk_h-vk_m+2\omega\right)^2\left(-vk_h+vk_m+2\omega\right)^2\left(v^2\left(k_h^2+k_m^2\right)-2\omega^2\right)^2$
b	$\left(k_h^2-k_m^2\right)^4\left(vk_h-vk_m+2\omega\right)^2\left(-vk_h+vk_m+2\omega\right)^2$ $\left(v^2\left(-2k_h^2\left(v^2k_m^2+2\omega^2\right)+v^2k_h^4+v^2k_m^4-4\omega^2k_m^2\right)+8\omega^4\right)$
c	$-\left(k_h^2-k_m^2\right)^4\left(vk_h-vk_m+2\omega\right)^2\left(-vk_h+vk_m+2\omega\right)^2\left(v^2\left(k_h^2+k_m^2\right)-2\omega^2\right)^2$

Table 3: Exact analytical equations for the coefficients of equation (4) in the case of isotropy ($\eta = 0$, $v_z = v$).

REFERENCES

Alkhalifah, T., 1995, Efficient synthetic-seismogram generation in transversely isotropic, inhomogeneous media: Geophysics, **60**, 1139–1150.

———, 1998, Acoustic approximations for processing in transversely isotropic media: Geophysics, **63**, 623–631.

———, 2000, Prestack phase-shift migration of separate offsets: Geophysics, **65**, 1179–1194.

Alkhalifah, T., S. Fomel, and B. Biondi, 2001, The space-time domain:theory and modelling for anisotropic media: Geophysical Journal International, **144**, 105–113.

Alkhalifah, T., and P. Sava, 2010, A transversely isotropic medium with a tilted symmetry axis normal to the reflector: Geophysics, **75**, A18–A24.

Alkhalifah, T., and I. Tsvankin, 1995, Velocity analysis for transversely isotropic media: Geophysics, **60**, 1550–1566.

Biondi, B., 2007, Angle-domain common-image gathers from anisotropic migration: Geophysics, **72**, 581–591.

Biondi, B., and W. Symes, 2004, Angle-domain common-image gathers for migration velocity analysis by wavefield-continuation methods: Geophysics, **69**, 1283–1298.

de Bruin, C. G. M., C. P. A. Wapenaar, and A. J. Berkhout, 1990, Angle-dependent reflectivity by means of prestack migration: Geophysics, **55**, 1223–1234.

Fomel, S., 2004, Theory of 3D angle gathers in wave-equation imaging: 74th Ann. Internat. Mtg., Soc. of Expl. Geophys., 1053–1056.

Mosher, C., and D. Foster, 2000, Common angle imaging conditions for prestack depth migration: 70th Ann. Internat. Mtg, Soc. of Expl. Geophys., 830–833.

Rickett, J. E., and P. C. Sava, 2002, Offset and angle-domain common image-point gathers for shot-profile migration: Geophysics, **67**, 883–889.

Sava, P. C., and S. Fomel, 2003, Angle-domain common-image gathers by wavefield continuation methods: Geophysics, **68**, 1065–1074.

———, 2005, Coordinate-independent angle-gathers for wave equation migration, *in* 75th Ann. Internat. Mtg, Soc. Expl. Geophys., Expanded Abstracts: Soc. of Expl. Geophys., 2052–2055.

Soubaras, R., 2003, Angle gathers for shot-record migration by local harmonic decomposition: 73rd Ann. Internat. Mtg., Soc. of Expl. Geophys., 889–892.

Stolk, C., and M. V. de Hoop, 2006, Seismic inverse scattering in the downward continuation approach: Wave Motion, **43**, 579–598.

Xie, X. B., and R. S. Wu, 2002, Extracting angle domain information from migrated wavefield, *in* 72nd Ann. Internat. Mtg, Soc. Expl. Geophys., Expanded Abstracts: Soc. of Expl. Geophys., 1360–1363.

A transversely isotropic medium with a tilted symmetry axis normal to the reflector

Tariq Alkhalifah, King Abdulah University of Science and Technology, and Paul Sava, Center for Wave Phenomena, Colorado School of Mines[1]

ABSTRACT

The computational tools for imaging in transversely isotropic media with tilted axes of symmetry (TTI) are complex and in most cases do not have an explicit closed-form representation. As discussed in this paper, developing such tools for a TTI medium with tilt constrained to be normal to the reflector dip (DTI) reduces their complexity and allows for closed-form representations. We show that, for the homogeneous case zero-offset migration in such a medium can be performed using an isotropic operator scaled by the velocity of the medium in the tilt direction. We also show that, for the nonzero-offset case, the reflection angle is always equal to the incidence angle, and thus, the velocities for the source and receiver waves at the reflection point are equal and explicitly dependent on the reflection angle. This fact allows us to develop explicit representations for angle decomposition as well as moveout formulas for analysis of extended images obtained by wave-equation migration. Although setting the tilt normal to the reflector dip may not be valid everywhere (i.e., salt flanks), it can be used in the process of velocity model building where such constrains are useful and typically used.

INTRODUCTION

In recent years and with the increasing emphasis on high resolution and the availability of better computing devices, anisotropic-media treatment of seismic data is becoming part of normal operations rather than the exception. This preference is fueled by the recent observed improvements in, for example, Gulf of Mexico images when anisotropy is included in the process (Zhou et al., 2004; Huang et al., 2008). A special anisotropy, a transversely isotropic medium with a tilt in the axis of symmetry, is especially convenient in approximating the features of the medium in such regions, and provides good imaging results.

Anisotropy characterization comes in many flavors approximating all sorts of phenomena present in the subsurface by introducing directional preferences in the velocity field that accommodates such phenomena. Whether we are dealing with the natural processes of sedimentation and gravity, especially in shales, or the ever localized

[1]**e-mail:** tkhalfah@kacst.edu.sa, psava@mines.edu

vertical fractures (some also non-vertical), we can find an anisotropy that will approximate the processes influence and produce wavefields that can accurately represent wave propagation in such media. The inclusion of anisotropy into the imaging and velocity model-building process evolved through the years. As expected, we started by looking into using the simplest of the anisotropies, that is elliptical anisotropy, to handle depth shortcomings of the isotropic assumption (Ball, 1995; Ohlsen and MacBeth, 1999), despite its impracticality. However, the size of the consistent non-hyperbolicity forced some to use a slightly more complex model and yet more practical (Alkhalifah and Larner, 1994), that is the transversely isotropic (TI) media with a vertical symmetry axis (VTI). Though this model proved resilient in many areas of the subsurface (Alkhalifah, 1997; Martinez and Lee, 2002), the dips of layers near salt flanks seemingly required additional degrees of freedom provided by the tilt of the symmetry axis in the transversely isotropic medium (Isaac and Lawton, 2004).

The vertical and normal moveout (NMO) velocities, as well as the nonhyperbolic dimensionless parameter, η, define the anisotropy aspects of the TI model for P-waves, at least to the accuracy required for prestack imaging (Alkhalifah and Tsvankin, 1995). If the symmetry axis is vertical no other parameters are needed to define the TI model. However, since the stratification in the Earth subsurface is not always horizontal, we can expect the symmetry axis to have some deviation from the vertical especially around salt-body flanks. For TI media with a tilt in the axis of symmetry, two additional parameters that describe the tilt in 3D, are needed to fully characterize acoustic wave propagation. These two parameters are often estimated by assuming that the tilt direction is normal to the medium structure or in the direction of the velocity gradient (Alkhalifah and Bednar, 2000; Audebert et al., 2006). Setting the tilt normal to the dip direction has been convenient and practical. Audebert et al. (2006) realized through numerical experimentation that constraining the tilt of the symmetry axis to the structure, in what they referred to as structurally conformable TI (STI) media, results in simplifications in the parameter dependency in which the short-spread focusing becomes decoupled from long-spread behavior. In fact, setting the tilt normal to the dip results in simplified equations for data analysis, as we discussed here.

In this paper, we show explicitly that when we constrain the tilt to be normal to the reflector dip, the behavior of plane waves around the scattering point is explicitly represented by closed-form relations. In fact, the reflection angles for the source and the receiver rays are always equal. Thus, the key is to include this constraint as part of the process, whether it is migration or angle-gather development. As a result, we call the medium dip-constrained TI (DTI) to stress the concept of using this constraint as part of the process as opposed to relating it to the structure of the model. We show that key equations are simplified by this constraint , which will help in boosting the efficiency of such processes. In fact, the DTI model makes processes such as angle-gather decomposition that depend on development around the scattering point simpler than the VTI model.

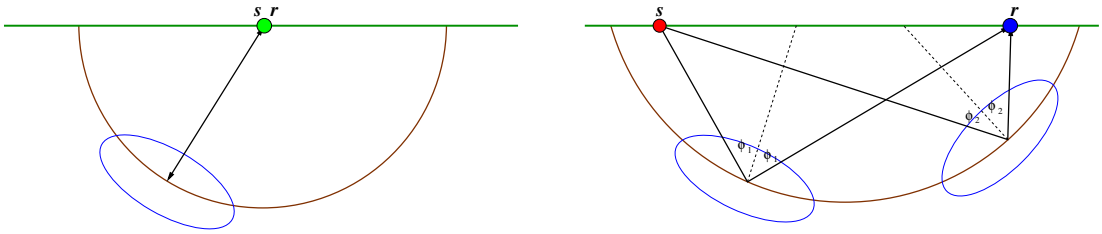

Figure 1: (a) A schematic representation of the tilted transverse isotropy isochron for zero-offset in which the tilt is constrained to the normal of the isochron – the isochron is circular. (b) A similar representation for the non-zero offset case. The angle ϕ is the group angle which is equal for the incident and reflected rays, but differs along the isochron. introDTI/XFig Isochron3,Isochron2

DIP-CONSTRAINED TTI MEDIA

To appreciate the simplification attained from this constraint , we initially restrict our discussions to a homogeneous medium. In this case, the zero-offset isochron, which is representative of the equal traveltime surface, is spherical in shape, equivalent to the isotropic medium isochron, with a radius governed by the velocity in the tilt direction, v_T, as follows:

$$r\left(\mathbf{x}\right) = v_T t\left(\mathbf{x}\right), \tag{1}$$

where t is the time along the wavefront and $\mathbf{x} = \{x, y, z\}$ represents space coordinates. This convenient assertion is only true if we constrain the tilt axis to the direction normal to the reflector dip, and thus the group velocity equals the phase velocity equals the velocity along the tilt. Figure 1(a) shows a schematic plot of the zero-offset isochron with two representative examples of tilt direction that are constrained to be orthogonal to the isochron surface. Though such a medium do not physically exist, it is assumed here in the context of a process, and thus what matters is the local action of the isochron on the reflection, which is similar to the isotropic case.

For non zero-offset case, the traveltime isochron is constrained by the double-square-root (DSR) formula (Claerbout, 1995). Thus, the total traveltime, t, is a combination of traveltimes from the source $\mathbf{s}$ located at (s_x,s_y), and the receiver $\mathbf{r}$ located at (r_x,r_y) to an image point in the subsurface at location $\mathbf{x}$ and is given by the expression

$$\begin{aligned} t &= \sqrt{\frac{(s_x - x)^2 + (s_y - y)^2 + z^2}{v_g^2(\phi)}} \\ &+ \sqrt{\frac{(r_x - x)^2 + (r_y - y)^2 + z^2}{v_g^2(\phi)}}\,, \end{aligned} \tag{2}$$

where $v_g(\phi)$ is the group velocity as a function of group angle ϕ. From Figure 1(b), and considering, for simplicity, that the incident and reflected rays are confined to

the vertical plane, ϕ can be evaluated geometrically as follows:

$$\begin{aligned}\phi &= \frac{1}{2}\cos^{-1}\frac{z}{\sqrt{(s_x-x)^2+(s_y-y)^2+z^2}} \\ &+ \frac{1}{2}\cos^{-1}\frac{z}{\sqrt{(r_x-x)^2+(r_y-y)^2+z^2}}\,,\end{aligned} \tag{3}$$

otherwise we have to project the angles to the plane that constrains the incident and reflected rays. However, evaluating $v_g(\phi)$ in complex media is complicated with no closed-form representation. An alternative is to rely on the phase angle by using plane waves and the Fourier decomposition.

If we reformulate the DSR equation in terms of changes in time, and thus, focus on the plane-wave relation we end up with the following DSR formula:

$$\frac{\partial t}{\partial z} = \sqrt{\frac{1}{v^2(\theta)} - \left(\frac{\partial t}{\partial r}\right)^2} + \sqrt{\frac{1}{v^2(\theta)} - \left(\frac{\partial t}{\partial s}\right)^2}\,, \tag{4}$$

where now v is the phase velocity and has a closed form representation in terms of the phase angle θ given by the acoustic approximation (Alkhalifah, 1998) as follows:

$$\begin{aligned}v^2(\theta) &= \frac{1}{2}\left(v^2(2\eta+1)\sin^2\theta + v_T^2\cos^2\theta\right) \\ &+ \frac{1}{4}\sqrt{a\sin^4\theta + b\sin^2(2\theta) + c\cos^4\theta}\,,\end{aligned} \tag{5}$$

where $a = 4v^4(2\eta+1)^2$, $b = 2v^2v_T^2(1-2\eta)$, $c = 4v_T^4$, v is the NMO velocity with respect to the tilted symmetry axis, and η is the anisotropy parameter relating the NMO velocity to the velocity normal to the tilt. The angle θ in equation 4 is measured from the tilt direction and will also be given by the angle gather as part of the process of downward continuation as we will see later.

Thus, in the non-zero offset case the isochron depends on angle, but it is a single angle for both source and receiver rays and we do not have to worry about relating the two angles, as is the case in VTI and general TTI media. This provides us with analytical relations for plane waves at the reflection point. In this case, both the source and receiver waves have the same wave group velocity that differs along the non-zero offset isochron. In fact, for the zero-dip part of the isochron the reflection angle is at its maximum reducing to zero for a vertical reflector, as seen in Figure 1(b).

Next, we formulate the extended imaging condition, necessary for angle-gather development, for the DTI model. As shown in this section, angle gathers are also necessary for an explicit formulation of downward continuation in a DTI model.

EXTENDED IMAGING CONDITION

Conventional seismic imaging methods share the assumption of single scattering at discontinuities in the subsurface. Under this assumption, waves propagate from

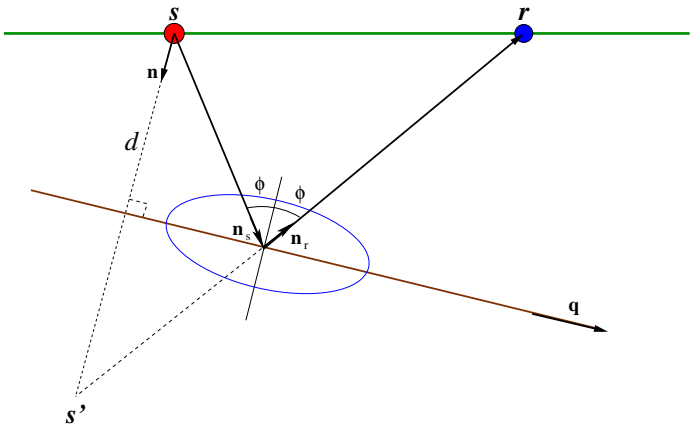

Figure 2: A schematic plot of the reflection geometry for a tilted transversely isotropic medium with a tilt in the dip direction. The incident and reflection angles are the same given by the group angle ϕ. Here, s and r correspond, respectively, to the source and receiver locations, d is the distance between the source and the reflector in the direction given by unit vector $\mathbf{n}$ normal to the reflector with direction described by unit vector $\mathbf{q}$, and $\mathbf{n_s}$ and $\mathbf{n_r}$ are, respectively, the unit vector directions for each of the source and receiver rays with ray angle ϕ measured from the normal to the reflector. introDTI/XFig Reflection

seismic sources, interact with discontinuities and return to the surface as reflected seismic waves. We commonly speak about a "source" wavefield, originating at the seismic source and propagating in the medium prior to any interaction with discontinuities, and a "receiver" wavefield, originating at discontinuities and propagating in the medium to the receivers (Berkhout, 1982; Claerbout, 1985). The two wavefields kinematically coincide at discontinuities. Any mismatch between the wavefields indicates inaccurate wavefield reconstruction typically assumed to be due to inaccurate velocity. In this context, we do not need to make geometrical assumptions about up- or down-going propagation, since waves can move in any direction as long as they scatter only once. We also do not need to make any assumption about how we reconstruct those two wavefields as long as the wave-equation used accurately describes wave propagation in the medium under consideration.

We can formulate imaging as a process involving two steps: the wavefield reconstruction and the imaging condition. The key elements in this imaging procedure are the source and receiver wavefields, u_s and u_r, which depend on space $\mathbf{x}$ and time t. A conventional crosscorrelation imaging condition (cIC) based on the reconstructed wavefields can be formulated as the zero lag of the crosscorrelation between the source and receiver wavefields (Claerbout, 1985):

$$r\left(\mathbf{x}\right) = \sum_{shots} \sum_{\omega} \overline{u_s\left(\mathbf{x},\omega\right)} u_r\left(\mathbf{x},\omega\right), \tag{6}$$

where r represents the migrated image and the over-line represents complex con-

jugation. This operation exploits the fact that portions of the wavefields match kinematically at subsurface positions where discontinuities occur.

An extended imaging condition preserves in the output image certain acquisition (e.g., source or receiver coordinates) or illumination (e.g., reflection angle) parameters (Clayton and Stolt, 1981; Claerbout, 1985; Stolt and Weglein, 1985; Weglein and Stolt, 1999). In shot-record migration, the source and receiver wavefields are reconstructed on the same computational grid at all locations in space and all times or frequencies, therefore there is no a-priori separation that can be transferred to the output image. In this situation, the separation can be constructed by local translations between the two wavefields, either in space (Rickett and Sava, 2002; Sava and Fomel, 2005), or in time (Sava and Fomel, 2006) or in space and time. This separation essentially represents local crosscorrelation lags between the source and receiver wavefields. Thus, an extended crosscorrelation imaging condition (eIC) defines the image as a function of space and crosscorrelation lags in space $\boldsymbol{\lambda}$ and time τ:

$$r\left(\mathbf{x},\boldsymbol{\lambda},\tau\right)=\sum_{shots}\sum_{\omega}e^{2i\omega\tau}\overline{u_s\left(\mathbf{x}-\boldsymbol{\lambda},\omega\right)}u_r\left(\mathbf{x}+\boldsymbol{\lambda},\omega\right)\ . \tag{7}$$

Equation 6 represents a special case of equation 7 for $\boldsymbol{\lambda}=0$ and $\tau=0$. The eIC defined by equation 7 can be used to analyze the accuracy of wavefield reconstruction.

MOVEOUT ANALYSIS

If we restrict the observation to the immediate vicinity of the reflection point, which means that we consider the moveout surface in a small range of lags, we can approximate the typical irregular wavefront in complex media by a plane, although the shapes of wavefronts are arbitrary in heterogeneous media. Following the derivation of Yang and Sava (2009) and using the geometry shown in Figure 2, the source and receiver plane waves are described by:

$$\mathbf{n_s}\cdot\mathbf{x} = v(\theta)t\ , \tag{8}$$
$$\mathbf{n_r}\cdot\left(\mathbf{x}-2d\mathbf{n}\right) = v(\theta)t\ , \tag{9}$$

where $\mathbf{n_s}$ and $\mathbf{n_r}$ are the unit direction vectors of the source and receiver plane waves, respectively, $\mathbf{n}$ is the unit vector orthogonal to the reflector at the image point, and vector $\mathbf{x}$ indicates the image point position. v is defined as the phase velocity in the locally homogeneous medium around the reflection point, and thus it is identical for both wavefields. θ is half the scattering angle (reflection angle).

We can also obtain the shifted source and receiver plane waves by introducing the space- and time-lags

$$\mathbf{n_s}\cdot\left(\mathbf{x}+\boldsymbol{\lambda}\right) = v(\theta)\left(t+\tau\right)\ , \tag{10}$$
$$\mathbf{n_r}\cdot\left(\mathbf{x}-2d\mathbf{n}-\boldsymbol{\lambda}\right) = v(\theta)\left(t-\tau\right)\ . \tag{11}$$

Solving the system of equations 10-11 leads to the expression

$$(\mathbf{n_s} - \mathbf{n_r}) \cdot \mathbf{x} = 2v(\theta)\tau - (\mathbf{n_s} + \mathbf{n_r}) \cdot \boldsymbol{\lambda} - 2d\mathbf{n_r} \cdot \mathbf{n} \ , \tag{12}$$

which characterizes the moveout function (surface) of space- and time-lags at a common-image point.

Furthermore, we have the following relations for the reflection geometry:

$$\mathbf{n_s} - \mathbf{n_r} = 2\mathbf{n}\cos\theta \ , \tag{13}$$
$$\mathbf{n_s} + \mathbf{n_r} = 2\mathbf{q}\sin\theta \ , \tag{14}$$

where $\mathbf{n}$ and $\mathbf{q}$ are unit vectors normal and parallel to the reflection plane, respectively, and θ is the reflection angle. Vector $\mathbf{q}$ characterizes the line representing the intersection of the reflection and the reflector planes. Combining equations 12-14, we obtain the moveout function for plane waves:

$$z\left(\boldsymbol{\lambda}, \tau\right) = d_0 - \frac{\tan\theta\left(\mathbf{q} \cdot \boldsymbol{\lambda}\right)}{n_z} + \frac{v(\theta)\tau}{n_z \cos\theta} \ . \tag{15}$$

The quantity d_0 is defined as

$$d_0 = \frac{d - (\mathbf{c} \cdot \mathbf{n})}{n_z} \ , \tag{16}$$

and represents the depth of the reflection corresponding to the chosen common-image gather (CIG) location. This quantity is invariant for different plane waves, thus assumed constant here. The vector $\mathbf{c}$ is along the Earth's surface given by $(x, y, 0)$.

When incorrect velocity is used for imaging, and thus, an inaccurate reflection angle is assumed, based on the analysis in the preceding section, we can obtain the moveout function

$$z\left(\boldsymbol{\lambda}, \tau\right) = d_{0f} - \frac{\tan\theta_m\left(\mathbf{q}_m \cdot \boldsymbol{\lambda}\right)}{n_{mz}} + \frac{v_m(\theta_m)\left(\tau - t_d\right)}{n_{mz}\cos\theta_m} \ , \tag{17}$$

where d_{0f} is the focusing depth of the corresponding reflection point, v_m is the migration velocity, t_d is the focusing error, $\mathbf{n}_m$ and $\mathbf{q}_m$ are vectors normal and parallel to the migrated reflector, respectively. Equation 17 describes the extended images moveout for a single seismic experiment and it is essentially identical to the similar formula obtained by Yang and Sava (2009) for isotropic media, but for using the phase velocity instead of the isotropic velocity.

ANGLE DECOMPOSITION

In downward continuation methods, theoretical analysis of angle gathers can be reduced to analyzing the geometry of reflection in the simple case of a dipping reflector in a locally homogeneous medium (Sava and Fomel, 2005). The behavior of plane waves in the vicinity of the reflection point is sufficient for deriving relationships for

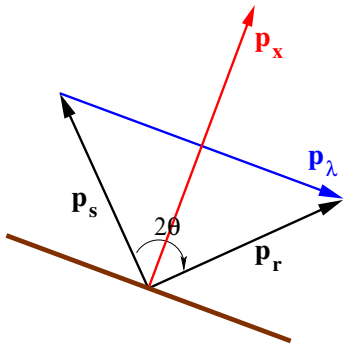

Figure 3: A schematic plot depicting the relation between source and receiver ray-parameter vectors ($\mathbf{p_s}$ and $\mathbf{p_r}$) and that of the space-lag and position ($\mathbf{p_\lambda}$ and $\mathbf{p_x}$). The angle θ corresponds to the phase angle direction of the plane wave. introDTI/XFig rayparameters

local reflection traveltime derivatives (Goldin, 1986). The geometry of the reflection ray paths is depicted in Figure 2.

Using the standard notations for the source and receiver coordinates: $\mathbf{s} = \mathbf{x} + \boldsymbol{\lambda}$ and $\mathbf{r} = \mathbf{x} - \boldsymbol{\lambda}$, the traveltime from a source to a receiver is a function of all spatial coordinates of the seismic experiment $t = t(\mathbf{x}, \boldsymbol{\lambda})$. Differentiating t with respect to all components of the vectors $\mathbf{x}$ and $\boldsymbol{\lambda}$, and using the standard notations to represent slownesses $\mathbf{p}_\alpha = \nabla_\alpha t$, where $\alpha = (\mathbf{x}, \boldsymbol{\lambda}, \mathbf{s}, \mathbf{r})$, we can write:

$$\mathbf{p_x} = \mathbf{p_r} + \mathbf{p_s} \; , \tag{18}$$

$$\mathbf{p_\lambda} = \mathbf{p_r} - \mathbf{p_s} \; . \tag{19}$$

By analyzing the geometric relations of various vectors at an image point (Figures 3), we can write the following trigonometric expressions:

$$|\mathbf{p_\lambda}|^2 = |\mathbf{p_s}|^2 + |\mathbf{p_r}|^2 - 2|\mathbf{p_s}||\mathbf{p_r}|\cos(2\theta) \; , \tag{20}$$

$$|\mathbf{p_x}|^2 = |\mathbf{p_s}|^2 + |\mathbf{p_r}|^2 + 2|\mathbf{p_s}||\mathbf{p_r}|\cos(2\theta) \; . \tag{21}$$

Defining $\mathbf{k_x}$ and $\mathbf{k_\lambda}$ as the position and lag (or offset) wavenumber vectors, we can replace $\mathbf{p} = \mathbf{k}/\omega$. Using the trigonometric identities

$$1 - \cos(2\theta) = 2\sin^2(\theta) \; , \tag{22}$$

$$1 + \cos(2\theta) = 2\cos^2(\theta) \; , \tag{23}$$

and assuming $|\mathbf{p_s}| = |\mathbf{p_r}| = s(\theta)$, where $s(\theta) = 1/v_p(\theta)$ is the phase slowness as a function of phase angle at an image location, we obtain the following relations:

$$|\mathbf{k_\lambda}|^2 = (2\omega s(\theta)\sin(\theta))^2 \; , \tag{24}$$

$$|\mathbf{k_x}|^2 = (2\omega s(\theta)\cos(\theta))^2 \; , \tag{25}$$

$$\mathbf{k_\lambda}.\mathbf{k_x} = 0 \; . \tag{26}$$

We can eliminate from equations 24- 25 the dependence on the depth axis and obtain an angle decomposition formulation prior to imaging. Thus, if we eliminate k_z and k_{λ_z}, we obtain the expression:

$$\begin{aligned}(k_x{}^2 + k_y{}^2)(2\omega s(\theta)\sin\theta)^2 + (k_{\lambda_x}{}^2 + k_{\lambda_y}{}^2)(2\omega s(\theta)\cos\theta)^2 = \\ (k_x k_{\lambda_y} - k_y k_{\lambda_x})^2 + (2\omega s(\theta)\sin\theta)^2(2\omega s(\theta)\cos\theta)^2 \ .\end{aligned} \tag{27}$$

The quadratic equation 27 can be used to map data from space-lag gathers (k_{λ_x}, k_{λ_y}) into angle coordinates θ, prior to imaging. For 2D data, equation 27 takes the simpler form

$$\begin{aligned}k_x{}^2(2\omega s(\theta)\sin\theta)^2 + k_{\lambda_x}{}^2(2\omega s(\theta)\cos\theta)^2 = \\ (2\omega s(\theta)\sin\theta)^2(2\omega s(\theta)\cos\theta)^2,\end{aligned} \tag{28}$$

which can be solved for an explicit mapping of k_{λ_x} to θ.

Note that the angle decomposition formula 28 reduces to a form simpler than that shown by Alkhalifah and Fomel (2009) for VTI media. This angle decomposition is particularly useful in imaging via downward continuation, as discussed next.

DOWNWARD CONTINUATION

The angle decomposition discussed in the preceding section allows us to produce angle gathers after downward continuation in DTI media. Wavefield reconstruction for multi-offset migration based on the one-way wave-equation under the survey-sinking framework (Claerbout, 1985) is implemented by recursive phase-shift of prestack wavefields

$$u_{z+\Delta z}\left(\mathbf{m},\mathbf{h}\right) = e^{-ik_z\Delta z}u_z\left(\mathbf{m},\mathbf{h}\right) \ , \tag{29}$$

followed by extraction of the image at time $t = 0$. Here, $\mathbf{m}$ and $\mathbf{h}$ represent the midpoint and half-offset coordinates, which are equivalent with the space and space-lag variables discussed earlier, but restricted to the horizontal plane. In equation 29, $u_z\left(\mathbf{m},\mathbf{h}\right)$ represents the acoustic wavefield for a given frequency ω at all midpoint positions $\mathbf{m}$ and half-offsets $\mathbf{h}$ at depth z, and $u_{z+\Delta z}\left(\mathbf{m},\mathbf{h}\right)$ represents the same wavefield extrapolated to depth $z + \Delta z$. The phase shift operation uses the depth wavenumber k_z which is defined in 2D by the DSR equation 4 as follows:

$$k_z = \sqrt{\omega^2 s^2(\theta) - \left(k_m - k_h\right)^2} + \sqrt{\omega^2 s^2(\theta) - \left(k_m + k_h\right)^2} \ , \tag{30}$$

where k_h is equivalent to k_{λ_x}.

Figure 4 shows k_z as a function of the midpoint wavenumber and the reflection angle for a DTI model characterized by $\eta = 0.3$ (left). As expected, the range of angles reduces with increasing dip angle (or k_m). The phase shift per depth is maximum for horizontal reflector ($k_m = 0$) and zero offset (equivalent with $\theta = 0$). The right plot in Figure 4 shows the difference between the k_z for this DTI model and that for an

isotropic model with velocity equal to $v = 1.8$ km/s. As expected, for zero reflection angle, the DTI phase shift is given by the isotropic operator as we discussed earlier. For the non-zero-offset case, the difference increases with the reflection angle.

To use k_z in this form we need to evaluate the reflection angle, θ, in the downward continuation process as the angle gather defines the phase angle needed for equation 30. Equation 28 provides a one-to-one relation between angle gathers and the offset wavenumber. However, to insure an explicit evaluation we formulate the problem as a mapping process to find the wavefield for a given offset wavenumber k_h that corresponds to a particular reflection angle. As a result, we can devise an algorithm for downward continuation for a wavefield with sources and receivers at depth z as follows:

- For a given reflection angle, use equation 28 to find the corresponding k_h $(= k_{\lambda_x})$.
- Using $k_h(\theta)$, map $u(k_m, k_h, \omega, z)$ to $u(k_m, \theta, \omega, z)$ (the angle decomposition).
- Apply the imaging condition by summing over frequencies ω to obtain imaged angle gathers.
- Apply phase shift to the wavefield $u(k_m, k_h, \omega, z)$ to obtain $u(k_m, k_h, \omega, z + \Delta z)$ by equation 29 using the depth wavenumber given by equation 30.
- Repeat the steps for depth $z = z + \Delta z$.

The process provides imaged angle gathers in DTI media. This approach also allows us to better treat illumination as we downward continue while keeping the sampling in reflection angle uniform.

DOMAIN OF APPLICABILITY

The reflector dip TI tilt constraint introduced here for imaging simplification purposes is not applicable everywhere. In fact, setting such a constraint inherently suggests smooth interfaces as it is impossible to impose such a constraint on a diffractor. The smooth interface is also required by the plane wave assumption used in the angle gather development. Thus, we are suggesting DTI as a model development tool in which this suggested assumption is typically used in areas like the Gulf of Mexico. Thus, the DTI model must be extracted from reflections that adhere to this constraint , which do not include salt flanks. This is convenient in building the model around the salt and even subsalt. While the top-of-salt reflections do not adhere to this constraint , the bottom reflections do as isotropy is a special case of DTI with the anisotropy parameters $\eta = \delta = 0$. In addition, subsalt reflections also satisfy this constraint whether such reflections are within isotropic media or an assumed DTI condition. It does not matter that the rays may have traveled through media that is VTI or general TTI, what matters is the behavior at the reflection point for applications like DTI imaging or angle gather analysis.

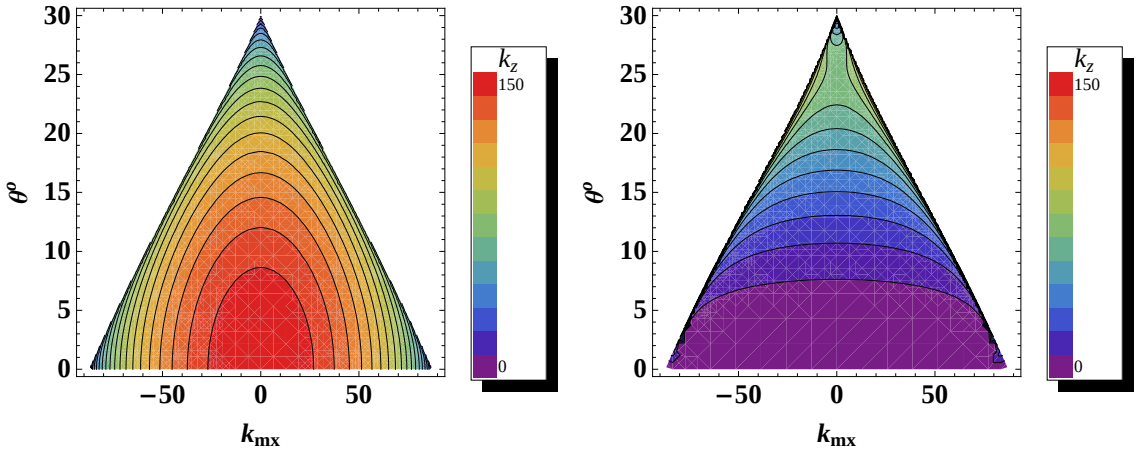

Figure 4: A plot of the vertical wavenumber, k_z, as a function of midpoint wavenumber and angle gather for a dip-constrained transversely isotropic (DTI) model with 2NMO velocity, v=2.0 km/s, titled direction velocity, v_T=1.8 km/s, and $\eta = 0.3$ (left) and the difference in k_z between the DTI model and an isotropic model with v=1.8 km/s (right). The wave numbers are given in units of km^{-1}. introDTI/Math kz

CONCLUSIONS

Constraining the tilt of a transversely isotropic medium normal to the reflector dip (DTI) allows for explicit formulations of plane waves around the scattering point. These formulations form the basis for angle decomposition or the moveout analysis in the extended image condition domain. As a result, DTI is a convenient model for anisotropy parameter estimation in media in which such models are applicable. This model also allows us to use the general TTI assumption in a simplified form that better fits the information embedded in the recorded data.

ACKNOWLEDGMENTS

We are grateful to KAUST and to the sponsors of the Center for Wave Phenomena at Colorado School of Mines for their support. We thank the associate editor and the reviewers for their critical review of the letter.

REFERENCES

Alkhalifah, T., 1997, Seismic data processing in vertically inhomogeneous TI media: Geophysics, **62**, 662–675.

———, 1998, Acoustic approximations for processing in transversely isotropic media: Geophysics, **63**, 623–631.

Alkhalifah, T., and J. Bednar, 2000, Building a 3-D anisotropic model: Its implications to traveltime calculation and velocity analysis: 70th Ann. Internat. Mtg, Soc. of Expl. Geophys., 965–968.

Alkhalifah, T., and S. Fomel, 2009, Angle gathers in wave-equation imaging for vti media: SEG Technical Program Expanded Abstracts, **28**, 2899–2903.

Alkhalifah, T., and K. Larner, 1994, Migration error in transversely isotropic media: Geophysics, **59**, 1405–1418.

Alkhalifah, T., and I. Tsvankin, 1995, Velocity analysis for transversely isotropic media: Geophysics, **60**, 1550–1566.

Audebert, F. S., A. Pettenati, and V. Dirks, 2006, TTI anisotropic depth migration - which tilt estimate should we use?: EAGE, Expanded Abstracts, P185.

Ball, G., 1995, Estimation of anisotropy and anisotropic 3-D prestack depth migration, offshore Zaire: Geophysics, **60**, 1495–1513.

Berkhout, A. J., 1982, Imaging of acoustic energy by wave field extrapolation: Elsevier.

Claerbout, J. F., 1985, Imaging the Earth's interior: Blackwell Scientific Publications.

———, 1995, Basic Earth Imaging: Stanford Exploration Project.

Clayton, R. W., and R. H. Stolt, 1981, A Born-WKBJ inversion method for acoustic reflection data: Geophysics, **46**, 1559–1567.

Goldin, S. V., 1986, Seismic Traveltime Inversion: Soc. of Expl. Geophys.

Huang, T., S. Xu, J. Wang, G. Ionescu, and M. Richardson, 2008, The benefit of tti tomography for dual azimuth data in gulf of mexico: SEG, Expanded Abstracts, **27**, 222–226.

Isaac, J. H., and D. C. Lawton, 2004, A practical method for estimating effective parameters of anisotropy from reflection seismic data: Geophysics, **69**, 681–689.

Martinez, R. D., and S. Lee, 2002, A strategy for anisotropic P-wave prestack imaging: SEG, Expanded Abstracts, **21**, 149–152.

Ohlsen, F., and C. MacBeth, 1999, Elliptical anisotropy: Regression or advance?: SEG, Expanded Abstracts, **18**, 1600–1603.

Rickett, J., and P. Sava, 2002, Offset and angle-domain common image-point gathers for shot-profile migration: Geophysics, **67**, 883–889.

Sava, P., and S. Fomel, 2005, Coordinate-independent angle-gathers for wave equation migration: 75th Annual International Meeting, SEG, Expanded Abstracts, 2052–2055.

———, 2006, Time-shift imaging condition in seismic migration: Geophysics, **71**, S209–S217.

Stolt, R. H., and A. B. Weglein, 1985, Migration and inversion of seismic data: Geophysics, **50**, 2458–2472.

Weglein, A. B., and R. H. Stolt, 1999, Migration-inversion revisited (1999): The

Leading Edge, **18**, 950–952.

Yang, T., and P. Sava, 2009, Moveout analysis of wave-equation extended images: Geophysics, submitted for publication.

Zhou, H., D. Pham, S. Gray, and B. Wang, 2004, Tomographic velocity analysis in strongly anisotropic tti media: SEG, Expanded Abstracts, **23**, 2347–2350.

Acoustic wavefield evolution as function of source location perturbation

Tariq Alkhalifah[1]

ABSTRACT

The wavefield is typically simulated for seismic exploration applications through solving the wave equation for a specific seismic source location. The direct relation between the form (or shape) of the wavefield and the source location can provide insights useful for velocity estimation and interpolation. As a result, I derive partial differential equations that relate changes in the wavefield shape to perturbations in the source location, especially along the Earth's surface. These partial differential equations have the same structure as the wave equation with a source function that depends on the background (original source) wavefield. The similarity in form implies that we can use familiar numerical methods to solve the perturbation equations, including finite difference and downward continuation. In fact, we can use the same Green's function to solve the wave equation and its source perturbations by simply incorporating source functions derived from the background field. The solutions of the perturbation equations represent the coefficients of a Taylor's series type expansion of the wavefield as a function of source location. As a result, we can speed up the wavefield calculation as we approximate the wavefield shape for sources in the vicinity of the original source. The new formula introduces changes to the background wavefield only in the presence of lateral velocity variation or in general terms velocity variations in the perturbation direction. The approach is demonstrated on the smoothed Marmousi model.

INTRODUCTION

The wave equation is the central ingredient in simulating and constraining wave propagation in a given medium. No other formulation, including the eikonal equation or ray tracing, can be as conclusive and elaborate (includes most traveltime and amplitude aspects) as does the full elastic wave equation [Aki and Richards (1980)]. Thus, the wave equation has the near complete far-field description of the wave behavior for a given velocity function. To reduce the computational cost, P-wave propagation in the Earth's subsurface is approximately simulated by numerically solving the acoustic wave equation. The wavefield in acoustic media is described by a scalar quantity.

[1]**e-mail:** tkhalfah@kacst.edu.sa

Kinematically, for P-waves in the far field of the source, the acoustic and elastic wave equations are similar; they both yield the same eikonal equation in isotropic media.

The first-order dependence of wavefields, and specifically the acoustic wave equation, on media parameters is described by the Born approximation. It is a single scattering approximation, used in seismic applications to approximate the perturbed wavefield due to a small perturbation of the reference medium. It is also, in its inverse form, used to help infer medium parameters from observed wavefields (Cohen and Bleistein, 1977; Panning et al., 2009). In the spirit of the Born approximation, the partial differential equations, introduced here, describe the wavefield shape first and second order dependence on a source location perturbation. Data evolution as a function of changes in acquisition parameters goes back to the development of normal moveout and the transformation of common-offset seismic gathers from one constant offset to another (Bolondi et al., 1982). Bagaini and Spagnolini (1996) identified offset continuation (OC) with a whole family of prestack continuation operators, such as shot continuation (Bagaini and Spagnolini, 1993), dip moveout as a continuation to zero offset (Hale, 1991; Alkhalifah, 1996), and three-dimensional azimuth moveout (Biondi et al., 1998). Even residual operators between different medium parameters or acquisition configurations are described by Alkhalifah and Biondi (2004) and Alkhalifah (2005). All these methods are based on a geometrical optics development using constant velocity approximations.

Alkhalifah and Fomel (2009) suggested a plane wave source perturbation expansion for the eikonal equation. Their approach rendered linearized forms of the eikonal equation capable of predicting the traveltime field for a shift in the source location represented by a shift in the velocity field in the opposite direction. The development here follows the same approach applied now to the wave equation. The major result in the eikonal application is the linearized forms of the new perturbation equations extracted from the conventionally nonlinear eikonal partial differential equation.

The source perturbation introduced here is based on a plane wave expansion around the source. For homogeneous or vertically inhomogeneous media, the wavefield calculated for a source in any location along the horizontal surface is valid in all other locations, and as a result no modifications are needed. For laterally inhomogeneous media, this statement is no longer true and the difference in the wavefield depends on the complexity of the lateral velocity variation. In this paper, I develop partial differential equations that approximately predict such changes, and thus, can be used to simulate wavefields for sources at other positions in the vicinity of the original source. Figure 1 illustrates the concept of wavefield evolution as a function of source perturbation in which the wavefield evolves as a function of source location perturbation l granted that the velocity field changes laterally. In Figure 1, the wavefield wavefront schematic reaction depicts a general velocity decrease with l. In this paper, we consider source perturbation in the lateral direction, which adheres to our familiarity with surface seismic exploration applications. However, equivalent perturbations may be applied in the depth direction as well, as Alkhalifah and Fomel (2009) showed for the eikonal equation, which may have applications in datuming.

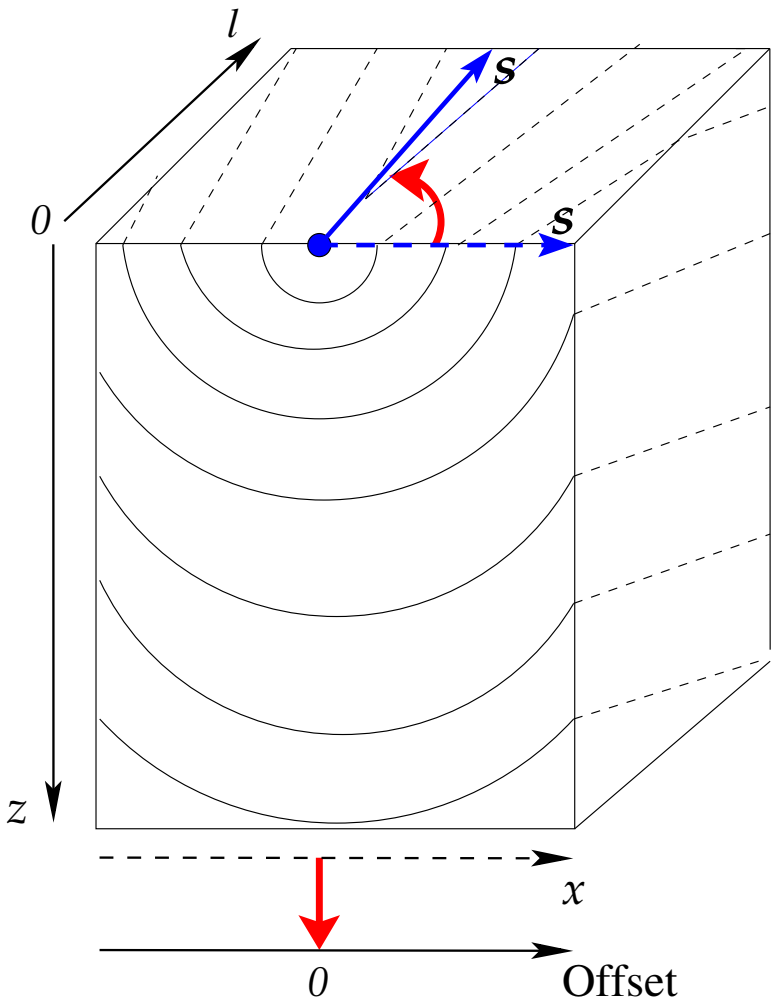

Figure 1: Illustration of the evolution of the two-dimensional wavefield given by distance, x, and depth, z, as a function of the shift in the source location, l. The actual source shift is transformed to a new 3rd axis, where the x axis now describes the offset from the source. The dot in the middle on the surface represents the source location. waveds/XFig SourcePert2

THEORY

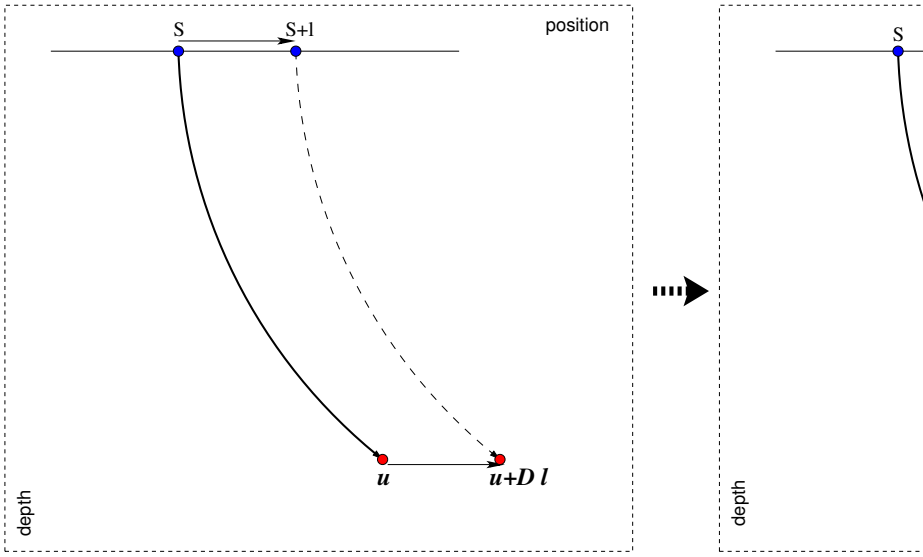

Figure 2: Illustration of the relation between the initial source location and a perturbed version given by a single source and image point locations. This is equivalent to a shift in the velocity field laterally by l. waveds/XFig timedsS

In this section, I derive partial differential equations that relate changes in the wavefield shape to perturbations in the source location. We will start by taking derivatives of the wave equation with respect to lateral perturbation and then use the Taylor's series expansion to predict the wavefield form at another source.

In 3-D media, the acoustic wavefield u is described as a function of x, y and depth z and is governed by a partial differential equation as a function of time t given by,

$$\frac{\partial^2 u}{\partial x^2}+\frac{\partial^2 u}{\partial y^2}+\frac{\partial^2 u}{\partial z^2}=w(x,y,z)\frac{\partial^2 u}{\partial t^2}+f(x,y,z,t), \tag{1}$$

where $w(x,y,z)$ is the sloth (slowness squared) as a function position. The source can be included as a function added to equation (1) given by $f(x,y,z,t)$, defined usually at a point, or represented by the wavefield $u(x,y,z,t)$ around time $t=0$ as an initial condition. A change in the source location along the surface,while keeping its source function stationary, is equivalently represented, in the far field, by shifting the velocity field laterally by the same amount in the opposite direction and thus can be represented by the following wave equation form:

$$\frac{\partial^2 u}{\partial x^2}+\frac{\partial^2 u}{\partial y^2}+\frac{\partial^2 u}{\partial z^2}=w(x-l,y,z)\frac{\partial^2 u}{\partial t^2}+f(x,y,z,t), \tag{2}$$

where $f(x,y,z,t)$, in this case, is stationary and independent of l. A simple variable change of $x^{'}=x-l$ can demonstrate this assertion, where $x^{'}$ is replaced by x to simplify notation. For simplicity, I use the symbol u to describe the new wavefield, as well. Figure 2 shows the depicts the relation for a single source and image point combination with the velocity shift. To evaluate the wavefield response to lateral perturbations, we take the derivative of equation (2) with respect to l, where the

wavefield is dependent on the source location as well $[u(x, y, z, l, t)]$, which yields:

$$\frac{\partial^3 u}{\partial x^2 \partial l} + \frac{\partial^3 u}{\partial y^2 \partial l} + \frac{\partial^3 u}{\partial z^2 \partial l} = -\frac{\partial w}{\partial x}\frac{\partial^2 u}{\partial t^2} + w\frac{\partial^3 u}{\partial t^2 \partial l}. \tag{3}$$

Substituting $D_x = \frac{\partial u}{\partial l}$, where l is the equivalent source shift (actual velocity shift) in the x-direction, into equation (3), and setting $l = 0$, the location in which we evaluate the equation for the Taylor's series expansion yields:

$$\frac{\partial^2 D_x}{\partial x^2} + \frac{\partial^2 D_x}{\partial y^2} + \frac{\partial^2 D_x}{\partial z^2} = w(x, y, z)\frac{\partial^2 D_x}{\partial t^2} - \frac{\partial w}{\partial x}\frac{\partial^2 u}{\partial t^2}, \tag{4}$$

which has the form of the wave equation with the last term on the right hand side acting as a source function. If this source function is zero given by, for example, no lateral velocity variation ($\frac{\partial w}{\partial x}$=0), then D_x=0, and as expected there will be no change in the wavefield form with a change in source position.

Therefore, the wavefield for a source located at a distance l from the source used to estimate the wavefield u can be approximated using the following Taylor's series expansion:

$$u(x, y, z, l, t) \approx u(x, y, z, l = 0, t) + D_x(x, y, z, t)l. \tag{5}$$

This result obviously has first-order accuracy represented by the first order Taylor's series expansion. For higher order accuracy, we take the derivative of equation (3) again with respect to l, which yields:

$$\frac{\partial^4 u}{\partial x^2 \partial l^2} + \frac{\partial^4 u}{\partial y^2 \partial l^2} + \frac{\partial^4 u}{\partial z^2 \partial l^2} = \frac{\partial^2 w}{\partial x^2}\frac{\partial^2 u}{\partial t^2} - 2\frac{\partial w}{\partial x}\frac{\partial^3 u}{\partial t^2 \partial l} + w\frac{\partial^4 u}{\partial t^2 \partial l^2}. \tag{6}$$

Again, by substituting $D_{xx} = \frac{\partial^2 u}{\partial l^2}$, as well as, D_x into equation (6) , and setting $l = 0$, the second order perturbation equation is given by:

$$\frac{\partial^2 D_{xx}}{\partial x^2} + \frac{\partial^2 D_{xx}}{\partial y^2} + \frac{\partial^2 D_{xx}}{\partial z^2} = w\frac{\partial^2 D_{xx}}{\partial t^2} - 2\frac{\partial w}{\partial x}\frac{\partial^2 D_x}{\partial t^2} + \frac{\partial^2 w}{\partial x^2}\frac{\partial^2 u}{\partial t^2}. \tag{7}$$

Now, the wavefield for a source located at a distance l from the original source can be approximated using the following second-order Taylor's series expansion:

$$u(x, y, z, l, t) \approx u(x, y, z, l = 0, t) + D_x(x, y, z, t)l + \frac{1}{2}D_{xx}(x, y, z, t)l^2. \tag{8}$$

Equations (4) and (7) can be solved in many ways and in the next section I show some of the features gained by using an integral formulation given by the Green's function.

THE GREEN'S FUNCTION

The Green's function represents the response and behavior of the wavefield if the source was a point impulse given theoretically by the Dirac delta function. The function allows us to solve the wave equation using an integral formulation as we convolve the Green's function with a source function. The most complicated part of this type of solution of the wave equation is the construction of the Green's function. Kirchhoff modeling and migration is a special case of this type of integral solution and provides incredible speed upgrades over finite difference implementations with some loss in quality, because of the limitations in the calculation of the phase and amplitude components of the Green's function.

Since Green's function for the wave equation satisfies the following formula:

$$\frac{\partial^2 G}{\partial x^2}+\frac{\partial^2 G}{\partial y^2}+\frac{\partial^2 G}{\partial z^2}=w(x,y,z)\frac{\partial^2 G}{\partial t^2}+\delta(\mathbf{x}-\mathbf{x_0})\delta(t-t_0), \tag{9}$$

where δ is the Dirac delta function, with $\mathbf{x_0}$ (x_0, y_0, z_0), and t_0 is the possible location and time of the source pulse, respectively. The solution of equation (1) with a source function $f(\mathbf{x_0},t_0)$ is given by

$$u(x,y,z,t)=\int\int G(\mathbf{x},\mathbf{x_0},t,t_0)f(\mathbf{x_0},t_0)d\mathbf{x_0}dt_0. \tag{10}$$

In typical imaging applications, the Green's function is evaluated upfront and stored in tables for use in prestack modeling and migration. For source perturbations, these stored Green's functions can be used to approximate the wavefield for a shift in the source location by using a source function that is based on Taylor's series expansion, without the need to modify the Green's function. Specifically, considering that in the first-order perturbation equation (4):

$$f_l(x,y,z,t)=-\frac{\partial w}{\partial x}\frac{\partial^2 u}{\partial t^2}, \tag{11}$$

then since equation (4) has the same form as the wave equation with the same velocity function,

$$D_x(x,y,z,t)=\int\int G(\mathbf{x},\mathbf{x_0},t,t_0)f_l(\mathbf{x_0},t_0)d\mathbf{x_0}dt_0. \tag{12}$$

The same argument holds for the second-order perturbation equation (7) with a slightly more complicated source function given by

$$f_{ll}(\mathbf{x_0},t_0)=-2\frac{\partial w}{\partial x}\frac{\partial^2 D_x}{\partial t^2}+\frac{\partial^2 w}{\partial x^2}\frac{\partial^2 u}{\partial t^2}. \tag{13}$$

Thus, the wavefield form can be approximated for a source perturbed a distance l using

$$u(x,y,z,l,t)\approx\int\int G(\mathbf{x},\mathbf{x_0},t,t_0)\left(f(\mathbf{x_0},t_0)+f_l(\mathbf{x_0},t_0)l+\frac{1}{2}f_{ll}(\mathbf{x_0},t_0)l^2\right)d\mathbf{x_0}dt_0. \tag{14}$$

Thus, the wavefield corresponding to a certain source location can be directly evaluated using the background Green's function with a modified source function, and these modifications, unlike the conventional ones, are dependent on lateral velocity variations.

THE IMPLEMENTATION

As we have seen earlier, the equations associated with the wavefield perturbation has a form similar to the wave equation. As a result, any of the methods typically used to solve the wave equation suffices for the perturbation partial differential equations. The most general and straightforward of these methods is the finite-difference approach. With proper space and time grid distribution this method provides acceptable solutions regardless of the complexity of the velocity model. Its only limitation is the relative slow execution speed.

To apply the source perturbation, I first solve the original wave equation for a particular point source as a background field for the perturbation step. In the process, we store the Laplacian evaluation as they are needed for the perturbation calculation. Using an initial condition of $D_x(x, z, t = 0)$=0, we can solve for D_x using equation (4) and add the solution to the original wavefield using equation 8, and thus, obtain a new wavefield shape approximating that for another source location. For higher-order accuracy, we also solve for D_{xx} using equation (7) with a similar initial condition, $D_{xx}(x, z, t = 0)$=0, and include it in the Taylor's series expansion with terms from the solutions of the original background source and D_x.

To avoid potential problems with the storage requirement especially in 3D, we can solve the wave equation and the corresponding perturbation equations simultaneously, and thus, use the already evaluated derivatives (Laplacian) directly. In this case, the cost of the perturbation finite difference application is similar to the cost of solving the wave equation. Thus, the cost of the first and second order expansions to obtain the wavefield for other sources is equivalent to two and three times, respectively, of the cost of solving the wave equation for a single source. However, the information obtained approximates the wavefield for infinite source possibilities in the vicinity of the original source.

Since the perturbation equations have the same form as the wave equation they adhere to the same Courant-Friedrichs-Lewy (CFL) condition [Courant et al. (1928)]. Thus, the time step is constrained by the grid spacing, which in turn relies on velocity, based on the following formula:

$$\frac{\min(\Delta x, \Delta y, \Delta z)}{\Delta t} > \sqrt{3}v \tag{15}$$

where Δt is the time step interval and Δx, Δy, and Δz are the grid spacing along the main axes and v is the velocity.

EXAMPLES

I test the developed partial differential equations on two examples: a simple lens velocity model and the complex Marmousi model. In both cases, I compare the wavefields obtained from a direct finite difference solution of the wave equation for a particular source to that obtained by perturbing the solution from a nearby source using the first and second order approximations. In the Marmousi case, I also compare the resulting surface recorded synthetic data for all options.

A lens

Since the differential equation depends on velocity changes in the direction of the perturbation, we test the methodology on a model that contains a lens anomaly in an otherwise homogeneous medium with a velocity of 2 km/s (Figure 3). The lens apex is located at 600 meters laterally and 500 meters in depth with a velocity perturbation of +250 m/s (or 12.5%). The lens has a diameter of 300 meters. Using this model we will test the accuracy of the first- and second-order perturbation equations.

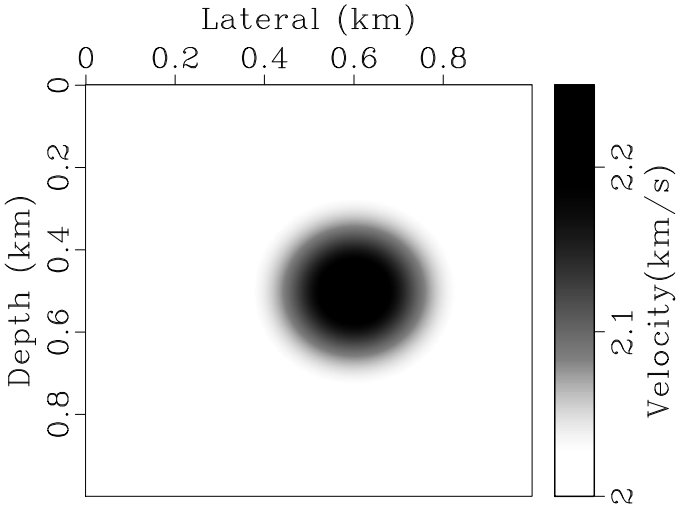

Figure 3: A velocity model containing a lens in an otherwise homogeneous background with a velocity of 2 km/s. waveds/svmod model

For a source located at the surface 0.3 km from the origin, I apply a second-order in time and fourth-order in space finite difference approximation to the wave equation as well as the perturbation equations to simulate a source 50 meters away from the original source position along the surface. A separate direct finite difference calculation using the wave equation is done for a source at 0.35 km location for comparison. Figure 4 shows a snap shot at time 0.5 seconds of the wavefield generated for the source at 0.35 km (left), as well as the snap shot at the same time for the perturbed wavefields using the first-order approximation (middle) and the second order approximation (right). All three wavefields look similar.

However, if we subtract the actual wavefield for the 0.3 km source from that of the 0.35 km one after we superpose the sources we obtain the difference between the

wavefields. This difference occurs only if there is lateral velocity variation. Since there are no lateral variations in the velocity field in Figure 3 prior to wavefront from the source crossing the lens we expect that the difference snapshot plots are zero. However, at time 0.3 s the difference, where the wavefront starts to interact with the lens as shown in Figure 5, appears as expected largest for the unperturbed case (left), while the differences for the perturbed case are much smaller, especially in the case of the second-order expansion. All three plots in Figure 5 are displayed using the same range, for easy comparison, and this range is maintained for all Figures in this section.

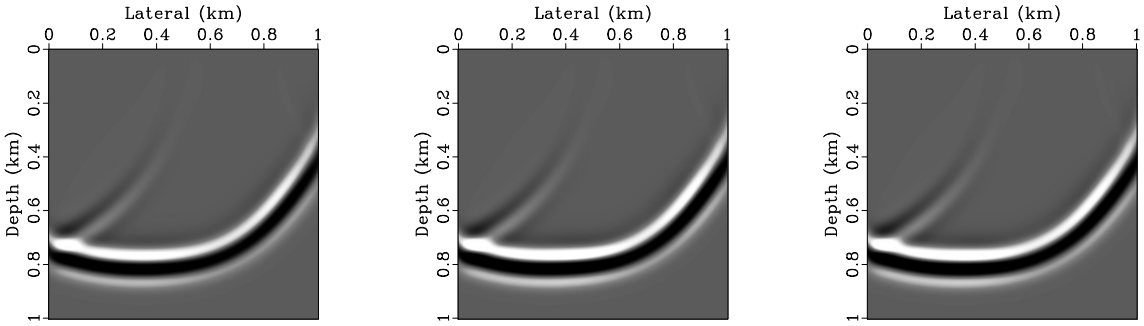

Figure 4: A snap shot at time 0.5 seconds of the wavefield obtained from solving the conventional wave equation using the velocity model in Figure 3 for a source located at surface at 0.35 km (left), a snap shot of the wavefield by perturbing the 0.3 km source wavefield to approximate the 0.35 km one using the first order approximation (middle), and using the second order approximation (right). waveds/svmod timeSide20

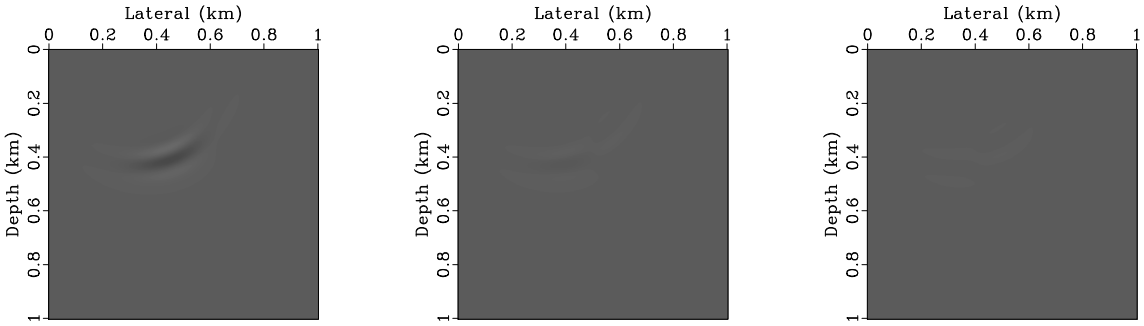

Figure 5: A snap shot at time 0.3 seconds of the difference between the 0.35 km source wavefield and the 0.3 km source wavefield after superimposing the sources (left), the difference after using the first order perturbation on the 0.3 km source wavefield (middle), and after using the second-order perturbation on it (right). All three plots are displayed using the same range, for comparison purposes, and this range is maintained in all Figures corresponding to this lens example. waveds/svmod timeSide212

Figure 6 shows a snap shot at 0.5 s (at the same time as wavefields shown in Figure 4) of the difference. Again, the second-order approximation shows less differ-

ence, and thus, a better match than the first order approximation and definitely the unperturbed wavefield. In fact, in the unperturbed wavefield a clear polarity reversal at the anomaly apex is evident.

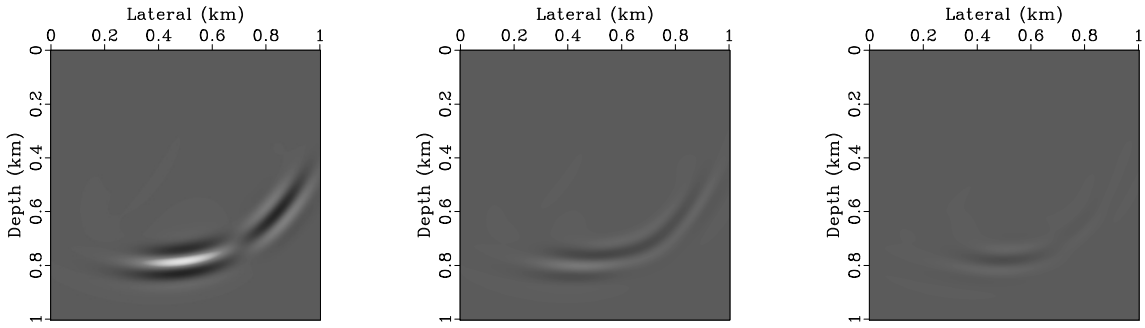

Figure 6: A snap shot at time 0.5 seconds of the difference between the 0.35 km source wavefield and the 0.3 km source wavefield after superposing the sources (left), the difference after using the first order perturbation on the 0.3 km source wavefield (middle), and after using the second-order perturbation on it (right). waveds/svmod timeSide220

Clearly, the perturbation formulas help reduce the difference between the actual wavefield and the perturbed one. An even closer look suggests that most of the difference is amplitude related.

The Marmousi model

The geometry of the Marmousi is based, somewhat, on a profile through the Cuanza basin Versteeg (1993). The target zone is a reservoir located at a depth of about 2500 m. The model contains many reflectors, steep dips, and strong velocity variations in both the lateral and the vertical directions (with a minimum velocity of 1500 m/s and a maximum of 5500 m/s). However, the Marmousi model includes complex discontinuities that pose problems to the perturbation formulation. As a result, we smooth the velocity model to obtain the model in Figure 7 (right). The point source considered here is a Ricker wavelet with a 15 Hz peak frequency.

Again using the fourth-order finite difference approximation in space and second order in time we solve the wave equation for a source located at the surface at lateral position 5 km, A snap shot of the resulting wavefield at time 1.2 s is shown in Figure 8 (left). Solving the wave equation for a source located 25 meters away results in the snap shot of the wavefield at 1.2 s shown in Figure 8 (middle). Superimposing the sources for the two fields and subtracting them yields the difference shown in Figure 8 (right). All three snap shots are plotted at the same scale (and this scale is maintained for all Figures in this section) and thus the difference, which is totally due to lateral inhomogeneity, is relatively large. It is especially large for the parts of the wavefront that were exposed to large lateral variations in the smoothed Marmousi model. This

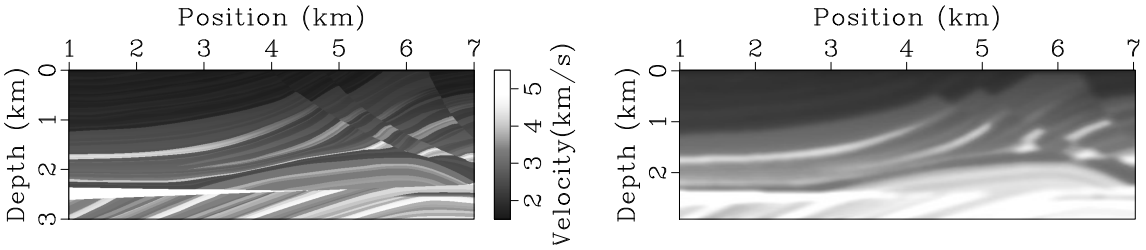

Figure 7: The Marmousi velocity model (left) and a smoothed version of it (right). waveds/fdmod medium

difference represents the wavefield we anticipate from the solution of new perturbation equation.

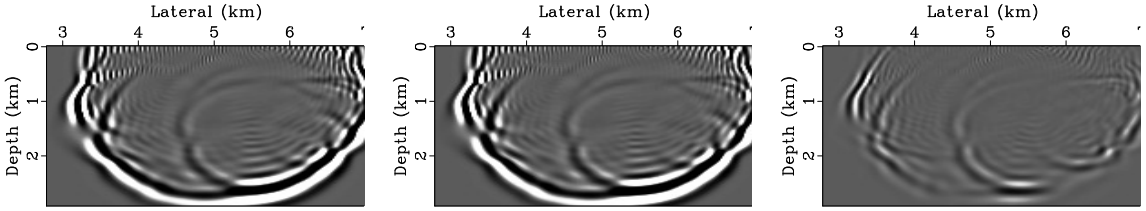

Figure 8: A snap shot of the wavefield obtained from solving the conventional wave equation in the smoothed Marmousi model for a source located at surface at 5 km (left) and at 5.025 km (middle). The difference between the two wavefields when we shift one of them to make the sources coincide is shown on the right. All three plots are displayed using the same range and this range is maintained in all Figures corresponding to Marmousi example. waveds/fdmod timeSide248

Using the new perturbation partial differential equations, I predict this difference from the original wavefield with source at location 5 km. We then add this difference to that original wavefield using equation (8), which provides an approximate to the wavefield for a source located at 5.025 km. Figure 9 shows a 1.2 s snap shot of the wavefield computed directly from a source at 5.025 km (left) and that obtained from the first-order perturbation expansion (middle), as well as, the difference between the two wavefields (right). Clearly, the difference is now less than that in Figure 8 in which perturbation was not used.

In fact, if we display the differences side by side along with that associated with the second-order perturbation approximation, Figure 10 demonstrates that the difference decreases considerably for the higher-order perturbation approximation, shown on the right.

One of the main objectives of solving the wave equation is to simulate the behavior of the wavefield at the surface (the measurement plane) as a function of time. Figure 11 shows the difference between the 5.025 km source and the 5 km source

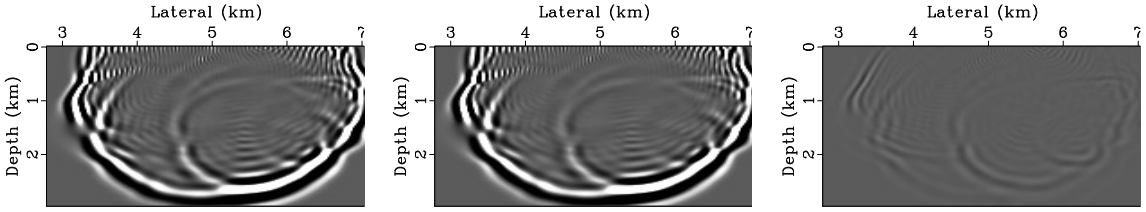

Figure 9: A snap shot of the wavefield obtained from solving the conventional wave equation in the smoothed Marmousi model for a source located at surface at 5.025 km (left), and the snap shot by perturbing the 5 km source wavefield to approximate the 5.025 km one using the first-order equation (middle). The difference between the two wavefields is shown on the right. waveds/fdmod timeSide348

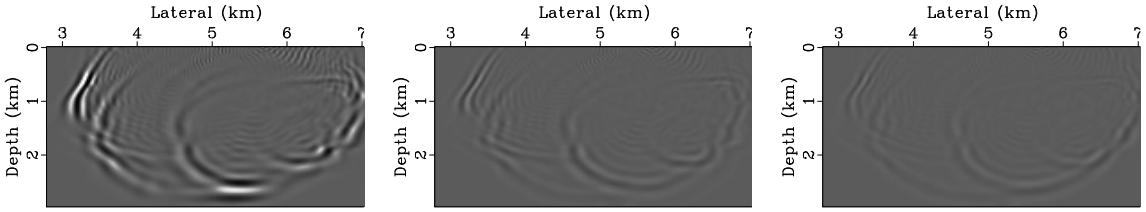

Figure 10: A snap shot of the difference between the 5 km source wavefield and the 5.025 km source wavefield (left), the difference after using the first order perturbation (middle), and after using the second-order perturbation (right). waveds/fdmod timeSide548

common-shot gathers after superimposing the sources (left) and compares it with difference between the 5.025 km source and first-order (middle) and the second order (right) perturbed versions. Clearly, the source gather extracted from using the perturbation equations better resemble the directly evaluated one than the source gather that does not include the perturbation. Specifically, most of the primary reflections in the section are seemingly well modeled by the perturbation approximation, as evidence by the small difference between the directly extracted gather and the perturbed one.

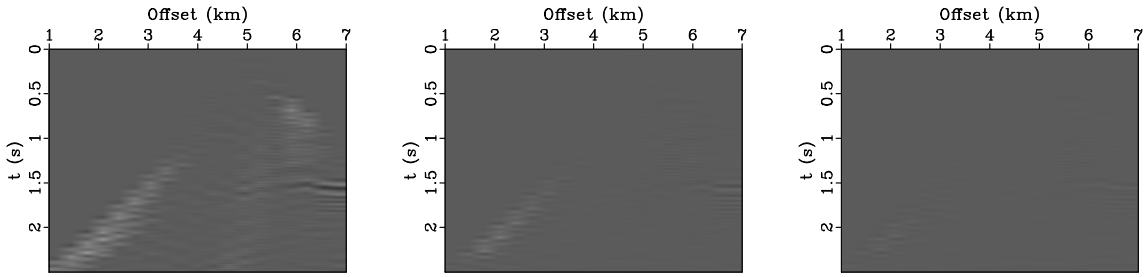

Figure 11: The difference between a shot gather for a source located at surface at 5.025 km and one located at 5 km after superimposing the sources (left), the difference between a shot gather for a source located at surface at 5.025 km and one extracted from the expansion of the 5 km source location using the first-order perturbation approximation (middle), and using the second-order perturbation approximation (right) for the smoothed Marmousi model. waveds/fdmod datdiffF

DISCUSSION

The transformation of the wavefield's shape as a function of source location provides valuable information for many applications, and in particular interpolation, velocity estimation, and imaging. All three applications rely in one way or another on the relation between the wavefields and the source location. To predict the content of a missing shot (or receiver) gather, we usually rely on reflection slope information of nearby common shot gathers [Fomel (2002)] to extend the information to the missing locations. For homogeneous and vertically inhomogeneous media, the process of interpolation is trivial as the common shot gathers are the same regardless of surface position. The complication occurs when the velocity varies laterally and differences, as we have seen above, can be large. Using these perturbation partial differential equations we can estimate the changes needed to fill in the gaps. This can be done as part of a finite-difference modeling or a reverse time migration process. It also can be done using a point source to generate the wavefield in a forward finite-difference approach or using a boundary condition, as typically the case for reverse time extrapolation of the receiver wavefields recored at the surface for the purpose of imaging. The equations shown above have no source restrictions and their development are not based on a particular source.

A major drawback of using conventional methods to solve the wave equation is that typically the velocity information and complexity have no baring on the efficiency of obtaining such solutions. In the development here, the perturbed wavefields are only excited by lateral velocity variation and in the absence of such variations we do not need to evaluate the perturbations. This allows us to implement selective computations that depends on the wavefield complexity and isolate areas of contribution based on the velocity field.

Nevertheless, the accuracy of the first and second order expansion approximations introduced here depends on the size of the source (or velocity) shift. Unlike, the traveltime version [Alkhalifah and Fomel (2009)] the wavefield is highly oscillatory (sinusoidal components)and thus their Taylor's series approximation accuracy is dependent on the wavelength of the perturbed wavefield within the context of the lateral velocity complexity. The accuracy here is synonymous to what we encounter using the Born approximation. However, unlike Born approximation, the source functions in equations (4) and (7) depend on the lateral velocity variation, not the source perturbation. Specifically, if the lateral velocity change induces perturbations in the wavefield that exceeds a half wavelength, we will encounter aliasing in the construction. This issue effects, more frequently, large dips and large perturbations with respect to the wavelength. However, unlike conventional source or velocity perturbation developments, this wavefield shape perturbation approach is far more stable and explicitly depends on the complexity of the lateral velocity variation as for the case of lateral homogeneity the approach is exact independent of amount of perturbation. Figure 12 shows a 1.2 second snap shot of the differences between the

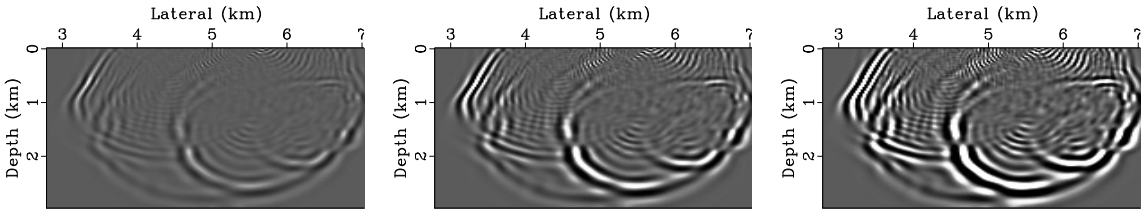

Figure 12: A snap shot of the difference between the 5 km source wavefield and the 5.05 km source wavefield (left), and the 5.075 km source wavefield (middle), and the 5.1 km source wavefield (right) after using the modified second-order expansion for 50, 75 and 100 meters perturbations, respectively. The velocity model is the original smoothed Marmousi model. waveds/fdmodnoSS timeSSSide6F48

wavefields obtained directly from a source and that obtained from nearby sources and perturbed a distance of 50 meters (left), 75 meters (middle), and 100 meters (right) for the smoothed Marmousi model using the second-order expansion. As expected the difference (error) is larger for the bigger perturbation. Also, we can observe that the dipping parts of the wavefield have larger errors as the effective change is bigger. Of course, we have to remind our selves that we are dealing with the Marmousi model, which is highly complex, and we can expect better results for smoother models. Also, we can observe that the difference is mainly manifested in the amplitude, where the

kinematics (phase) show little difference.

CONCLUSIONS

The transformation in the wavefield shape as a function of source location is directly related to the lateral velocity variation. Such transformation is described by partial differential equations that have forms similar to the conventional acoustic wave equation in which their solutions provide the coefficients needed for a Taylor's series type expansion. The source function, for the perturbation equation, depends on the background wavefield of the original source as well as lateral derivatives of the velocity of the medium. As a result, while the second order expansion, which requires solving two PDEs, provide the best approximation of the perturbation in generally smooth velocity models, as expected, and similar to the Born approximation, the accuracy of the approximation here reduces with the size of the source perturbation. However, unlike the Born approximation, the accuracy here depends only on the amount of lateral velocity variation, not on the velocity perturbation acting as a secondary source.

ACKNOWLEDGMENTS

I thank Sergey Fomel for many useful discussions. I thank KAUST for its support. I also thank the editors and the anonymous reviewers for their critical and helpful review of the paper.

REFERENCES

Aki, K., and P. G. Richards, 1980, Quantitative seismology: theory and methods: W.H. Freeman and Company, Volume I.

Alkhalifah, T., 1996, Transformation to zero offset in transversely isotropic media: Geophysics, **61**, 947–963.

———, 2005, Residual dip moveout in VtI media: Geophys. Prosp., **53**, 1–12.

Alkhalifah, T., and S. Fomel, 2009, An eikonal based formulation for traveltime perturbation with respect to the source location: Geophysics, accepted.

Alkhalifah, T. T., and B. Biondi, 2004, Numerical analysis of the azimuth moveout operator for vertically inhomogeneous media: Geophysics, **69**, 554–561.

Bagaini, C., and U. Spagnolini, 1993, Common shot velocity analysis by shot continuation operator: 63rd Ann. Internat. Mtg, Soc. of Expl. Geophys., 673–676.

———, 1996, 2-D continuation operators and their applications: Geophysics, **61**, 1846–1858.

Biondi, B., S. Fomel, and N. Chemingui, 1998, Azimuth moveout for 3-D prestack imaging: Geophysics, **63**, 574–588.

Bolondi, G., E. Loinger, and F. Rocca, 1982, Offset continuation of seismic sections: Geophys. Prosp., **30**, 813–828.

Cohen, J., and N. Bleistein, 1977, Seismic waveform modelling in a 3-d earth using the born approximation: potential shortcomings and a remedy: J. Appl. Math, **32**, 784–799.

Courant, R., K. Friedrichs, and H. Lewy, 1928, Uber die partiellen differenzengleichungen der mathematischen physik: Math. Ann., **100**, 32–74.

Fomel, S., 2002, Applications of plane-wave destruction filters: Geophysics, **67**, 1946–1960.

Hale, D., 1991, Course notes: Dip moveout processing: Soc. Expl. Geophys.

Panning, M., Y. Capdeville, and A. Romanowicz, 2009, An inverse method for determining small variations in propagation speed: Geophys. J. Int., **177**, 161–178.

Versteeg, R. J., 1993, Sensitivity of prestack depth migration to the velocity model: Geophysics, **58**, 873–882.

An eikonal based formulation for traveltime perturbation with respect to the source location

Tariq Alkhalifah and Sergey Fomel[1]

ABSTRACT

Traveltime calculations amount to solving the nonlinear eikonal equation for a given source location. We analyze the relationship between the eikonal solution and its perturbations with respect to the source location and develop a partial differential equation that relates the traveltime field for one source location to that for a nearby source. This linear first-order equation in one form depends on lateral changes in velocity and in another form is independent of the velocity field and relies on second-order derivatives of the original traveltime field. For stable finite-difference calculations, this requires the velocity field to be smooth in a sense similar to ray-tracing requirements. Our formulation for traveltime perturbation formulation has several potential applications, such that fast traveltime calculation by source-location perturbation, velocity-independent interpolation including datuming, and velocity estimation. Additionally, higher-order expansions provide parameters necessary for Gaussian-beam computations.

INTRODUCTION

The traveltime field is typically used to describe the phase behavior of the Green's function, a key tool for Kirchhoff modeling and migration. It also is used at the heart of many velocity estimation applications, such as reflection tomography. The traveltime field for a fixed source in a heterogeneous medium is governed by the eikonal equation, derived about 150 years ago by Sir William Rowan Hamilton. Since early 1990s, a direct numerical solution of the eikonal equation has been a popular method of computing traveltimes on regular grids, commonly used in seismic imaging (Vidale, 1988, 1990; van Trier and Symes, 1991; Podvin and Lecomte, 1991). Modern methods of traveltime computation include the *fast marching* method, developed by Sethian (1996) in the general context of level set methods for propagating interfaces. Sethian and Popovici (1999) and Popovici and Sethian (2002) report a successful application of this method in three-dimensional seismic computations. Alkhalifah and Fomel (2001) improved its accuracy using spherical coordinates. Alternative methods include group fast marching (Kim, 2002), fast sweeping (Zhao, 2005), and paraxial marching (Qian and Symes, 2002). Several alternative schemes are reviewed by Kim (2002).

[1]**e-mail:** tkhalfah@kacst.edu.sa, sergey@sep.stanford.edu

The nonlinear nature of the eikonal partial differential equation was addressed by Aldridge (1994), who linearized the eikonal equation with respect to velocity perturbation, while retaining its first-order nature. Alkhalifah (2002) developed a similar linearization formula for perturbations in anisotropic parameters and solved it numerically using the fast marching method. The linear feature increased the efficiency and stability of the numerical solution, especially in the anisotropic case.

A major drawback of using conventional methods to solve the eikonal equation numerically is that we only evaluate the fastest arrival solution, not necessarily the most energetic one. This results in less than acceptable traveltime computation for imaging in complex media (Geoltrain and Brac, 1993). Eikonal solvers can be extended to image multiple arrivals through semi-recursive Kirchhoff migration (Bevc, 1997), phase-space equations (Fomel and Sethian, 2002), or slowness matching (Symes and Qian, 2003) techniques. The linearization also helps to avoid the first-arrival only limitation, especially when the background traveltime field includes energetic arrivals.

The dependence of the traveltime field on the source location can be empirically evaluated by comparing the shape of the traveltime fields for two different sources when the sources are superimposed on each other. For a medium with no lateral velocity variation, the traveltime field should be source-location independent. Relating the two traveltime fields directly through an equation can provide insights into the dependence of traveltime fields on lateral velocity variations. Such information can serve in developing better traveltime interpolation and velocity estimation.

In this paper, we develop a new eikonal-based partial differential equation that relates traveltime shape changes to changes in the source location. The changes can be described first- or second-order accurate terms and thus used in a Taylor's type expansion to find the traveltime for a nearby source. We test the accuracy of the approximation analytically and numerically through the use of complex synthetic models. In the discussion section, we suggest possible applications for the new equation.

SHIFT IN THE SOURCE LOCATION

The eikonal equation appears in the zeroth-order asymptotic expansion of the solution of the wave equation given by the Wentzel, Kramers, and Brillouin (WKB) approximation. It represents the geometrical optics term that contains the most rapidly varying component of the leading behavior of the expansion. In a medium with sloth (slowness squared), w, the traveltime τ for a wavefield emanating from a source satisfies the following formula:

$$\left(\frac{\partial \tau}{\partial x}\right)^2 + \left(\frac{\partial \tau}{\partial y}\right)^2 + \left(\frac{\partial \tau}{\partial z}\right)^2 = w(x,y,z), \tag{1}$$

where (x,y,z) are the components of the 3-D medium. At the location of the source (x_s,y_s,z_s), the initial value of time $\tau(x_s,y_s,z_s)=0$ is needed for numerically solving

the eikonal equation 1. Moving the source along the x-axis a distance l is equivalent to solving the following eikonal equation:

$$\left(\frac{\partial \tau}{\partial x}\right)^2 + \left(\frac{\partial \tau}{\partial y}\right)^2 + \left(\frac{\partial \tau}{\partial z}\right)^2 = w(x-l, y, z), \tag{2}$$

for the same source location. In other words, we are replacing a shift in the source location with an equal distance shift in the velocity field in the opposite direction. Figure 1 shows the operation for a single source and image point combination taking into account the reciprocity principle between sources and receivers.

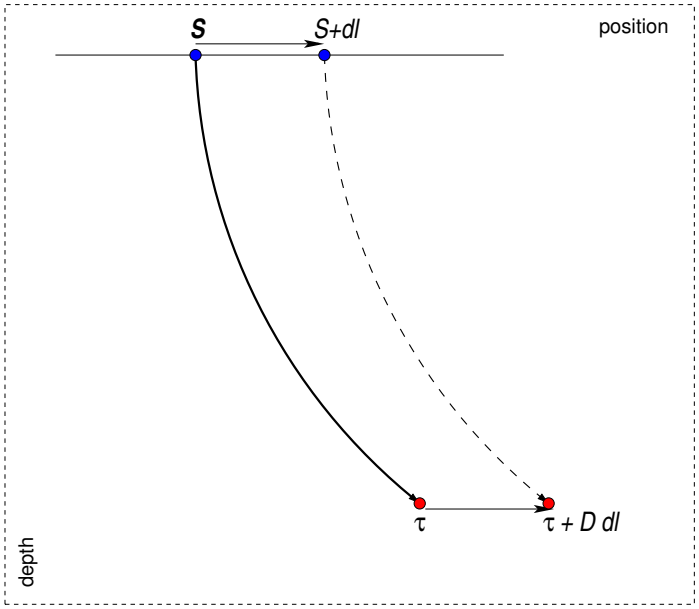

Figure 1: Illustration of the relation between the initial source location and a perturbed version given by a single source and image point locations. This is equivalent to a shift in the velocity field laterally by dl. eikds/XFig timeds

Assuming that the sloth (or velocity) field is continuous in the x direction, we differentiate equation 2 with respect to l and get:

$$2\frac{\partial \tau}{\partial x}\frac{\partial^2 \tau}{\partial x \partial l} + 2\frac{\partial \tau}{\partial y}\frac{\partial^2 \tau}{\partial y \partial l} + 2\frac{\partial \tau}{\partial z}\frac{\partial^2 \tau}{\partial z \partial l} = -\frac{\partial w}{\partial x}. \tag{3}$$

Substituting the change in traveltime field shape due to source perturbation, $D_x = \frac{\partial \tau}{\partial l}$, into equation 3 provides a first order linear equation in D_x given by:

$$2\frac{\partial \tau}{\partial x}\frac{\partial D_x}{\partial x} + 2\frac{\partial \tau}{\partial y}\frac{\partial D_x}{\partial y} + 2\frac{\partial \tau}{\partial z}\frac{\partial D_x}{\partial z} = -\frac{\partial w}{\partial x}. \tag{4}$$

Solving for D_x requires the velocity (sloth) field as well as the traveltime field τ for a source located at the surface at l_0. Thus,the traveltime field for a source at l can be approximated by

$$t(x, y, z) \approx \tau(x, y, z) + D_x(x, y, z)(l - l_0). \tag{5}$$

Equation 4 is velocity dependent, which limits its use for inversion purposes. However, a differentiation of Equation 2 with respect to x produces

$$2\frac{\partial \tau}{\partial x}\frac{\partial^2 \tau}{\partial x^2} + 2\frac{\partial \tau}{\partial y}\frac{\partial^2 \tau}{\partial x \partial y} + 2\frac{\partial \tau}{\partial z}\frac{\partial^2 \tau}{\partial x \partial z} = \frac{\partial w}{\partial x}. \tag{6}$$

Adding equations 3 and 6 yields equation

$$\frac{\partial \tau}{\partial x}\frac{\partial^2 \tau}{\partial x \partial l}+\frac{\partial \tau}{\partial y}\frac{\partial^2 \tau}{\partial y \partial l}+\frac{\partial \tau}{\partial z}\frac{\partial^2 \tau}{\partial z \partial l}=\frac{\partial \tau}{\partial x}\frac{\partial^2 \tau}{\partial x^2}+\frac{\partial \tau}{\partial y}\frac{\partial^2 \tau}{\partial x \partial y}+\frac{\partial \tau}{\partial z}\frac{\partial^2 \tau}{\partial x \partial z}, \tag{7}$$

which is velocity independent. Substituting again the change in traveltime with source location $D_x = \frac{\partial \tau}{\partial l}$ into equation 7 yields

$$\frac{\partial \tau}{\partial x}\frac{\partial D_x}{\partial x}+\frac{\partial \tau}{\partial y}\frac{\partial D_x}{\partial y}+\frac{\partial \tau}{\partial z}\frac{\partial D_x}{\partial z}=\frac{\partial \tau}{\partial x}\frac{\partial^2 \tau}{\partial x^2}+\frac{\partial \tau}{\partial y}\frac{\partial^2 \tau}{\partial x \partial y}+\frac{\partial \tau}{\partial z}\frac{\partial^2 \tau}{\partial x \partial z}, \tag{8}$$

which is a first order linear partial differential equation in D_x with D_x=0 at the source. The traveltime derivatives are computed for a given traveltime field τ corresponding to a source location l_0. Equation 8 can be represented in a vector notation as follows:

$$\nabla \tau \cdot \nabla D_x \;=\; \nabla \tau \cdot \nabla \frac{\partial \tau}{\partial x}. \tag{9}$$

A similar treatment for a change of the source location in y or z yields the following equations, respectively:

$$\frac{\partial \tau}{\partial x}\frac{\partial D_y}{\partial x}+\frac{\partial \tau}{\partial y}\frac{\partial D_y}{\partial y}+\frac{\partial \tau}{\partial z}\frac{\partial D_y}{\partial z}=\frac{\partial \tau}{\partial x}\frac{\partial^2 \tau}{\partial x \partial y}+\frac{\partial \tau}{\partial y}\frac{\partial^2 \tau}{\partial y^2}+\frac{\partial \tau}{\partial z}\frac{\partial^2 \tau}{\partial y \partial z}, \tag{10}$$

or

$$\nabla \tau \cdot \nabla D_y \;=\; \nabla \tau \cdot \nabla \frac{\partial \tau}{\partial y}. \tag{11}$$

and

$$\frac{\partial \tau}{\partial x}\frac{\partial D_z}{\partial x}+\frac{\partial \tau}{\partial y}\frac{\partial D_z}{\partial y}+\frac{\partial \tau}{\partial z}\frac{\partial D_z}{\partial z}=\frac{\partial \tau}{\partial x}\frac{\partial^2 \tau}{\partial x \partial z}+\frac{\partial \tau}{\partial y}\frac{\partial^2 \tau}{\partial y \partial z}+\frac{\partial \tau}{\partial z}\frac{\partial^2 \tau}{\partial z^2}, \tag{12}$$

or

$$\nabla \tau \cdot \nabla D_z \;=\; \nabla \tau \cdot \nabla \frac{\partial \tau}{\partial z}. \tag{13}$$

The above set of equations provides a tool for calculating first-order traveltime derivatives with respect to the source location. However, a condition for stability is that the velocity field must be continuous. This condition is analogous to conditions used in ray tracing methods and can be enforced using smoothing techniques. Another approach to handle this limitation is discussed later.

A LINEAR VELOCITY MODEL EXAMPLE

As a first test to our formulations, we consider a 2-D model where the velocity changes linearly in the direction of the source perturbation. In this case, the traveltime is described analytically as a function of x and z and so will the traveltime changes, D_x. Restricting this example to models with change of velocity in the direction of the source perturbation does not limit its generality since changes in the orthogonal direction has no direct influence on the traveltime field.

In the first example, we consider a source perturbation in the vertical direction in a medium in which the velocity changes linearly in the vertical direction. Considering source perturbation in the vertical direction is useful for applications related to datuming and possibly downward continuation. The linear velocity model is defined by

$$v(z) = v_0 + az. \tag{14}$$

where a is the vertical velocity gradient and v_0 is velocity at the surface $z = 0$. The traveltime from a source at $x = z = 0$ to a point in the subsurface given by x and z is provided by Slotnick (1959), as follows:

$$\tau(x,z) = \frac{1}{a}\cosh^{-1}\left(\frac{a^2z^2\left(\frac{x^2}{z^2}+1\right)}{2v_0\left(az+v_0\right)}+1\right). \tag{15}$$

Evaluating $\frac{\partial\tau}{\partial x}$ and $\frac{\partial\tau}{\partial y}$ and using equation 4 yields:

$$D_z = -\frac{\left(az+2v_0\right)\sqrt{\frac{a^2(x^2+z^2)}{a^2x^2+(az+2v_0)^2}}}{v_0\left(az+v_0\right)}, \tag{16}$$

which is an analytical representation of the change in the traveltime field shape with source depth location for this specific linear model and can be used to predict the traveltime for a source at a different depth. To test equation 16, we use equation 15 to estimate the traveltime using expansion 5 and compare that with the true traveltime for that source. Figure 2 shows this difference for a model with (a) a vertical velocity gradient of 0.5 s^{-1} and (b) a vertical velocity gradient of 0.7 s^{-1}. A 200 meter vertical shift, used here for the source, is typical of corrections applied in datuming among other applications. The errors, as expected, increase with an increase in velocity gradient as zero velocity gradient results in no change in traveltime shape and thus no errors. However, the errors are generally small for both gradients with the maximum value of 0.007 s occurring for the largest offset to depth ratio.

In the second example, we consider source perturbation laterally in a medium in which the velocity changes linearly in the lateral direction. Considering source perturbation in the lateral direction could be useful for velocity estimation, beam based imaging, and interpolation applications, and more inline with the objectives of this study. In this case, the linear velocity model is defined by

$$v(x) = v_0 + ax. \tag{17}$$

where a is now the lateral velocity gradient and v_0 is velocity at the vertical line $x = 0$. The traveltime and D_x are given by formulations similar to equations 15 and 16, but with an orthogonal transformation of coordinates. Though the equations are similar, we want to get an estimate of the error distribution for this problem. Figure 3 shows the traveltime errors for using these new formula to predict the changes due to shifts in the source location by (a) 100 meters and (b) 200 meters. As expected, the errors increase with the amount of shift. However, in both cases the errors are generally small and bounded by 0.002 s.

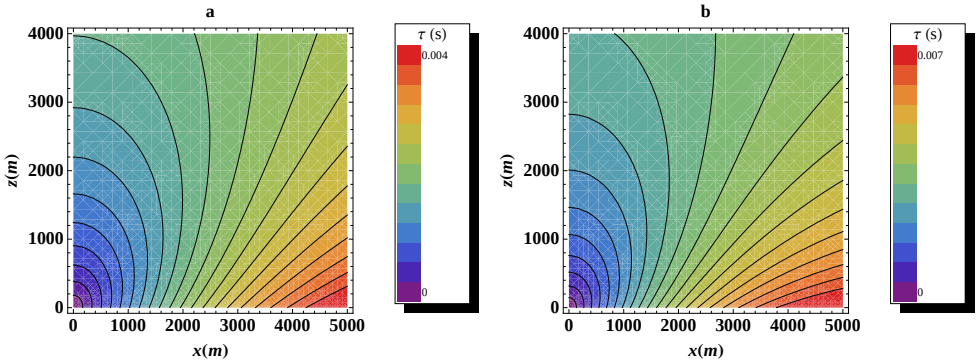

Figure 2: A color contour plot of the traveltime errors using the perturbation equation as a function of location (x, z) for a linear velocity model of with v_0=2000 m/s and a vertical velocity gradient of $0.5s^{-1}$ for (a) and $0.7s^{-1}$ for (b). In both cases, the vertical source perturbation distance is 200 meters. The maximum traveltime errors are (a) 0.004 s and (b) 0.007 s. eikds/Math diff2

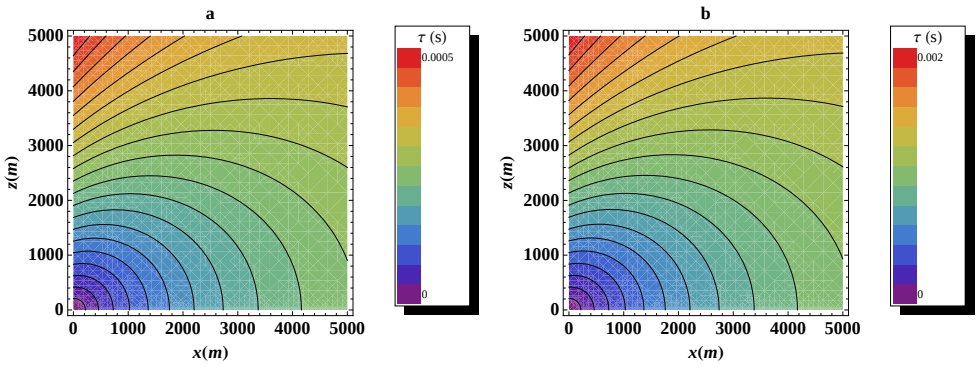

Figure 3: A color contour plot of the traveltime errors using the perturbation equation as a function of location (x, z) for a linear velocity model of with v_0=2000 m/s and a horizontal velocity gradient of $0.5s^{-1}$ for (a) a horizontal source perturbation of 100 meters and (b) a horizontal source perturbation distance of 200 meters. The maximum traveltime errors are (a) 0.0005 s and (b) 0.002 s. eikds/Math diffx2

HIGHER-ORDER ACCURACY

The accuracy of the above formulations are first order in source perturbation, which is valid for small perturbation distances. To obtain a higher-order accuracy, we differentiate equation 3 again with respect to l yielding:

$$2\left(\frac{\partial^2\tau}{\partial x\partial l}\right)^2+2\frac{\partial\tau}{\partial x}\frac{\partial^3\tau}{\partial x\partial l^2}+2\left(\frac{\partial^2\tau}{\partial y\partial l}\right)^2+2\frac{\partial\tau}{\partial y}\frac{\partial^3\tau}{\partial y\partial l^2}+2\left(\frac{\partial^2\tau}{\partial z\partial l}\right)^2+2\frac{\partial\tau}{\partial z}\frac{\partial^3\tau}{\partial z\partial l^2}=\frac{\partial^2 w}{\partial x^2}. \tag{18}$$

Substituting the second derivative of traveltime with respect to source location $D_{xx}=\frac{\partial^2\tau}{\partial l^2}$ into equation 18 provides us with a first order linear partial differential equation in D_{xx} given by:

$$2\left(\frac{\partial D_x}{\partial x}\right)^2+2\frac{\partial\tau}{\partial x}\frac{\partial D_{xx}}{\partial x}+2\left(\frac{\partial D_x}{\partial y}\right)^2+2\frac{\partial\tau}{\partial y}\frac{\partial D_{xx}}{\partial y}+2\left(\frac{\partial D_x}{\partial z}\right)^2+2\frac{\partial\tau}{\partial z}\frac{\partial D_{xx}}{\partial z}=\frac{\partial^2 w}{\partial x^2}, \tag{19}$$

or

$$\nabla D_x\cdot\nabla D_x+\nabla\tau\cdot\nabla D_{xx}=\frac{1}{2}\frac{\partial^2 w}{\partial x^2} \tag{20}$$

This equation is similar in form to the first order equations, but with a different source function. Of course, D_x must be evaluated first using equation 4 to solve equation 20.

Based on Taylor's series expansion, the traveltime for a source at l is approximated by

$$t(x,y,z)\approx\tau(x,y,z)+D_x(x,y,z)(l-l_0)+\frac{1}{2}D_{xx}(x,y,z)(l-l_0)^2. \tag{21}$$

Using an infinite series representation by defining poles to eliminate the most pronounced transient behavior using Shanks transforms (Bender and Orszag, 1978), we can represent the second order Taylor's expansion in equation 21 as follows

$$t(x,y,z)\approx\tau(x,y,z)+\frac{{D_x}^2(x,y,z)(l-l_0)}{D_x(x,y,z)(l-l_0)+\frac{1}{2}D_{xx}(x,y,z)(l-l_0)^2}, \tag{22}$$

which can provide a better approximation results in some regions but has an obvious singularity that might cause divergence when the denominator tends to zero.

Similar equations for expansions in 3-D are obtained with the help of the following matrix

$$\begin{pmatrix} D_{xx} & D_{xy} & D_{xz}\\ D_{xy} & D_{yy} & D_{yz}\\ D_{xz} & D_{yz} & D_{zz}\end{pmatrix}=\begin{pmatrix} \frac{\partial^2\tau}{\partial l_x^2} & \frac{\partial^2\tau}{\partial l_x l_y} & \frac{\partial^2\tau}{\partial l_x l_z}\\ \frac{\partial^2\tau}{\partial l_x l_y} & \frac{\partial^2\tau}{\partial l_y^2} & \frac{\partial^2\tau}{\partial l_y l_z}\\ \frac{\partial^2\tau}{\partial l_x l_z} & \frac{\partial^2\tau}{\partial l_y l_z} & \frac{\partial^2\tau}{\partial l_z^2}\end{pmatrix}, \tag{23}$$

with components obtainable using similar first order partial differential equations shown in Appendix A, where l_x, l_y, and l_z describe source perturbations in the x, y, and z directions, respectively. These equations can form the basis for beam expansions in beam-type migrations.

The higher-order equations provide better approximations of the traveltime perturbation. However, they require both the velocity and its derivative to be continuous in the direction of the source perturbation.

ALGORITHM

All the traveltime source perturbation equations developed above are linear first order partial differential equations that can be solved using any of the many upwind numerical methods. Similar to Franklin and Harris (2001) and Alkhalifah (2002), we will rely on the fast marching method Sethian (1996) to solve such linear equations.

An update procedure for such a method is based on an upwind first or second-order approximation to the new equations. In simple terms, the procedure starts with selecting one or more (up to three) neighboring points around the updated point. The traveltime values at the selected neighboring points need to be smaller than the current value. After the selection, one solves the discrete version of the linear partial differential equation for D_x. We add this perturbation value multiplied by the perturbation distance to the background traveltime. As the result of the updating, either a FarAway point is marked as NarrowBand or a NarrowBand point gets assigned a new value. This process is repeated until we run out of points in the narrow band.

In all cases, we will need the traveltime field for a given source obtained using the eikonal equation or ray-based methods. This traveltime field serves as the background field for predicting the traveltime for other sources. For the first-order accuracy expansion, we have to only solve the linear source differential eikonal partial differential equation once. However, for the second order expansion or its shank transform representation, we will need D_{xx}, and thus need to solve an equivalent linear differential equation again.

The critical part of solving these equations is the need to evaluate the first and second order derivatives of the velocity field or equivalently the second- and third-order derivatives of the background traveltime field all with respect to the direction in which the source is perturbed. This poses a challenge in media where the velocity changes abruptly in that direction. Therefore, some smoothing may be required for the velocity field in the source perturbation direction.

EXAMPLES

Lens example

Since the differential equation depends on velocity changes in the direction of the source shift, we test the methodology on a model that contains a lens anomaly in an otherwise constant velocity gradient ($\frac{dv}{dx} = 0.5s^{-1}$ and $\frac{dv}{dz} = 0.7s^{-1}$ with velocity at

the origin equal to 2 km/s) model. The lens is located at 600 meters laterally and 500 meters depth with a velocity perturbation of +500 m/s (or 20%). The lens has a diameter of 200 meters and causes a large velocity variation. Using this model, we test the accuracy of the first-order, second-order, and the Shanks-transform representation equations.

For a source located at 200 meters lateral distance from origin and 200 meter depth, we solve the eikonal equation using the fast marching method with second order accuracy. The traveltime field in this case is represented by the solid contours on the left side plots of Figures 4, 5, and 6. We also solve the eikonal equation for source located virtually 100 meters away in lateral direction and it is represented by the solid curves in the middle plot of the three Figures. Solving for D_x using equation 3 and using that along with the original traveltime field, we obtain an approximate traveltime field for a source 100 meters away. This new traveltime field is represented by the dashed contour curves in Figure 4. The absolute difference between the simulated traveltime and the true one both displayed in the center plot is given by the density plot shown on the right side of Figure 4.

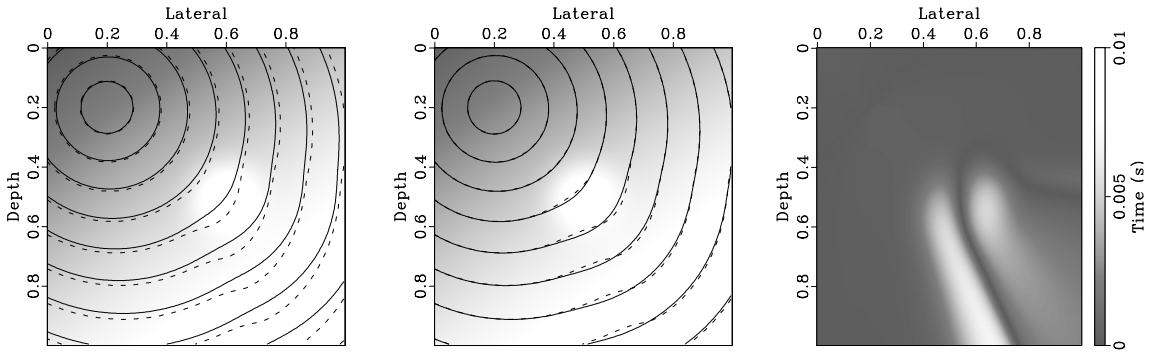

Figure 4: The traveltime contour (solid curve) plot for a source at lateral and depth position of 0.2 km (left) and for a source virtually perturbed by 100 meters in the lateral direction (middle), both compared with the traveltime derived using the first-order accuracy perturbation eikonal for a 100 meters virtual shift (dashed curves). In both plots the velocity field is shown in the background. Also shown on the right is a density plot of the difference between the two contours in the middle plot. eikds/smvel circ1

The errors are generally small (less than 0.008 s), with the largest of errors appearing on the lower side of the lens. This error is generally small considering the large shift (100 meters) and first-order nature of the expansion. In addition, errors for the rest of the traveltime field corresponding to the linear variation in velocity is extremely small.

Figure 5 is similar to Figure 4, but now we use the second-order expansion, which requires solving the linear partial differential equation twice. Overall, as expected, the errors are less than the first order case with clear reduction in the upper side trail of the lens.

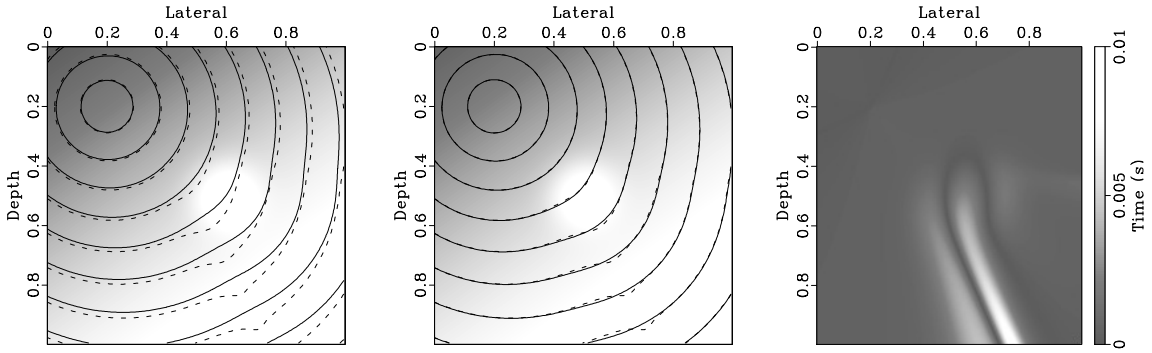

Figure 5: The traveltime contour (solid curve) plot for the original source (left) and for a source virtually perturbed by 100 meters in the lateral (middle), both compared with the traveltime derived using the second-order accuracy perturbation eikonal for a 100 meters virtual shift (dashed curves). In both plots the velocity field is shown in the background. Also shown on the right is a density plot of the difference between the two contours in the middle plot. eikds/smvel circ2

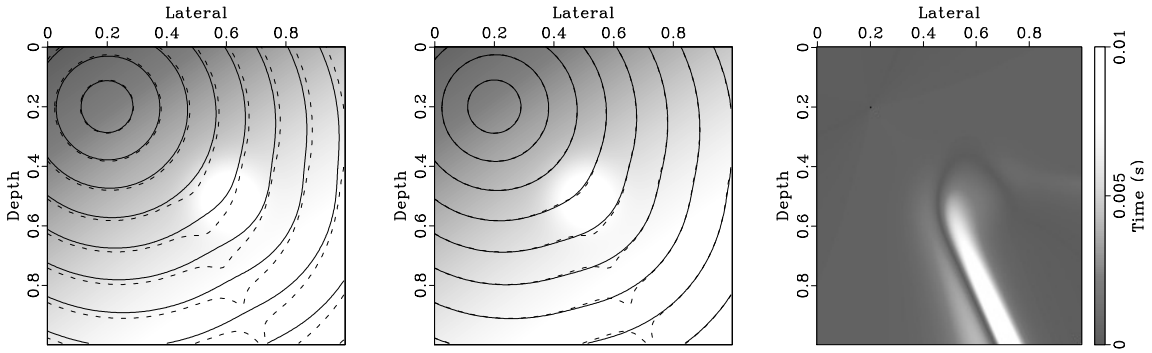

Figure 6: The traveltime contour (solid curve) plot for the original source (left) and for a source virtually perturbed by 100 meters (middle), both compared with the traveltime derived using Shanks transform perturbation eikonal for a 100 meters virtual shift (dashed curves). In both plots the velocity field is shown in the background. Also shown on the right is a density plot of the difference between the two contours in the middle plot. eikds/smvel circ3

With hardly any additional computational cost, we can use the Shank transform representation of the expansion and in this case the errors, as shown in Figure 6, are reduced even further.

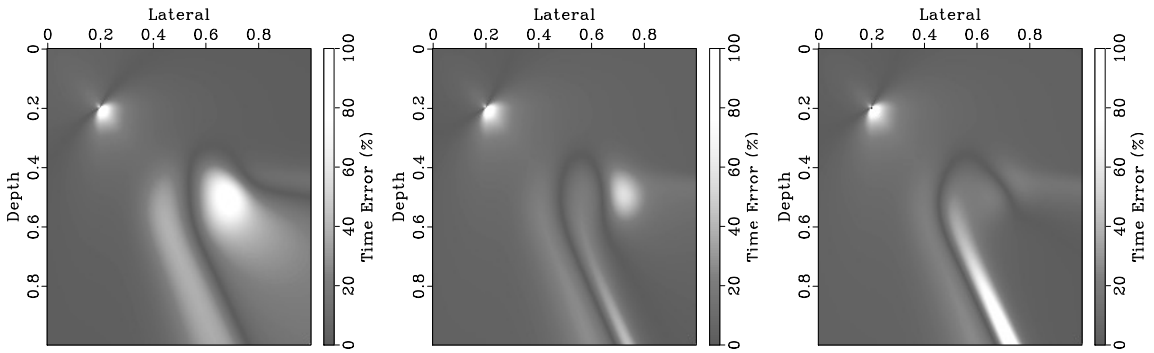

Figure 7: A density plot of the traveltime error in percent for the difference plots in Figures 4-6 (right), plotted from left to right, respectively. The percent error is measured in a relative manner where 0 corresponds to the accurate traveltime and 100% to the unperturbed traveltime. eikds/smvel circ4

To emphasize the role of the perturbation terms in approximating the source-shifted traveltime, we define a relative percent error as

$$t_{err} = 100\frac{\tau - \tau_0}{\tau_1 - \tau_0}, \tag{24}$$

where τ_0 is the unperturbed traveltime for the original source, τ_1 is the traveltime for the desired source calculated directly using the conventional eikonal equation, and τ is the traveltime estimated using the perturbation equations for the desired source. If τ is equal to τ_1, as desired, the error is zero. However, if τ equals the unperturbed traveltime τ_0 the error is 100 percent. Figure 7 shows this relative errors for the first-order accuracy perturbation (left), the second-order accuracy perturbation (middle), and using Shanks transform perturbation (right) for the linear model with a lens. The errors are overall less for the Shanks transform perturbation. The large error at position and depth equal to 0.2 km corresponds to the source location, where the denominator of equation 24 tends to zero.

Marmousi example

Despite the fact that the source perturbation differential equations are dependent on the derivative of velocity, and thus, discontinuous velocity fields pose a problem, we test the method on the unsmoothed Marmousi model (Versteeg, 1994) to asses the stability of the numerical process. In this case, we use only the first order expansion to avoid relying on higher order derivatives of the velocity field, which might breakdown here.

Figure 8 shows the Marmousi model in the background with the traveltime field contours computed directly using the finite difference eikonal equation for a source located at 4.2 km at the surface (dashed curves) compared with the traveltime field perturbed from a source located 200 meters away at 4 km surface location. The two contour curves overlap near the source, but show some difference away from the source. However, the difference is generally small considering the large source perturbation of 200 meters and the velocity complex model.

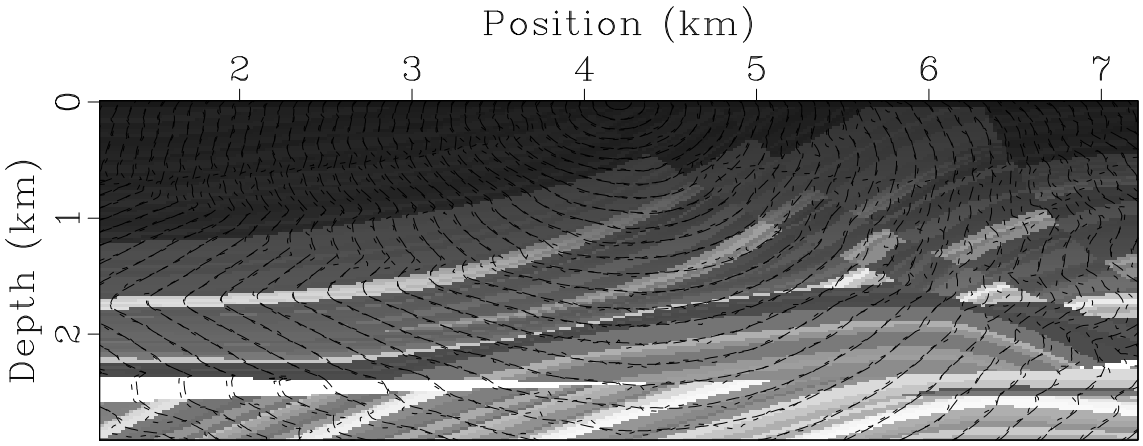

Figure 8: The traveltime contour plot for a source at the surface at 4.2 km (dashed curves) and for a source virtually perturbed by 200 meters from the traveltime field at 4 km source surface location (solid curves). The perturbed traveltime is derived using the first-order accuracy perturbation eikonal. The Marmousi velocity field is shown in the background. eikds/marm2 cir1

A closer and more quantitative look is given by the difference plot; Figure 9 shows a density plot for the difference in traveltime contours in Figure 8. With a clip of 0.01 seconds, errors given in gray are small and dominate the plot. This is a testament to the stability of the Fast marching implementation despite the complex velocity field that includes many lateral discontinuities.

DISCUSSION

Seismic data are usually acquired with geophone layouts that record information from multiple source locations. The redundancy in the coverage is necessary to eliminate gaps in the data, estimate velocity, and image the data. Thus, the direct relation between the traveltime field and the source location allows us to estimate attributes that can help in interpolation, velocity estimation and possibly imaging. Specifically:

- Traveltime compression schemes (Alkhalifah, 2010) require the ability to interpolate subsampled traveltimes.

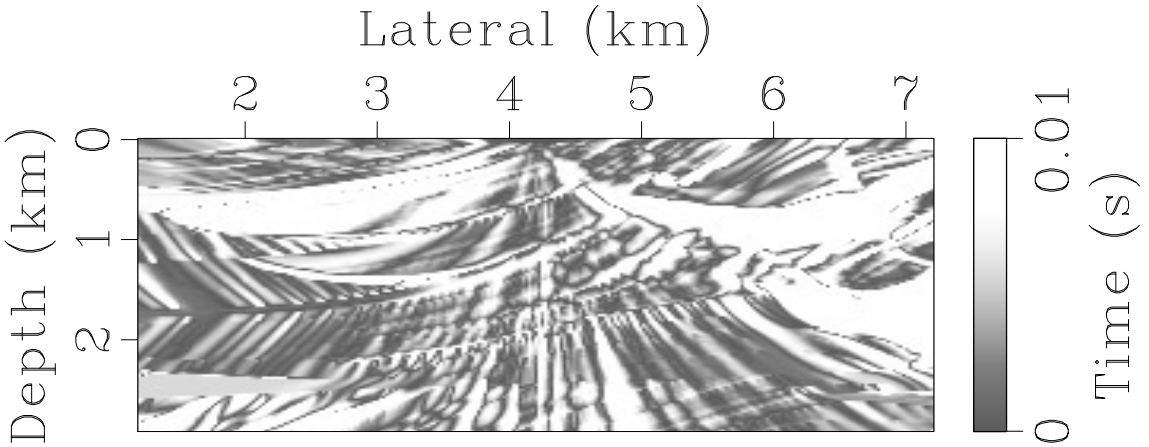

Figure 9: A density plot for the difference between the two contours shown in Figure 8.
eikds/marm2 cir2

- One of the main sources of trace interpolation information is the behavior of wavefronts with respect to the source location.

- Velocity estimation relies directly on the change in traces as a function of source and receiver locations.

- Kirchhoff antialiasing schemes (Lumley et al., 1994; Abma et al., 1999) explicitly require the derivatives of the traveltime with respect to the source and receiver locations on the surface.

- Gaussian-beam migration (Hill, 1990, 2001; Alkhalifah, 1995; Gray, 2005) relies on traveltime derivative information as a function of ray angle variations and source variations, which is usually obtained from the slower and less stable dynamic ray tracing.

- Efficient traveltime calculation can be achieved using first order linear equations instead of the nonlinear form of the eikonal equation.

However, the formulation developed here has limitations. Chief among them is the need to evaluate derivatives of velocity and traveltime fields. Since velocities may include discontinuities, their derivatives are not easy to evaluate. However, similar to the ray-based methods, one can simply smooth the velocity field.

Since traveltime fields that contain all arrivals satisfy the eikonal equation, the source perturbation can be applied to traveltimes extracted from other methods, such as ray tracing or escape equations. Therefore, they can include most energetic arrivals as opposed to first-arrival traveltimes.

CONCLUSIONS

The behavior of the traveltime field shape as a function of source location in an inhomogeneous medium provides a platform for many useful applications. We present eikonal-based equations that relate traveltime field changes with respect to the source perturbations. These equations are linear first-order differential equations that depend on the background traveltime and velocity fields. Their solutions describe the first- and second-order changes in the traveltime field as a function of the source location. These equations are equivalent to the plane wave expansion extracted from dynamic ray tracing, such as the one used for Gaussian-beam migration. They can be solved efficiently by finite-difference solvers on a regular grid. The solutions are used to estimate the traveltime shape for neighboring sources. The accuracy of the equations depends on the complexity of lateral velocity variations as well as on the source perturbation distance.

ACKNOWLEDGMENTS

The first author thanks KACST and KAUST for their support of this research. We thank the editors and the reviewers of Geophysics for their critical review of the paper and the resulting improvements.

REFERENCES

Abma, R., J. Sun, and N. Bernitsas, 1999, Antialiasing methods in Kirchhoff migration: Geophysics, **64**, 1783–1792.

Aldridge, D. F., 1994, Linearization of the eikonal equation (short note): Geophysics, **59**, 1631–1632.

Alkhalifah, T., 1995, Gaussian beam depth migration for anisotropic media: Geophysics, **60**, 1474–1484.

———, 2002, Traveltime computation with the linearized eikonal equation for anisotropic media: Geophys. Prosp., **50**, 373–382.

———, 2010, Efficient traveltime compression for 3D prestack kirchhoff migration: Geophysical Prospecting, in print, **58**.

Alkhalifah, T., and S. Fomel, 2001, Implementing the fast marching eikonal solver: spherical versus Cartesian coordinates: Geophys. Prosp., **49**, 165–178.

Bender, C. M., and S. A. Orszag, 1978, Advanced mathematical methods for scientists and engineers: McGraw-Hill.

Bevc, D., 1997, Imaging complex structures with semirecursive Kirchhoff migration: Geophysics, **62**, 577–588.

Fomel, S., and J. A. Sethian, 2002, Fast phase-space computation of multiple arrivals: Proceedings of the National Academy of Sciences, **99**, 7329–7334.

Franklin, J. B., and J. M. Harris, 2001, A high-order fast marching scheme for the linearized eikonal equation: Journal of Computational Acoustics, **9**, 1095–1109.

Geoltrain, S., and J. Brac, 1993, Can we image complex structures with first-arrival traveltime?: Geophysics, **58**, 564–575.

Gray, S. H., 2005, Gaussian beam migration of common-shot records: Geophysics, **70**, S71–S77.

Hill, N. R., 1990, Gaussian beam migration: Geophysics, **55**, 1416–1428.

———, 2001, Prestack Gaussian-beam depth migration: Geophysics, **66**, 1240–1250.

Kim, S., 2002, 3-D eikonal solvers: First-arrival traveltimes: Geophysics, **67**, 1225–1231.

Lumley, D. E., J. F. Claerbout, and D. Bevc, 1994, Anti-aliased Kirchhoff 3-D migration: 64th Ann. Internat. Mtg, Soc. of Expl. Geophys., 1282–1285.

Podvin, P., and I. Lecomte, 1991, Finite difference computation of traveltimes in very contrasted velocity models: A massively parallel approach and its associated tools: Geophysical Journal International, **105**, 271–284.

Popovici, A. M., and J. Sethian, 2002, 3-D imaging using higher order fast marching traveltimes: Geophysics, **67**, 604–609.

Qian, J., and W. W. Symes, 2002, An adaptive finite-difference method for traveltimes and amplitudes: Geophysics, **67**, 167–176.

Sethian, J. A., 1996, A fast marching level set method for monotonically advancing fronts: Proc. Nat. Acad. Sci., **93**, 1591–1595.

Sethian, J. A., and A. M. Popovici, 1999, 3-D traveltime computation using the fast marching method: Geophysics, **64**, 516–523.

Slotnick, M. M., 1959, Lessons in Seismic Computing: Soc. of Expl. Geophys. (Edited by R. A. Geyer).

Symes, W. W., and J. Qian, 2003, A slowness matching Eulerian method for multivalued solutions of eikonal equations: Journal of Scientific Computing, **19**, 501–526.

van Trier, J., and W. W. Symes, 1991, Upwind finite-difference calculation of traveltimes: Geophysics, **56**, 812–821.

Versteeg, R., 1994, The Marmousi experience: Velocity model determination on a synthetic complex data set: The Leading Edge, **13**, 927–936.

Vidale, J. E., 1988, Finite-difference calculation of traveltimes: Bull. Seis. Soc. Am., **6**, 20622076.

———, 1990, Finite-difference calculation of traveltimes in three dimensions: Geophysics, **55**, 521–526.

Zhao, H.-K., 2005, A fast sweeping method for eikonal equations: Mathematics of Computation, **74**, 603–627.

APPENDIX A: HIGHER-ORDER EXPANSIONS

Traveltime behavior due to source perturbations can be estimated more accurately using higher-order formulations. Considering that l_x, l_y, and l_z represent source perturbations in the x, y, and z directions, respectively, a full representation of the

second derivative behavior is given by the following symmetric matrix

$$\begin{pmatrix} D_{xx} & D_{xy} & D_{xz} \\ D_{xy} & D_{yy} & D_{yz} \\ D_{xz} & D_{yz} & D_{zz} \end{pmatrix} = \begin{pmatrix} \frac{\partial^2 \tau}{\partial l_x^2} & \frac{\partial^2 \tau}{\partial l_x l_y} & \frac{\partial^2 \tau}{\partial l_x l_z} \\ \frac{\partial^2 \tau}{\partial l_x l_y} & \frac{\partial^2 \tau}{\partial l_y^2} & \frac{\partial^2 \tau}{\partial l_y l_z} \\ \frac{\partial^2 \tau}{\partial l_x l_z} & \frac{\partial^2 \tau}{\partial l_y l_z} & \frac{\partial^2 \tau}{\partial l_z^2} \end{pmatrix}. \tag{E-1}$$

D_{xx} is evaluated using the first order linear differential equation 20, where τ is obtained from solving the eikonal equation and D_x is evaluated from equation 4.

Similarly, higher order approximations in l_y and l_z are given by

$$\nabla D_y \cdot \nabla D_y \, + \, \nabla \tau \cdot \nabla D_{yy} \, = \, \frac{1}{2} \frac{\partial^2 w}{\partial y^2} \tag{E-2}$$

and

$$\nabla D_z \cdot \nabla D_z \, + \, \nabla \tau \cdot \nabla D_{zz} \, = \, \frac{1}{2} \frac{\partial^2 w}{\partial z^2}, \tag{E-3}$$

respectively, which represent the diagonal terms of the matrix in equation E-1.

To obtain the non-diagonal components of the matrix we differentiate equation 3 with respect to l_y, instead of l_x, yielding:

$$2 \left(\frac{\partial^2 \tau}{\partial x \partial l_x} \right) \left(\frac{\partial^2 \tau}{\partial x \partial l_y} \right) + 2 \frac{\partial \tau}{\partial x} \frac{\partial^3 \tau}{\partial x \partial l_x \partial l_y} + 2 \left(\frac{\partial^2 \tau}{\partial y \partial l_x} \right) \left(\frac{\partial^2 \tau}{\partial y \partial l_y} \right) + 2 \frac{\partial \tau}{\partial y} \frac{\partial^3 \tau}{\partial y \partial l_x \partial l_y} + 2 \left(\frac{\partial^2 \tau}{\partial z \partial l_x} \right) \left(\frac{\partial^2 \tau}{\partial z \partial l_y} \right) + 2 \frac{\partial \tau}{\partial z} \frac{\partial^3 \tau}{\partial z \partial l_x \partial l_y} = \frac{\partial^2 w}{\partial x \partial y} \tag{E-4}$$

Substituting the second derivative of traveltime with respect to source location $D_{xy} = \frac{\partial^2 \tau}{\partial l_x \partial l_y}$ into equation E-4 provides us with a first order linear equation in D_{xy} given by:

$$2 \left(\frac{\partial D_x}{\partial x} \right) \left(\frac{\partial D_y}{\partial x} \right) + 2 \frac{\partial \tau}{\partial x} \frac{\partial D_{xy}}{\partial x} + 2 \left(\frac{\partial D_x}{\partial y} \right) \left(\frac{\partial D_y}{\partial y} \right) + 2 \frac{\partial \tau}{\partial y} \frac{\partial D_{xy}}{\partial y} + 2 \left(\frac{\partial D_x}{\partial z} \right) \left(\frac{\partial D_y}{\partial z} \right) + 2 \frac{\partial \tau}{\partial z} \frac{\partial D_{xy}}{\partial z} = \frac{\partial^2 w}{\partial x \partial y}. \tag{E-5}$$

or

$$\nabla D_x \cdot \nabla D_y \, + \, \nabla \tau \cdot \nabla D_{xy} \, = \, \frac{1}{2} \frac{\partial^2 w}{\partial x \partial y}. \tag{E-6}$$

Similar equations for the rest of the matrix components are given by

$$\nabla D_x \cdot \nabla D_z \, + \, \nabla \tau \cdot \nabla D_{xz} \, = \, \frac{1}{2} \frac{\partial^2 w}{\partial x \partial z}, \tag{E-7}$$

and

$$\nabla D_y \cdot \nabla D_z \, + \, \nabla \tau \cdot \nabla D_{yz} \, = \, \frac{1}{2} \frac{\partial^2 w}{\partial y \partial z}, \tag{E-8}$$

Wavefield extrapolation in pseudodepth domain

Xuxin Ma and Tariq Alkhalifah[1]

ABSTRACT

Wavefields are commonly computed in the Cartesian coordinate frame. Its efficiency is inherently limited due to spatial oversampling in deep layers, where the velocity is high and wavelengths are long. To alleviate this computational waste due to uneven wavelength sampling, we convert the vertical axis of the conventional domain from depth to vertical time or pseudo depth. This creates a nonorthognal Riemannian coordinate system. Both isotropic and anisotropic wavefields can be extrapolated in the new coordinate frame with improved efficiency and good consistency with Cartesian domain extrapolation results. Prestack depth migrations are also evaluated based on the wavefield extrapolation in the pseudodepth domain.

INTRODUCTION

Migrations based on wavefield extrapolation, both in depth and in time, are used extensively for imaging complex subsurface structures. Ray-based migrations such as Kirchhoff migration can not correctly image reflectors where multipathing occurs. In all the wave-equation based migrations, the seismic image is constructed directly from the wavefields by applying a proper imaging condition to the extrapolated wavefields. As a result, there is a constant demand of more accurate and more cost-effective means of wavefield extrapolation.

Wavefield extrapolation is commonly implemented by finite difference approximations using regularly spaced Cartesian meshes. It is popular because there is no need to interpolate wavefields between the computation domain and physical space. However, Cartesian coordinate frame is poor in several other aspects because it does not take into account the physics of the wavefield. For example, wavelength is varies in space due to velocity variation, and considering the regular spacing in conventional implementations, this could result in uneven spatial representation of wavefields. Specifically, we tend to undersample wavefields in layers with low velocities and oversample them in layers with high velocities. Another issue with the conventional Cartesian coordinate system arises with downward continuation in the presence of overturned events: the vertical extrapolation direction in a Cartesian mesh does not follow the direction of energy propagation.

[1]**e-mail:** tkhalfah@kacst.edu.sa, sergey@sep.stanford.edu

Wavefield extrapolation in non-Cartesian coordinate frames has been address by several authors for different purposes. Among them, the Riemannian coordinate allows downward continuation with small dip angles due to the fact that the coordinates are more aligned with wave-propagation directions (Sava and Fomel, 2005; Shragge, 2008); tilted Cartesian coordinate allows imaging of steep dipping reflectors using downward continuation (Shan and Biondi, 2008).

Our goal is to develop and implement reverse-time migration using pseudodepth in the vertical direction, as opposed to the conventional depth. The pseudo depth is velocity dependent in a way that the wavelength remains constant in spite of the vertical velocity variation. This allows the vertical axis to be discretized with less number of samples, and thus speed up imaging. In this paper, we first develop the pseudodepth coordinate frame and the procedures needed to interpolate between pseudodepth and the Cartesian coordinates. Next, we derive the proper extrapolation operators for isotropic and anisotropic media in the new coordinate frame. Finally, we present examples of pseudodepth domain prestack depth migration and compare the cost and accuracy with Cartesian domain implementation.

PSEUDODEPTH DOMAIN WAVE EQUATION

Vertical time coordinate frame

The concept of *vertical time* has a long history in seismic exploration. Vertical time τ is the vertical axis for time migration (Yilmaz, 2001; Claerbout, 1985). It is defined as the *two-way* traveltime measured by coinciding source and receiver on the surface

$$\tau_{TW}(z) = 2\int_0^z \frac{\mathrm{d}z'}{v(z')}. \tag{1}$$

For conventional time image applications, this equation is used in the context of laterally invariant media. This is however, not adequate for imaging complex strudtures. We argue that vertical time, although does not correspond to the actual two-way traveltime in complex velocites, still works fine as representation of the vertical axis. Since wavefield extrapolation is usually not zero-offset, in this work we will use the *one-way* vertical time, defined as

$$\tau(x,y,z) = \int_0^z \frac{\mathrm{d}z'}{v_m(x,y,z')}, \tag{2}$$

Note that velocity v_m does not have to be identical to the velocity in which we propagate wavefields. For example, one can choose a constant v_m, then the vertical time is simply a scaled version of depth, $\tau = z/v_m$. In practice, we suggest using a smooth background velocity as v_m, because it helps regularize τ coordinate grids. Here we retain the name "vertical time" for τ, however, it should not be confused with the vertical time τ_{TW} used in time processing. In other words, Equation 3 represent only a change of variable from z to τ.

Normally, wavefields are discretized on the Cartesian mesh with equally-spaced grids. For a monochromatic wave, wavelength changes with velocity and since the grid spacing is held constant, the number of samples per wavelength increases in layers with high velocities and decreases in layers with low velocities. To avoid spatial aliasing, the maximum grid spacing is limited by $\Delta x \leq v_{\min}/(2f_{\max})$, where $v_{\min}$ is the lowest velocity, often located in shallow layers. As a result, the deep layers with high velocities are often oversampled. The increased sampling of the layers with high velocity raises the cost of wavefield extrapolation without enhancing image resolution. Introducing vertical time partially resolves this problem. This can be seen by taking difference of equation 3 between to time levels,

$$\Delta\tau \equiv \tau_{n+1} - \tau_n = \int_{z(\tau_n)}^{z(\tau_{n+1})} \frac{\mathrm{d}z'}{v_m(x, y, z')}, \tag{3}$$

which corresponds to a fixed τ sampling, $\Delta\tau$. This implies that the effective sampling in depth $z(\tau_{n+1}) - z(\tau_n)$ increases with velocity.

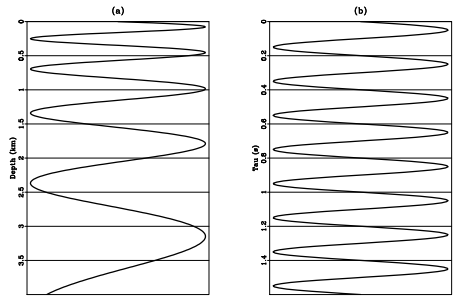

Figure 1: wavelength variation with depth z (Left) and vertical time τ (Right) of a 5Hz sine. The velocity profile is $v = 1500 + 0.7z$ m/sec. tau/vertical uCT

Figure 1 shows a comparison of vertical sampling in depth z and vertical time τ. In the Cartesian domain on the left, the sampling of the wavefield is relatively coarse in shallow layers and becomes finer with depth. In the τ domain on the right, the wavefield is evenly sampled in spite of the velocity variation, for the same number of samples.

Equation 3 maps a depth point (x, y, z) to vertical time point (x, y, τ). The inverse mapping is also straighforward, from differentiation of inverse functions, it follows

$$z(x, y, \tau) = \int_0^{\tau} v_m(x, y, \tau')\mathrm{d}\tau', \tag{4}$$

where the integration constant is zero because $\tau(z = 0) = 0$.

By changing the vertical axis from z to τ, the coordinate system is effectively changed from the Cartesian frame $\{x_1, x_2, x_3\}$ to a new coordinate frame $\{\xi_1, \xi_2, \xi_3\}$, where the two coordinate systems are related by

$$\xi_1 = x_1 \quad , \xi_2 = x_2 \quad , \xi_3 = \tau = \int_0^{x_3} \frac{\mathrm{d}x_3'}{v_m(x_1, x_2, x_3')} \tag{5}$$

As long as the funtions $x_i(\xi_1, \xi_2, \xi_3)$ and $\xi_i(x_1, x_2, x_3)$ are one-to-one and free from singularities, we can interpolate any space functions between the Cartesian and τ

domains. Figures 2(a) to 3(b) illustrate examples of such interpolations. The velocity field in the τ domain is obtained by interpolating the velocity in the Cartesian domain using Equation 3. In Figures 2(a) and 2(b), the mapping velocity v_m is computed by stacking the true velocity v horizontally, and thus it is laterally constant. As a result, the τ coordinate system is orthogonal. In Figures 3(a) and 3(b), τ is computed from the true velocity, i.e. $v_m = v$, the resulting τ coordinate system is nonorthogonal due to the lateral variation of v.

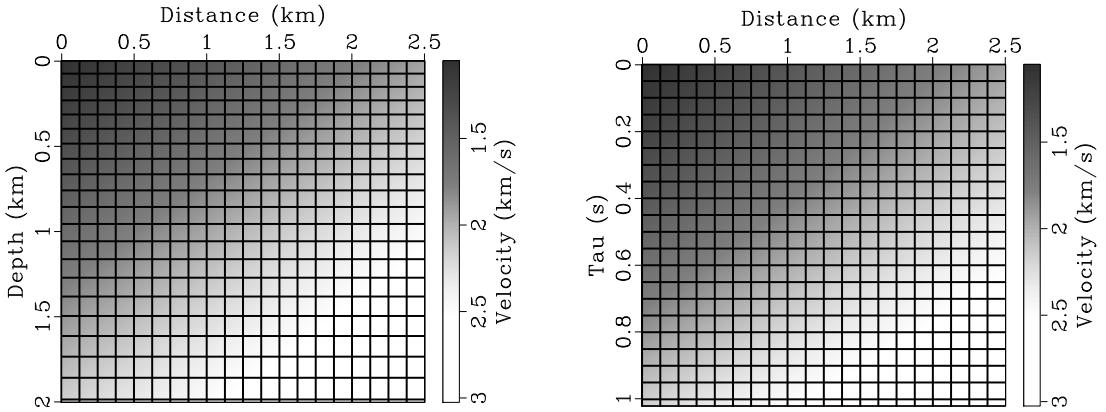

Figure 2: A linear velocity model in (a) Cartesian domain and (b) orthogonal τ domain overlaid with τ domain mesh. The velocity is $v = 1250 + 0.35x + 0.3z$ m/sec. tau/linear linA,linB

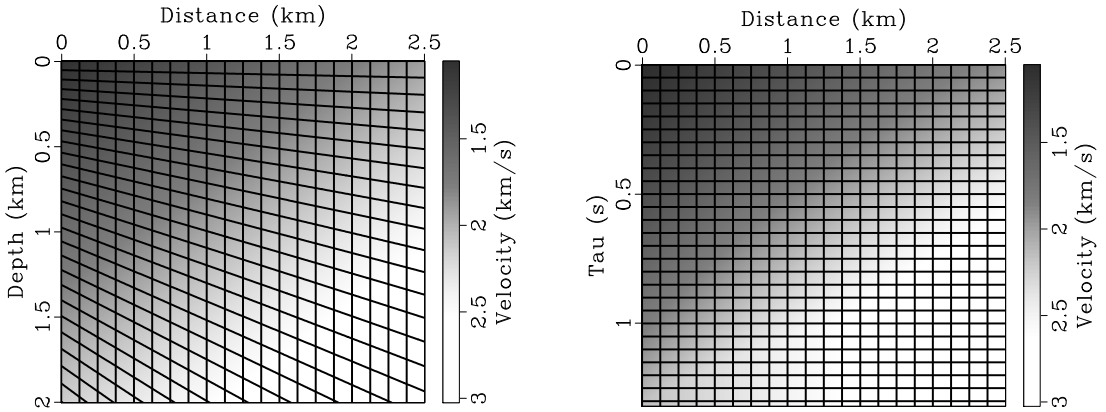

Figure 3: The same velocity model as in Figure 2(a) in (a) Cartesian domain and (b) nonorthogonal τ domain overlaid with τ domain mesh. tau/linear linC,linD

The new coordinate system (x, y, τ) has mixed units of time in the vertical axis and distance in the horizontal axes. Sometime it is more convenient to have distance units in all three axes of the space domain. To achieve this we can simply scale τ by some velocity funciton $\tilde{v}$

$$\tilde{z}(\tau) = \int_0^\tau \tilde{v}(\tau')\mathrm{d}\tau' = \int_0^z \frac{\tilde{v}}{v_m}\mathrm{d}z' \tag{6}$$

For example, if $\tilde{v}$ is set to constant, the pseudodepth is simply a linear scaling of τ, $\tilde{z}(\tau) = \tilde{v}\tau$. The importance of this step will be evident later as we look into anisotropic media.

Isotropic extrapolations

Alkhalifah et al. (2001) obtained τ-domain wave equation by applying a coordinate transformation to the conventional eikonal equation and then develop the dynamic part by inverse Fourier transform in space and time to formulate a wave equation in τ domain. Because of the high frequency assumption of eikonal equation, the resulting wave equation is not accurate in amplitudes. Here, we derive the coordinate transformation to the differentiations in wave equation directly.

From Equations in 5, we can obtain the Jacobian matrix associated with coordinate transformation from Cartesian domain x_i to τ-domain ξ_i

$$\mathbf{J} = \left[\frac{\partial \xi_i}{\partial x_j}\right] = \begin{bmatrix} 1 & 0 & 0 \\ 0 & 1 & 0 \\ \sigma_1 & \sigma_2 & 1/v_m \end{bmatrix}, \tag{7}$$

where we have denoted horizontal variation of vertical time by $\sigma_i = \partial\tau/\partial x_i$ ($i = 1, 2$). The nonzero off-diagonal elements in the Jacobian matrix $\mathbf{J}$ indicate that ξ_i coordinates are nonorthogonal. From the Jacobian matrix we can compute its metric tensor

$$[g^{ij}] = \mathbf{J}\mathbf{J}^T = \begin{bmatrix} 1 & & \sigma_1 \\ & 1 & \sigma_2 \\ \sigma_1 & \sigma_2 & \sigma_1^2 + \sigma_2^2 + \frac{1}{v_m^2} \end{bmatrix}. \tag{8}$$

and its determinant $g = 1/\det(g^{ij}) = v_m^2$. Using the Jacobian matrix defined in 7, we obtain the following derivative transformations:

$$\begin{aligned} \frac{\partial}{\partial x_1} &= \frac{\partial}{\partial \xi_1} + \sigma_1 \frac{\partial}{\partial \xi_3} \\ \frac{\partial}{\partial x_2} &= \frac{\partial}{\partial \xi_2} + \sigma_2 \frac{\partial}{\partial \xi_3} \\ \frac{\partial}{\partial x_3} &= \frac{1}{v_m} \frac{\partial}{\partial \xi_3}. \end{aligned} \tag{9}$$

A brief overview of the relevant tensor calculus theory is enclosed in Appendix A.

The two-way wave equation may be written in the following first order system

$$\frac{\partial p}{\partial t} = v^2 \nabla \cdot \mathbf{q} \quad \text{and} \quad \frac{\partial \mathbf{q}}{\partial t} = \nabla p, \tag{10}$$

where p is stress and $-\mathbf{q}$ is particle momentum. The gradient of a scalar ϕ in a general curvilinear coordinate frame ξ_i is

$$\nabla \phi = \frac{\partial \phi}{\partial \xi_j} g^{ij} \mathbf{e}_i, \tag{11}$$

which upon substitution of τ domain metric tensor 8 gives the following form of the τ domain gradient operator

$$\begin{aligned}\nabla\phi = &\left(\frac{\partial\phi}{\partial\xi_1} + \sigma_1\frac{\partial\phi}{\partial\xi_3}\right)\mathbf{e}_1 \\ &+ \left(\frac{\partial\phi}{\partial\xi_2} + \sigma_2\frac{\partial\phi}{\partial\xi_3}\right)\mathbf{e}_2 \\ &+ \left[\sigma_1\frac{\partial\phi}{\partial\xi_1} + \sigma_2\frac{\partial\phi}{\partial\xi_2} + \left(\sigma_1^2+\sigma_2^2+\frac{1}{v_m^2}\right)\frac{\partial\phi}{\partial\xi_3}\right]\mathbf{e}_3.\end{aligned} \tag{12}$$

The divergence of vector $f = f_i\mathbf{e}_i$ in a general curvilinear coordinate frame ξ_i is

$$\nabla\cdot\mathbf{f} = \frac{1}{\sqrt{g}}\frac{\partial}{\partial\xi_i}\left(\sqrt{g}f_i\right). \tag{13}$$

Similarly we can find the τ domain divergence using equation 8 as follows

$$\nabla\cdot\mathbf{f} = \frac{1}{v_m}\frac{\partial}{\partial\xi_i}\left(v_m f_i\right) \tag{14}$$

A τ domain two-way wave equation is established by substituting the gradient and divergence operators in equations 12 and 14 into equation 10,

$$\begin{aligned}\frac{\partial p}{\partial t} &= \frac{v^2}{v_m}\sum_{i=1}^{3}\frac{\partial}{\partial\xi_i}\left(v_m q_i\right) \\ \frac{\partial q_i}{\partial t} &= \frac{\partial p}{\partial\xi_i} + \sigma_i\frac{\partial p}{\partial\xi_3} \quad (i=1,2) \\ \frac{\partial q_3}{\partial t} &= \sigma_1\frac{\partial p}{\partial\xi_1} + \sigma_2\frac{\partial p}{\partial\xi_2} + \left(\sigma_1^2+\sigma_2^2+\frac{1}{v_m^2}\right)\frac{\partial p}{\partial\xi_3}.\end{aligned} \tag{15}$$

This new wave equation is seemingly more complex then the normal two-way wave equation 10. It, however, does not raise the computational cost significantly because the number of differentiations on the right-hand side of the system is 6 for both Equations 15 and 10. The only cost increase comes from the multiplication with the σ_i terms, which is less costly than differentiations. As will be shown in the next section, the additional cost due to σ_i terms is in practice offset by an efficiency gain due to reduced vertical sampling.

If the τ coordinate system is orthogonal, in other words, v_m is laterally constant, and thus, $\sigma_i = 0$, then the Jacobian matrix becomes diagonal $\mathbf{J} = \mathrm{diag}(1,1,1/v_m)$ and the metric tensor $g^{ij} = \mathrm{diag}(1,1,1/v_m^2)$. The two-way wave equation 15 simplifies to

$$\begin{aligned}\frac{\partial p}{\partial t} &= v^2\sum_{i=1}^{2}\frac{\partial q_i}{\partial\xi_i} + \frac{v^2}{v_m}\frac{\partial}{\partial\xi_3}\left(v_m q_3\right) \\ \frac{\partial q_i}{\partial t} &= \frac{\partial p}{\partial\xi_i} \quad (i=1,2) \\ \frac{\partial q_3}{\partial t} &= \frac{1}{v_m^2}\frac{\partial p}{\partial\xi_3}.\end{aligned} \tag{16}$$

The simplicity of this equation allows us to reorganize it into a second-order form

$$\frac{\partial^2 p}{\partial t^2} = v^2 \left(\frac{\partial^2 p}{\partial x^2} + \frac{\partial^2 p}{\partial y^2} \right) + \frac{v^2}{v_m} \frac{\partial}{\partial \tau} \left(\frac{1}{v_m} \frac{\partial p}{\partial \tau} \right), \tag{17}$$

which upon expansion becomes

$$\frac{\partial^2 p}{\partial t^2} = v^2 \left(\frac{\partial^2 p}{\partial x^2} + \frac{\partial^2 p}{\partial y^2} \right) + \frac{v^2}{v_m^2} \frac{\partial^2 p}{\partial \tau^2} - \frac{v^2}{v_m^3} \frac{\partial v_m}{\partial \tau} \frac{\partial p}{\partial \tau}. \tag{18}$$

Since the first-order derivatives affect only the amplitude of the solution (Courant and Hilbert, 1989), the last term in Equation 18 can be dropped while retaining a kinematically correct solution, the resulting wave equation is

$$\frac{\partial^2 p}{\partial t^2} = v^2 \left(\frac{\partial^2 p}{\partial x^2} + \frac{\partial^2 p}{\partial y^2} \right) + \frac{v^2}{v_m^2} \frac{\partial^2 p}{\partial \tau^2}. \tag{19}$$

When both v and v_m are constants, the wavefront described by Equation 19 is an ellipse. This suggests that elliptical anisotropy can be viewed as a linear change of the variable $\tau = z/v_m$ to isotropic velocity.

Anisotropic extrapolation

Velocity variation with angle in anisotropic media allows more choices for the mapping velocity v_m in Equation 3. It is natural to use, but not limited to, the vertical velocity, v_v, as v_m.

The kinematics of a quasi-P wave in an anisotropic acoustic medium can be characterized by three parameters: P-wave velocity in the direction of the axis of symmetry v_v, NMO velocity $v = v_v\sqrt{1+2\delta}$ and anellipticity $\eta = (\epsilon - \delta)/(1+2\delta)$ (Alkhalifah, 2000), here ϵ and δ are Thomsen parameters (Thomsen, 1986).

The quasi-P wave motion in transversely isotropic media with vertical axis of symmetry (VTI) is described by the following first-order system (Duveneck and Bakker, 2011)

$$\begin{aligned}
\frac{\partial p_H}{\partial t} &= (1+2\eta) v^2 \left(\frac{\partial q_1}{\partial x_1} + \frac{\partial q_2}{\partial x_2} \right) + v v_v \frac{\partial q_3}{\partial x_3} \\
\frac{\partial p_V}{\partial t} &= v v_v \left(\frac{\partial q_1}{\partial x_1} + \frac{\partial q_2}{\partial x_2} \right) + v_v^2 \frac{\partial q_3}{\partial x_3} \\
\frac{\partial q_i}{\partial t} &= \frac{\partial p_H}{\partial x_i} \quad (i = 1, 2) \\
\frac{\partial q_3}{\partial t} &= \frac{\partial p_V}{\partial x_3},
\end{aligned} \tag{20}$$

where p_H and p_V are horizontal and vertical stresses, $-\mathbf{q}$ is the particle momentum.

In the τ domain, the wave equation is obtained by applying the chain rule 9 to 20, the resulting system of equations is

$$\begin{aligned}
\frac{\partial p_H}{\partial t} &= (1+2\eta)v^2 \sum_{i=1}^{2} \left(\frac{\partial q_i}{\partial \xi_i} + \sigma_i \frac{\partial q_i}{\partial \xi_3} \right) + \frac{v v_v}{v_m} \frac{\partial q_3}{\partial \xi_3} \\
\frac{\partial p_V}{\partial t} &= v v_v \sum_{i=1}^{2} \left(\frac{\partial q_i}{\partial \xi_i} + \sigma_i \frac{\partial q_i}{\partial \xi_3} \right) + \frac{v_v^2}{v_m} \frac{\partial q_3}{\partial \xi_3} \\
\frac{\partial q_i}{\partial t} &= \frac{\partial p_H}{\partial \xi_i} + \sigma_i \frac{\partial p_H}{\partial \xi_3} \quad (i = 1, 2) \\
\frac{\partial q_3}{\partial t} &= \frac{1}{v_m} \frac{\partial p_V}{\partial \xi_3}
\end{aligned} \tag{21}$$

Equation 20 has the second-order form

$$\begin{aligned}
\frac{\partial^2 p_H}{\partial t^2} &= (1+2\eta)v^2 \left(\frac{\partial^2}{\partial x_1^2} + \frac{\partial^2}{\partial x_2^2} \right) p_H + v v_v \frac{\partial^2 p_V}{\partial x_3^2} \\
\frac{\partial^2 p_V}{\partial t^2} &= v v_v \left(\frac{\partial^2}{\partial x_1^2} + \frac{\partial^2}{\partial x_2^2} \right) p_H + v_v^2 \frac{\partial p_V}{\partial x_3^2}.
\end{aligned} \tag{22}$$

Similarly, the second order form of 21 is

$$\begin{aligned}
\frac{\partial^2 p_H}{\partial t^2} &= (1+2\eta)v^2 \left[\left(\frac{\partial}{\partial \xi_1} + \sigma_1 \frac{\partial}{\partial \xi_3} \right)^2 + \left(\frac{\partial}{\partial \xi_2} + \sigma_2 \frac{\partial}{\partial \xi_3} \right)^2 \right] p_H + \frac{v v_v}{v_m} \frac{\partial}{\partial \xi_3} \left(\frac{1}{v_m} \frac{\partial p_V}{\partial \xi_3} \right) \\
\frac{\partial^2 p_V}{\partial t^2} &= v v_v \left[\left(\frac{\partial}{\partial \xi_1} + \sigma_1 \frac{\partial}{\partial \xi_3} \right)^2 + \left(\frac{\partial}{\partial \xi_2} + \sigma_2 \frac{\partial}{\partial \xi_3} \right)^2 \right] p_H + \frac{v_v^2}{v_m} \frac{\partial}{\partial \xi_3} \left(\frac{1}{v_m} \frac{\partial p_V}{\partial \xi_3} \right)
\end{aligned} \tag{23}$$

In addition to the cost reduction, the vertical time axis also allows time processing in VTI media to be independent of the vertical velocity v_v, which is usually unresolvable from surface seismic data.

In transversely isotropic media with tilted axis of symmetry (TTI), the symmetry plane and symmetry axis are rotated by tilt angle θ and azimuth ϕ. The two-way wave equation is obtained by substituting derivatives in Equation 20 by the following relations

$$\begin{aligned}
\frac{\partial}{\partial x_1} &\leftarrow \cos\theta \cos\phi \frac{\partial}{\partial x_1} + \cos\theta \sin\phi \frac{\partial}{\partial x_2} - \sin\theta \frac{\partial}{\partial x_3} \\
\frac{\partial}{\partial x_2} &\leftarrow -\sin\phi \frac{\partial}{\partial x_1} + \cos\phi \frac{\partial}{\partial x_2} \\
\frac{\partial}{\partial x_3} &\leftarrow \sin\theta \cos\phi \frac{\partial}{\partial x_1} + \sin\theta \sin\phi \frac{\partial}{\partial x_2} + \cos\theta \frac{\partial}{\partial x_3}.
\end{aligned} \tag{24}$$

In τ domain, the TTI extrapolation equation is obtained by replacing each of the spatial derivatives $\partial/\partial x_i$ $(i = 1, 2, 3)$ on the right-hand side of Equation 24 by the expressions given by chain rule in Equation 9. The τ coordinate transformation does not affect stability of the extrapolation.

Implementation aspects

The Sampling of the τ axis should be small enough to avoid wavefield aliasing in the τ domain, for example

$$\Delta\tau \leq \frac{1}{10}\frac{v_{min}}{f_{max}}, \tag{25}$$

where v_{min} is the minimum velocity in the model and f_{max} is the maximum frequency of the wave. Accordingly, the number of samples representing the τ axis should be chosen to cover the largest expected τ value,

$$n_\tau \Delta\tau \geq \max_{x,y} \int_0^z \frac{\mathrm{d}z'}{v_m(x,y,z')}. \tag{26}$$

The mapping velocity v_m is often chosen as a slightly smoothed version of true velocity v. This is because the τ domain wave equation involves a differentiation of v_m, for example the first equation in 15.

For second-order wave equations, the operators on the right-hand side can become significantly complicated in the τ domain, such as Equation 23. Thus, it is more convenient to code up its first-order form 21. For consistency, we will extrapolate the wavefields using the first-order form for all the examples in this paper. Thus, the time derivatives in these equations are approximated by central differences,

$$\frac{\partial p}{\partial t} \approx \frac{p^{n+1} - p^{n-1}}{2\Delta t}, \tag{27}$$

and the spatial derivatives are approximated using the Fourier pseudospectral approuch (Gazdag, 1981; Carcione et al., 2002), as follows

$$\frac{\partial p}{\partial x_1} \approx F_1^{-1}\{\mathrm{i}k_1 F_1\{p\}\}, \tag{28}$$

where superscript n indicate time steps, F_i is the spatial Fourier transform in the x_i direction. The change of the vertical axis from z to τ does not affect the stability condition. For both isotropic and VTI extrapolations, the same time-step is used in both the Cartesian and τ domains.

EXAMPLES

Impulse responses

The τ domain wave equations in the previous section are derived for 3D models. For simplicity, the examples in this paper is for D models. Since the change in the vertical axis acts on a single vertical velocity profile at a time, the conclusions in this section can be extended to 3D case. To test the accuracy of the τ domain wavefield

extrapolation, we look at impulse responses of the τ domain migration operators and compare them with those obtained from the Cartesian domain extrapolations. A synthetic zero-offset section with three spikes are illustrated in Figure 4. Migration images obtained from this section are superpositions of the Green's functions due to a point source located at the center on the surface.

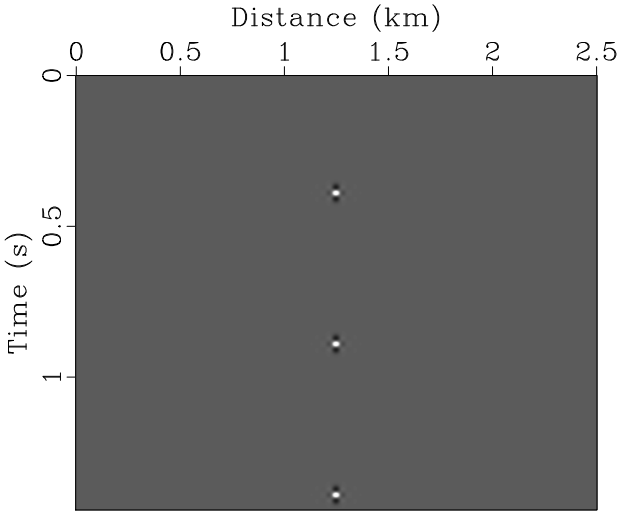

Figure 4: Zero-offset section with three impulse events equally spaced in time. The source has peak frequency of 20Hz. The lag between impulses is 0.5sec. tau/lens spike

Our first example is a lens velocity model, shown in Figure 5(a). The background velocity is $v = 2100 + .025z + .14x$ m/sec and contains a negative anomaly of -750 m/sec. We use the same velocity to obtain vertical time τ, i.e. $v_m = v$ in Equation 3. The τ mesh is overlaid on the velocity model, a prominent "pull-down" near the bottom of the model is due to the slow velocity lens. By the same analogy, a "push-up" will appear in the τ domain beneath a positive velocity anomaly, for example a salt body. By applying the change of variable in Equation 3, the velocity is interpolated to the τ domain and plotted in Figure 5(b). The τ axis is discretized by 401 samples to speedup extrapolation and honor the aliasing condition. The zero-offset section in Figure 4 is migrated using Equation 10 by extrapolating backward in time and applying zero-time imaging condition. The resulting image is shown in Figure 5(c). In the τ domain, the extrapolation is done by solving Equation 15. Following the same imaging condition, the migrated image is shown in Figure 5(d). This image is then interpolated back to the Cartesian domain using equation 4, and compared with Figure 5(c). The error shown in Figure 5(f) is due to the linear interpolation between Cartesian and τ meshes, and it is relatively small.

The next examples demonstrate extrapolation in complex models. In Figure 6(a), we show a section of the isotropic Marmousi velocity model. Since the vertical time derived from this velocity has very ragged curvatures that may pose stability difficulties for the τ domain extrapolation, in Equation 3 we use instead a smoothed version of the Marmousi velocity as v_m to compute τ. Interpolation of the Marmousi velocity on to the τ mesh is shown in Figure 6(b). Impulse responses are obtained by solving Equations 10 (Figure 6(c)) and 15 (Figure 6(d)). The error is plotted in Figure 6(f) and it is relatively small.

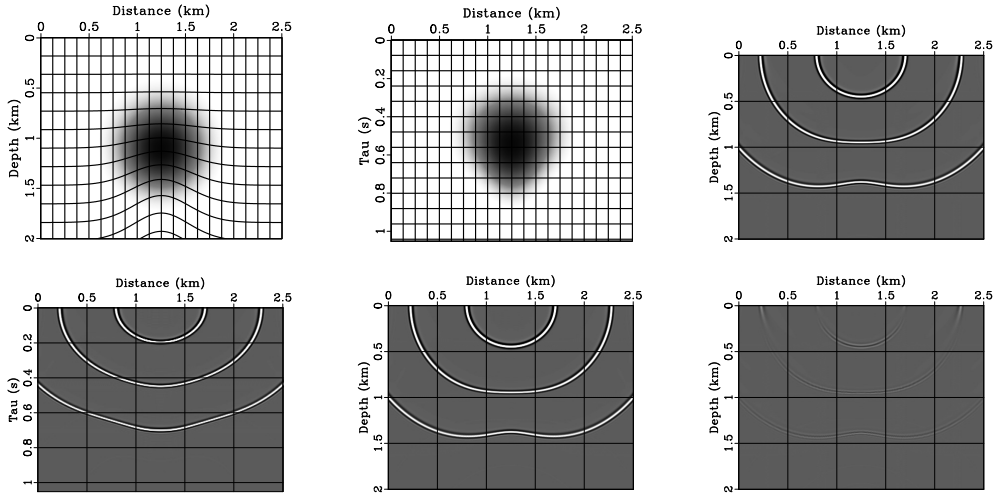

Figure 5: A lens velocity model in (a) Cartesian and (b) τ domains overlaid with τ mesh. Migration images are shown for (c) Cartesian and (d) τ domains. (e) is image (d) interpolated to the Cartesian domain. (f) is the relative error between (c) and (e). The model is discretized with 501 samples in depth and 401 samples in vertical time. tau/lens lengC,lengT,leniC,leniT,leniB,leniE

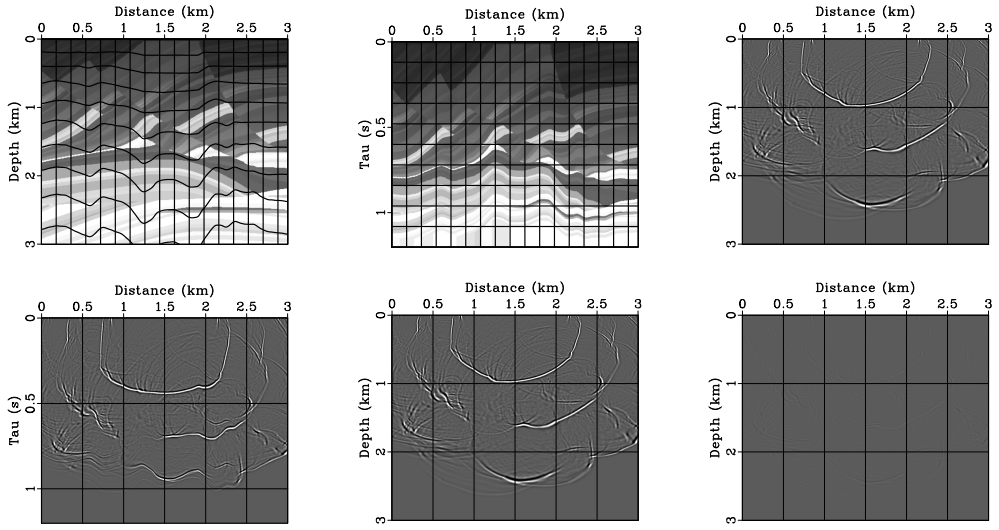

Figure 6: A portion of the Marmousi velocity in (a) Cartesian and (b) τ domains overlaid with the τ mesh. Migration images are shown for (c) Cartesian and (d) τ domains. (e) is image (d) interpolated to the Cartesian domain. (f) is the relative error between (c) and (e). The model is discretized with 751 samples in depth and 501 samples vertical time. The mapping velocity v_m is smoothed from true velocity by using 8-point triangle filter. tau/marm margC,margT,mariC,mariT,mariB,mariE

Extrapolation of anisotropic wavefields in the τ coordinates system is also feasible. The propagation of quasi-acoustic P waves is characterized by three parameters: vertical P-wave velocity v_v, NMO velocity v and the anellipticity η. For example, the anisotropic parameters of the SEG/Hess model are shown in Figures 7(a) to 7(c).

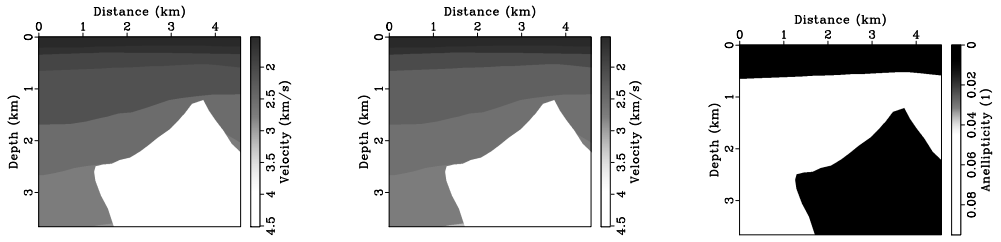

Figure 7: A portion of the SEG/Hess anisotropic velocity model. (a) Vertical velocity (b) NMO velocity (c) η. tau/hess hesm1,hesm2,hesm3

Similar to isotropic complex models, to alleviate the distortion of the τ mesh due to the strong velocity variation of the salt body, the τ mesh is constructed using a smooth background velocity v_m. The resulting τ coordinate system is overlaid on vertical velocities in the Cartesian and τ domains, shown in Figure 8(a) and 8(b). The Cartesian domain impulse response is computed from Equation 20, Figure 8(c) shows the horizontal stress field p_H. In the τ domain, the impulse response is obtained from equation 21, and the resulting p_H field is shown in Figure 8(d). As expected, the wavefield beneath the salt is "pushed up" due to positive velocity anomaly at salt dome. The error in the migration image obtained in τ domain is plotted in Figure 8(f).

Table 1 summarizes the numerical cost of wavefield extrapolation in Cartesian and τ domains. For isotropic extrapolations, elapsed time is shorter in τ domain than in Cartesian domain, the percentage cut is close to the reduction of vertical sampling of the wavefield. For anisotropic extrapolations, the efficiency improvement is less significant, due to the increased number of derivatives on the right-hand side of equations 21 as compared to Cartesian extrapolator 20.

Model	n_c	n_τ	reduction	t_c	t_τ	speedup
Lens (Figure 5(a))	401	251	37.5%	18	12	33.3%
Marmousi (Figure 6(a))	751	501	33.3%	277	193	30.3%
SEG/Hess (Figure 8(a))	601	501	16.6%	102	98	3.9%

Table 1: Cost of wavefield extrapolation in Cartesian (c) and τ (τ) domain, showing elapsed time t in seconds and number of vertical samples n. Reduction of samples are computed by $(n_c - n_\tau)/n_c$. Speedup is estimated by $(t_c - t_\tau)/tc$.

In addition to the reduced computational cost, τ anisotropic extrapolation also features attenuated shear wave artifacts. Figure 9 shows the impulse responses using

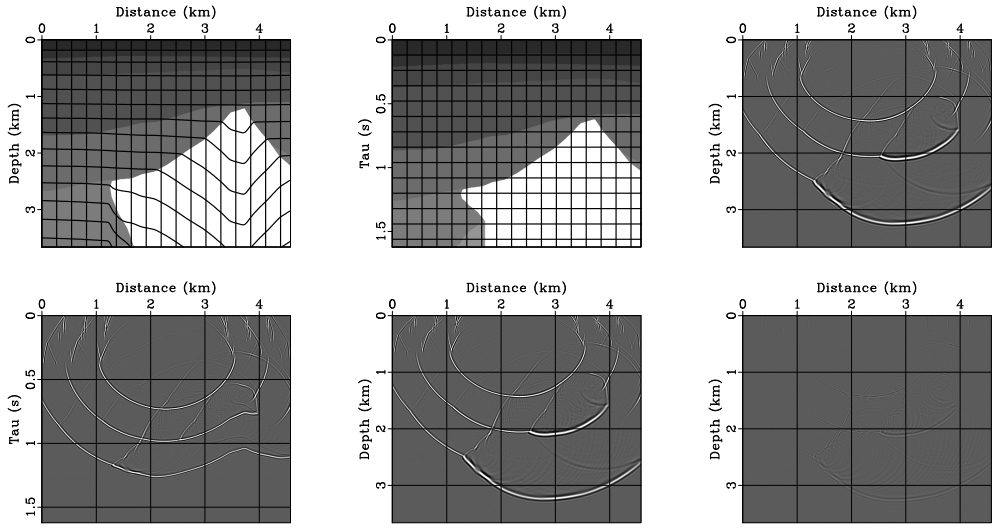

Figure 8: The vertical velocity in (a) the Cartesian and (b) the τ domains overlaid with τ mesh. Migration images are shown for (c) Cartesian and (d) τ domains. (e) is image (d) interpolated to the Cartesian domain. (f) is the relative error between (c) and (e). The model is discretized with 601 samples in depth and 501 samples vertical time. The mapping velocity v_m is smoothed from true velocity by using 8-point triangle filter. tau/hess hesgC,hesgT,hesiC,hesiT,hesiB,hesiE

a homogeneous anisotropic velocity model. The shear wave artifact is significant in the Cartesian domain, shown on the left. In the τ domain, the artifact is attenuated with the coarser vertical sampling, as shown on the right. Coarser sampling enhance numerical dispersion of the shear wave, which tends to spread the energy across the domain, thus attenuates the shear wave artifact.

Prestack imaging

Using the τ domain two-way wave equation 15, we apply reverse-time migration to Sigsbee2a synthetic dataset. Figure 10(a) shows a standard RTM image obtained in the Cartesian domain. The vertical axis, depth z, is discretized into 1201 samples. Figure 10(b) shows an RTM image obtained in τ domain. The vertical axis has been replaced by vertical time τ, with 751 samples. Thus, the model size in the τ domain has been reduced by 37.5% compared to the Cartesian domain. Measured by wall clock times, the τ domain RTM gained a total of 33% speedup compared to Cartesian domain RTM, which as expected, is close to the reduction of the model size.

Similarly, anisotropic reverse-time migration can be implemented using Equation 21. Figure 11(a) illustrates a migrated image of the SEG/Hess salt dataset, with 1500 samples in vertical direction. In the τ domain, the models are discretized into 1200 samples in vertical direction. Figure 11(b) illustrates the τ domain migration

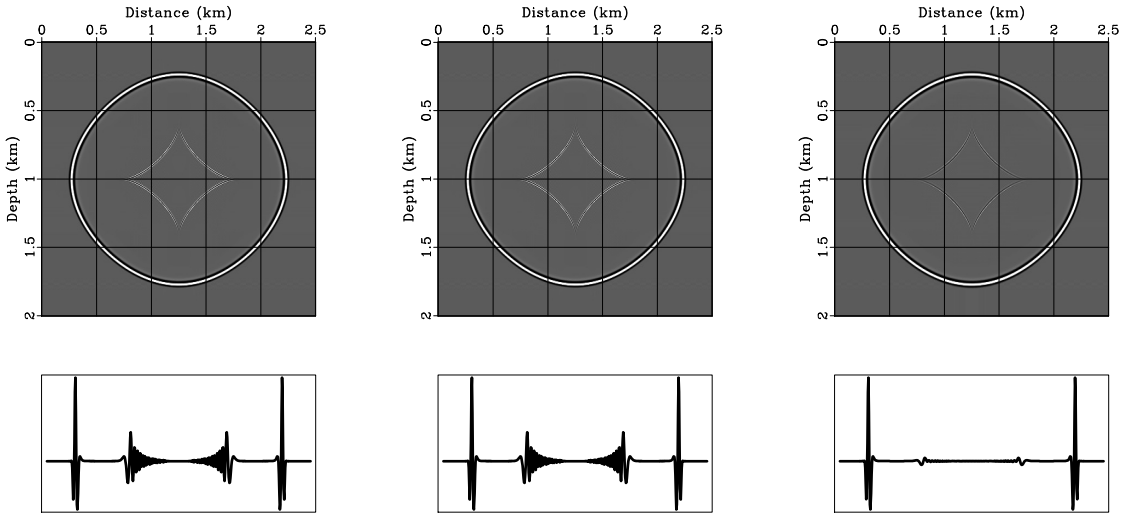

Figure 9: Anisotropic impulse response obtained in Cartesian (Left) and τ (Middle and Right) domains, showing attenuation of the shear wave artefact. In the Middle figure, the τ axis is sampled at $\Delta\tau = 2.5$ msec with 401 samples. In the Right figure, the τ axis is sampled at $\Delta\tau = 3.0$ msec with 301 samples. The anisotropic model has vertical velocity 2000 m/sec, NMO velocity 1643 m/sec and anellipticity $\eta = 0.1$. tau/arte arteC,arteZ,arteT

image. Again, the τ domain RTM has seen 18% speedup, due to a corresponding sampling reduction of 20%. Note as well that the first two reflections in the τ domain result is not aliased compared to its depth counterpart. This implies that if these reflections are crucial, then we will require even a denser depth sampling to avoid aliasing up shallow. This will result in even a larger cost difference.

CONCLUSION

The oversampling of wavefields in the vertical direction is effectively resolved by converting the vertical axis from depth to vertical time. Depending on lateral variation of the chosen vertical time, the resulting coordinate system can be made orthogonal or nonorthogonal. We derived wave equations for time extrapolation of both isotropic and anisotropic wavefields in the vertical time coordinate frame. Extrapolation in the vertical time domain features reduced computation cost due to elimination of oversampling in vertical direction. Using the τ domain extrapolators, over 30% speedup are observed for both isotropic and anisotropic RTMs.

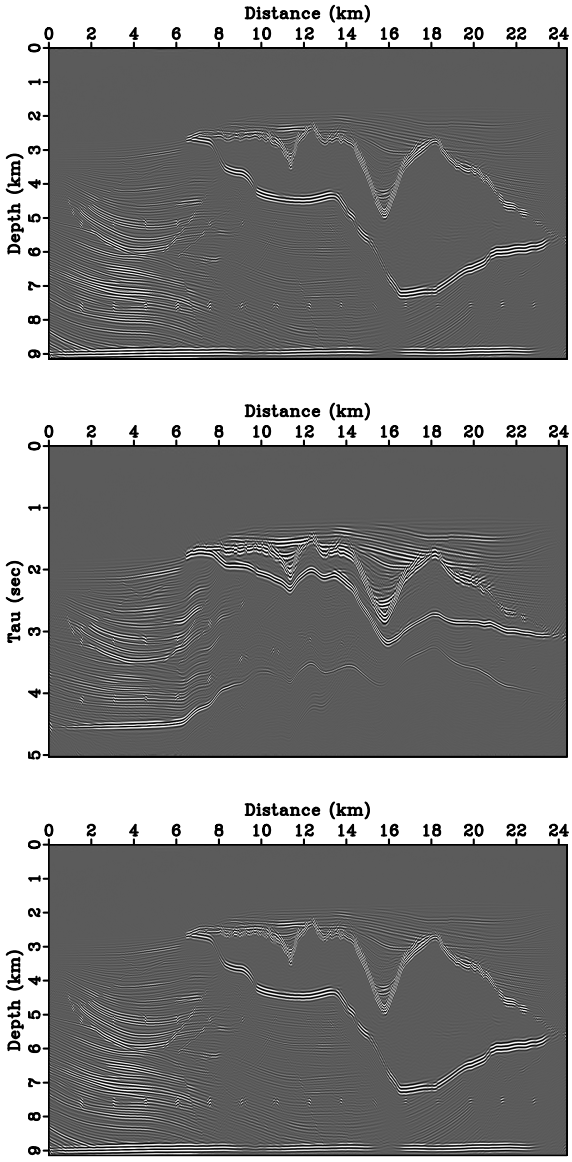

Figure 10: Prestack migration of the Sigsbee dataset. Images are obtained in (a) Cartesian and (b) τ domains. (c) is Figure (b) interpolated to Cartesian domain. The computational cost measured by wall clock time is 19h36min for (a) and 13h03min for (b). tau/. sigsC,sigsT,sigsB

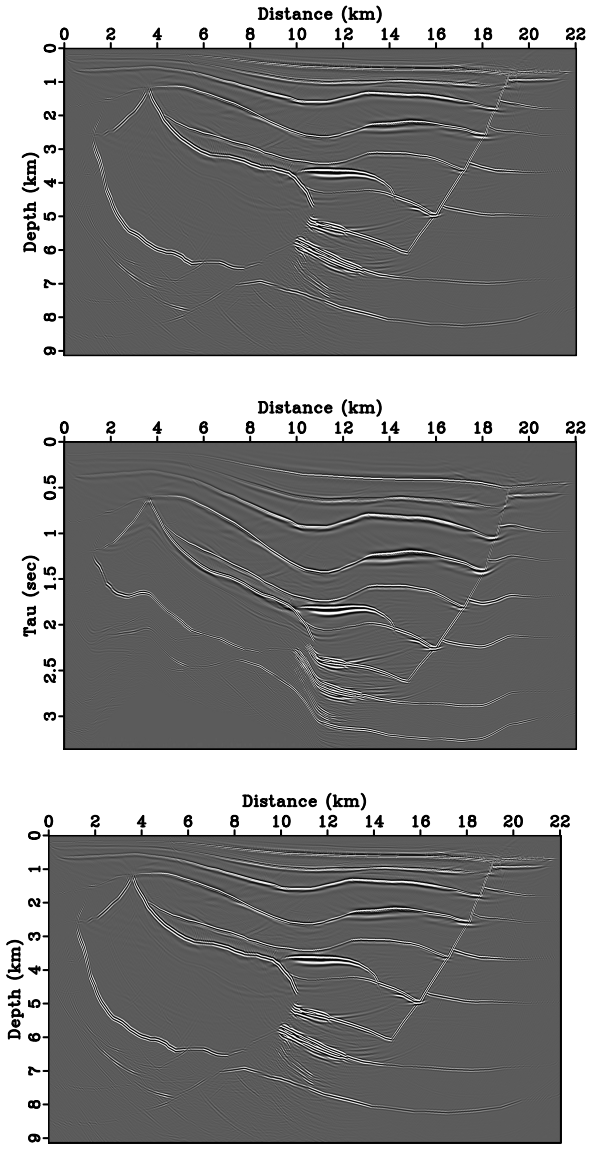

Figure 11: Prestack migration of the SEG/Hess dataset. Images are obtained in (a) Cartesian and (b) τ domains. (c) is Figure (b) interpolated to Cartesian domain. The computational cost measured by wall clock time is 24h24min for (a) and 20h02min for (b). tau/. hessC,hessT,hessB

ACKNOWLEDGMENTS

We thank KAUST for supporting this work. We are grateful to Mohammad Zuberi and Yunseok Choi for many helpful discussions. The oustanding reviews by Alexey Stovas, Yu Zhang and an anonymous reviewer had great improved this manuscript. We acknowledge Hess Corporation and SMAART consortium for releasing their synthetic salt datasets.

APPENDIX A: OVERVIEW OF TENSOR CALCULUS

Transofrmation between general coordinates is conveniently handled by tensor calculus. We consider a genearl curvilinear, possibly nonorthogonal, coordinate system $\{\xi_1, \xi_2, \xi_3\}$ and Cartesian coordinates $\{x_1, x_2, x_3\}$. At each point $\mathbf{r}(\xi_1, \xi_2, \xi_3)$ in space, two sets of basis vectors exist: *covariant vectors* $\mathbf{e}_i = \partial\mathbf{r}/\partial\xi_i$ and *contravariant vectors* $\mathbf{e}^i = \nabla\xi_i$. Basis vectors $\mathbf{e}_i$ and $\mathbf{e}^i$ are, in general, not of unit length. A *metric tensor* is a second-order symmetric tensor from which the unit arc length, unit area and unit volume can be computed easily. Each element of the *covariant metric tensor* g_{ij} is the inner product of a pair of covariant vectors, $g_{ij} = \mathbf{e}_i \cdot \mathbf{e}_j$. The *contravariant metric tensor* is defined similarly, $g^{ij} = \mathbf{e}^i \cdot \mathbf{e}^j$. The two metric tensors form a pair of inverse matrices $g_{ij} = [g^{ij}]^{-1}$. If the curvilinear coordinate system ξ_i is orthogonal, for example spherical coordinates, the two basis vectors coincide and metric tensors become diagonal matrices.

Transformations between coordinate systems are characterized by *Jacobian matrix* $\mathbf{J}$, defined as $J_{ij} = \partial x_i'/\partial x_j$ for the transformation from coordinate system x_i to x_i'. In the case that x_i is Cartesian coordinates, we noticed that each row of $\mathbf{J}$ is one contravariant basis vector $\mathbf{e}^i$, thus the metric tensors can be computed from Jacobian matrix, $[g^{ij}] = \mathbf{J}\mathbf{J}^T$ and $[g_{ij}] = (\mathbf{J}\mathbf{J}^T)^{-1}$.

Once the basis vectors and metric tensors are known, differentiations in the curvilinear coordinates ξ_i is straightforward. The gradient of scalar ϕ is (Riley et al., 2006)

$$\nabla\phi = \frac{\partial\phi}{\partial\xi_j} g^{ij}\mathbf{e}_i, \tag{F-1}$$

and the divergence of $\mathbf{f} = f_i\mathbf{e}_i$ is

$$\nabla\cdot\mathbf{f} = \frac{1}{\sqrt{g}}\frac{\partial}{\partial\xi_i}\left(\sqrt{g}f_i\right) \tag{F-2}$$

where $g = \det(g_{ij})$. Combining these two expression give the Laplacian of scalar ϕ

$$\nabla^2\phi = \frac{1}{\sqrt{g}}\frac{\partial}{\partial\xi_i}\left(\sqrt{g}g^{ij}\frac{\partial\phi}{\partial\xi_j}\right). \tag{F-3}$$

APPENDIX B: τ DOMAIN TRAVELTIME

A geometrical description of the τ domain isotropic wavefield can be achieved by looking at its eikonal. A dispersion relation associated with the τ domain wave equation 15 is obtained by taking Fourier transform of this equation in space and time, specifically, do the substitution $\partial t \rightarrow -i\omega$ and $\partial x_i \rightarrow ik_i$, the result is

$$\frac{\omega^2}{v^2} = \sum_{i=1}^{2} \left(k_i + \sigma_i k_3\right)^2 + \frac{k_3^2}{v_m^2}. \tag{G-1}$$

Note here k_1 and k_2 has units of rad/m, while k_3 has the angular frequency unit of rad/sec.

We then relate slowness vector $\mathbf{p}$ with wavenumber vector $\mathbf{k}$ by $\mathbf{k} = \omega\mathbf{p}$, thus the τ domain isotropic eikonal equation is

$$\frac{1}{v^2} = \sum_{i=1}^{2} \left(p_i + \sigma_i p_3\right)^2 + \frac{p_3^2}{v_m^2} \tag{G-2}$$

where $p_i = \partial T/\partial x_i$ is the component of slowness vector in the x_i direction, T is traveltime. Similarly, while p_1 and p_2 has slowness units sec/m, p_3 is dimensionless. Alternatively, Equation G-2 can be derived by applying chain rule 9 to the Cartesian domain eikonal $\sum_{i=1}^{3} p_i^2 = 1/v^2$.

APPENDIX C: STABILITY ANALYSIS FOR τ DOMAIN EXTRAPOLATION

For homogeneous velocity and regularly spaced grids, the stability condition is often studied by Von Neumann analysis (Trefethen, 1994). Consider 1-D second-order wave equation,

$$u_{tt} = v^2 u_{zz}, \tag{H-1}$$

approximated by central difference in space and time

$$\frac{u_i^{n+1} - 2u_i^n + u_i^{n-1}}{\Delta t^2} = v^2 \frac{u_{i+1}^n - 2u_i^n + u_{i-1}^n}{\Delta z^2} \tag{H-2}$$

where superscripts indicate time index and subscripts indicate space index. Substitute ansatz $u_i^n = U^n \exp\left(\mathrm{i}\, k z_j\right)$ into Equation H-2 yields

$$U^2 + \left(4\frac{v^2\Delta t^2}{\Delta z^2}\sin^2\frac{k\Delta z}{2} - 2\right)U + 1 = 0 \tag{H-3}$$

where amplification factor U characterizes the growth of the numerical solution during iteration. Stability of the numerical solution requires $|U| \leq 1$ for all wavenumbers k. It can be shown that in order for the quadratic equation

$$U^2 + \beta U + 1 = 0 \tag{H-4}$$

to have bounded roots $|U| \leq 1$, it is necessary that $|\beta| \leq 2$. This is equivalent to

$$0 \leq \frac{v^2 \Delta t^2}{\Delta z^2} \sin^2 \frac{k \Delta z}{2} \leq 1 \quad \forall\, k \tag{H-5}$$

thus yields the well-known CFL condition

$$\Delta t \leq \frac{\Delta x}{v}. \tag{H-6}$$

In τ domain, the 1-D problem can be extracted from the vertical component of Equation 19

$$u_{tt} = \frac{v^2}{v_m^2} u_{\tau\tau}. \tag{H-7}$$

Following the same analysis for H-2, we can obtain τ domain CFL condition

$$\Delta t \leq \frac{v_m}{v} \Delta \tau \tag{H-8}$$

REFERENCES

Alkhalifah, T., 2000, An acoustic wave equation for anisotropic media: Geophysics, **65**, 1239–1250.

Alkhalifah, T., S. Fomel, and B. Biondi, 2001, The space-time domain: theory and modelling for anisotropic media: Geophysical Journal International, **144**, 105–113.

Carcione, J., G. C. Herman, and A. P. E. ten Kroode, 2002, Seismic modeling: Geophysics, **67**, 1304–1325.

Claerbout, J. F., 1985, Imaging the earth's interior: Blackwell Scientific Publications.

Duveneck, E., and P. M. Bakker, 2011, Stable p-wave modeling for reverse-time migration in tilted ti media: Geophysics, **76**, S65–S75.

Gazdag, J., 1981, Modeling of the acoustic wave equation with transform methods: Geophysics, **46**, 854–859.

Riley, K., M. Hobson, and S. Bence, 2006, Mathematical methods for physics and engineering: Cambridge University Press.

Sava, P., and S. Fomel, 2005, Riemannian wavefield extrapolation: Geophysics, **70**, T45–T56.

Shan, G., and B. Biondi, 2008, Plane-wave migration in tilted coordinates: Geophysics, **73**, S185–S194.

Shragge, J. C., 2008, Riemannian wavefield extrapolation: Nonorthogonal coordinate systems: Geophysics, **73**, T11–T21.

Thomsen, L., 1986, Weak elastic anisotropy: Geophysics, **51**, 1954–1966.

Trefethen, L., 1994, Finite difference and spectral methods for ordinary and partial differential equations: Unpublished, available online.

Yilmaz, 2001, Seismic data analysis: Processing, inversion, and interpretation of seismic data: Society of Exploration Geophysicists.

Automatic traveltime picking using the instantaneous traveltime

Christos Saragiotis, Tariq Alkhalifah*, and Sergey Fomel†**

ABSTRACT

Event picking is used in many steps of seismic processing. We present an automatic event picking method that is based on a new attribute of seismic signals, the instantaneous traveltime. The calculation of the instantaneous traveltime consists of two separate but interrelated stages. First, a trace is mapped onto the time-frequency domain. Then the time-frequency representation is mapped back onto the time domain by an appropriate operation. The computed instantaneous traveltime equals the recording time at those instances at which there is a seismic event, a feature that is used to pick the events. We analyze the concept of the instantaneous traveltime and demonstrate the application of our automatic picking method on dynamite and Vibroseis field data.

INTRODUCTION

Event picking is an important step in seismic processing. It is used in static corrections, velocity analysis, seismic tomography, amplitude versus offset (AVO) analysis, and geological interpretation. By event, here, we mean a lineup on a number of traces of a seismic record that indicates the arrival of new seismic energy. The arrival of such new seismic energy is denoted by a discontinuity in the values of one or more attributes that characterize the various layers of the subsurface.

The recognition of seismic events is usually based on some measure of coherency or similarity from trace to trace (Marfurt et al., 1998; Bienati and Spagnolini, 1998). The underlying assumption is that when a wave reaches the receiver line, it will produce approximately the same effect on all neighboring receivers. If the wave is strong enough to override other energy arriving at the same time, the traces will look similar during the interval in which this wave arrives. Therefore, coherence is considered a necessary condition for the recognition of any event.

Image processing techniques are also very popular for event picking (Bondár, 1992). Seismic sections are considered as images and seismic events can be thought of as edges on the seismic image. Edge detection or edge linking algorithms are therefore used to detect events usually after edge-preserving filtering (Bondár, 1992) or multiresolution analysis (Maroni et al., 2001) of the image. Other features used to

***e-mail:** tkhalfah@kacst.edu.sa, sergey@sep.stanford.edu

recognize seismic events are amplitude standout, which refers to an increase in amplitude due to the arrival of coherent energy, wave signature, dip moveout and normal moveout (Garotta, 1971).

In this paper, we propose a new methodology for automatic event picking based on a new attribute of seismic signals, which we call instantaneous traveltime. Our approach is based on the assumption that a recorded trace consists of the superposition of sufficiently concentrated signals that arrive at different times. A time-frequency decomposition allows the separation of those signals and the calculation of the traveltimes of different events within a trace. The computed traveltimes are initially time and frequency dependent but the dependency on the frequency is dropped by an appropriate operator. Testing this approach on simple synthetic and field data examples reveals its properties and shows promising results for automated seismic event picking.

METHODOLOGY

The approach utilizes a number of signal analysis techniques both in the time and frequency domains. We describe them below.

The mean and instantaneous traveltime attributes

We first define the quantity $\tau(\omega)$ for a signal $u(t)$ as

$$\tau(\omega) := \mathrm{Im}\left\{\frac{\frac{dU(\omega)}{d\omega}}{U(\omega)}\right\}, \tag{1}$$

where U is the Fourier transform of $u(t)$ and $\mathrm{Im}\{\,\}$ denotes the imaginary part. The rationale behind this seemingly arbitrary definition is that for the ideal case in which $u(t)$ is a delta function occurring at time t_0, i.e. $u(t) = a\delta(t - t_0)$, $\tau(\omega)$ equals the time of occurrence of the delta function for all frequencies, namely $\tau(\omega) = t_0$.

If $u(t)$ is a band-limited delta function, then $\tau(\omega)$ does not equal t_0 but rather is approximately equal to t_0, within the bandwidth of $u(t)$ (see Figure 1(a)). Consequently, the dependence of $\tau(\omega)$ on frequency can be dropped by simply averaging $\tau(\omega)$ within the bandwidth of $u(t)$. In the case that $u(t)$ is indeed a signal that signifies an event, such as the band-limited spike of Figure 1(a), averaging over the frequencies within the bandwidth of the signal yields a meaningful number, namely the time of occurrence of the event. On the other hand, if $u(t)$ is random noise or even insufficiently spiky, then $\tau(\omega)$ varies considerably with frequency (Figures 1(b), 1(c)). In this case, averaging of $\tau(\omega)$ yields a meaningless number. This feature can be used to identify events in the seismic data.

The quantity $\tau(\omega)$ is essentially the derivative of the phase of $U(\omega)$ with respect to frequency, also referred to as group delay or envelope delay. In fact it has been used

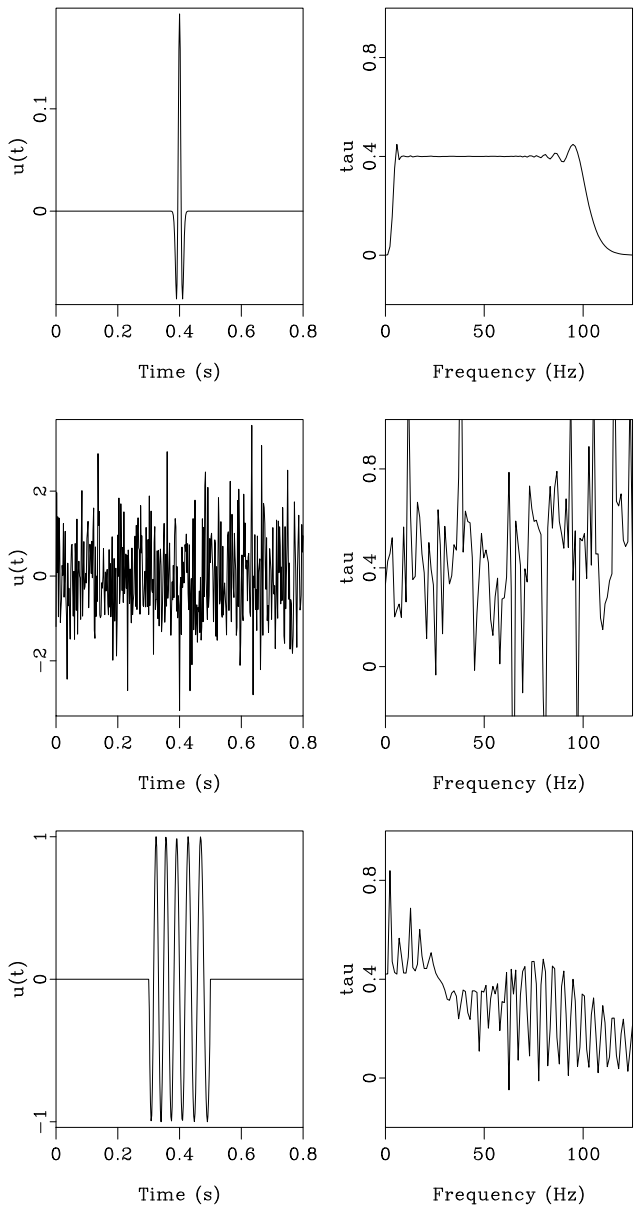

Figure 1: Various signals (left) and their mean traveltimes as a function of frequency (right). (a) Band-limited spike. (b) Random noise. (c) Quasi-sinusoid (simulates Vibroseis harmonics). itime/syn rick,noiz,chrp

as such by Stoffa et al. (1974) to compute a continuous phase curve and circumvent the phase-wrapping problem in homomorphic deconvolution. However, we prefer to use the term traveltime for reasons that are explained below.

If we assume a signal consisting of two spikes at t_1 and t_2, respectively, i.e., $u(t) = a_1\delta(t-t_1) + a_2\delta(t-t_2)$, we get

$$\mathrm{Im}\left\{\frac{\frac{dU}{d\omega}}{U}\right\} = \lambda_1 t_1 + \lambda_2 t_2, \tag{2}$$

where λ_1, λ_2 are coefficients that depend on ω, a_1, a_2 and $t_2 - t_1$ and $\lambda_1 + \lambda_2 = 1$. In general, for a signal $u(t) = \sum a_n \delta(t-t_n)$, then

$$\tau(\omega) := \mathrm{Im}\left\{\frac{\frac{dU}{d\omega}}{U}\right\} = \sum_n \lambda_n(\omega) t_n, \tag{3}$$

where $\sum \lambda_n(\omega) = 1$. In other words, $\tau(\omega)$ is a weighted sum of the times of arrivals of the different signals. By dropping the dependence on the frequency, we get the mean traveltime of the arrivals of $u(t)$. We note that the calculation of the derivative $\frac{dU}{d\omega}$ can be unstable for sharp variations with frequency. It is therefore preferable to compute this quantity as the Fourier transform of $itu(t)$. In addition, it is generally a good idea to employ some kind of smooth division (for instance, like the one described by Fomel (2007a)) when dividing $\frac{dU}{d\omega}$ over U to avoid instability caused by small values of $U(\omega)$.

From the above discussion, it is clear that the mean traveltime attribute is not much of use, if it is to be computed on the whole trace. The Fourier transform used in equation 1 performs an integration over the observed time interval. The localized temporal information is therefore lost. What is needed is a time-frequency transform to replace the Fourier transform in equation 1 such that the traveltime attribute becomes localized in time as well. In this way, different arrivals are isolated from one another and the computed traveltimes are more accurate. The instantaneous traveltime $\tau(t)$ is therefore defined as

$$\tau(t) := \mathcal{S}_\omega\left[\mathrm{Im}\left\{\frac{\frac{\partial U(t,\omega)}{\partial\omega}}{U(t,\omega)}\right\}\right], \tag{4}$$

where $U(t,\omega)$ now denotes an appropriate time-frequency transform and $\mathcal{S}_\omega$ is an appropriate operator or mapping from the frequency domain into a single number. In the above definition, we intentionally let the time-frequency transform as well as the mapping $\mathcal{S}_\omega$ undefined as different transforms and/or operators may be more effective depending on the type of data under examination. We also note that only the forward transform is employed in equation 4 and not the inverse. This allows for more flexibility on the choice of the transform used to capture the nonstationary behavior of the seismic traces as the transform need not have an inverse.

In the next two subsections, we discuss these two issues, namely the choices of the time-frequency transform and the mapping operator.

Time-frequency transform

In principle any time-frequency representation can be used for the calculation of the instantaneous traveltime. An obvious choice is the short-time Fourier transform. However the short-time Fourier transform suffers from the time-frequency resolution limitation and therefore the length of the window used for its calculation significantly depends on the frequency content of the windowed data. It is therefore not appropriate for our problem.

Another alternative is provided by Liu et al. (2011). Their method essentially computes a series representation of a nonstationary, temporally bounded signal using the same basis functions as the Fourier series. This series representation is therefore similar to the Fourier series, however, the series coefficients are allowed to be time-varying.

In particular, if $\phi_k(t) = e^{ik\omega_0 t}$ denote the basis functions of the Fourier series expansion for a signal $s(t)$ with support $T = \frac{2\pi}{\omega_0}$, then $s(t)$ is represented as

$$s(t) \sim \sum_k c_k \phi_k(t), \tag{5}$$

where $c_k = \frac{\langle s,\phi_k \rangle}{\langle \phi_k,\phi_k \rangle}$ and $\langle x, y \rangle$ denotes the usual dot product of the $\mathbb{L}_2$ space of functions with period T.

We note that equation 5 is equivalent to the $\mathbb{L}_2$-minimization problem:

$$\min_{\{c_k\}} \quad \int_T |s(t) - \sum_k c_k \phi_k(t)|^2 \, dt. \tag{6}$$

Instead of using equation 6 to calculate constant Fourier series coefficients, Liu et al. (2011) calculate time-varying coefficients, $c_k(t)$, which are the solution of the $\mathbb{L}_2$-minimization problem:

$$\min_{\{c_k(t)\}} \quad \sum_k \int_T |s(t) - c_k(t)\phi_k(t)|^2 \, dt. \tag{7}$$

Apart from the time-varying character of the coefficients, $c_k(t)$, in equation 7, equations 6 and 7 are also different in another significant way: in equation 6, the minimization is performed between the signal and its series representation, while in equation 7, the minimization is performed between the signal and every frequency component separately.

The coefficients, $c_k(t)$, can be computed by solving the regularized least-squares problem:

$$\min_{\{c_k(t)\}} \quad \sum_k \int_T |s(t) - c_k(t)\phi_k(t)|^2 \, dt + R(c_k(t)), \tag{8}$$

where R is the regularization operator (Liu et al., 2011). Using such an approach enforces smoothness on the coefficients, $c_k(t)$, which ensures the solution of the underdetermined problem 7 (Fomel, 2007b).

The mapping operator

To illustrate the effect the mapping operator has on the computation of the instantaneous traveltime, we use the simple synthetic signal shown in Figure 2(a). This signal consists of three events at 0.4, 1.2 and 1.4 s. Figures 2(b) and 2(c) depict the time frequency representation of the test signal using the formulation of equation 8 and the computed τ as a function of time and frequency. It is evident that for a significant part of the frequency band, $\tau(t,\omega)$ is a smooth function of ω; in fact, it is almost constant. In particular, the three curves at about 0.4, 1.2 and 1.4 s are contour lines of $\tau(t,\omega) = t$. This means that for this particular time-frequency transformation, the mapping operator can be a simple averaging operator. It would be prudent, however, to average $\tau(t,\omega)$ over the frequencies in the bandwidth of the signal.

For most data, the bandwidth of signals is varying with time. It therefore makes sense to estimate the effective bandwidth as a function of time. In order to choose the frequency band automatically, we suggest any data-driven criterion, such as an estimate of the instantaneous frequency or some weighted mean of the frequency. An obvious choice is

$$\mu_\omega(t) = \frac{\int \omega |c(t,\omega)|\, d\omega}{\int |c(t,\omega)|\, d\omega}, \tag{9}$$

where $c(t,\omega)$ are the time- and frequency-varying coefficients of the time-frequency transform, which we call local frequency. Equation 9 has been used by Lovell et al. (1993) as an estimate of the instantaneous frequency (Taner et al., 1979; Barnes, 1992) or the dominant frequency (Liu et al., 2011). Similarly, we can define an estimate of the variance of the local frequency as

$$\sigma_\omega^2(t) = \frac{\int (\omega - \mu_\omega(t))^2 |c(t,\omega)|\, d\omega}{\int |c(t,\omega)|\, d\omega} \tag{10}$$

Having estimated the local frequency, $\mu_\omega(t)$, and its variance, $\sigma_\omega^2(t)$, we may now estimate the effective bandwidth, $\mathrm{BW}(t)$, as

$$\mathrm{BW}(t) = [\mu_\omega(t) - \sigma_\omega(t), \mu_\omega(t) + \sigma_\omega(t)]. \tag{11}$$

In Figures 2(b) and 2(c), the dashed lines denote the effective bandwidth.

The result of the averaging operation is shown in Figure 3(b), in which $\tau(t,\omega)$ is averaged over the frequencies in its effective bandwidth. (Figure 3(a) is the same as Figure 2(a) and shown here just to illustrate the agreement between the actual arrivals and the picked arrivals.) Parameter $\tau(t)$ equals the recording t (dashed line) at the times of arrival of the spikes, namely at $t_1 = 0.3996$, 1.1991 and 1.3978 s. It should be noted that although there are actually no arrivals between two consecutive arrivals, $\tau(t)$ is not zero in that interval. This is due to the smooth division we

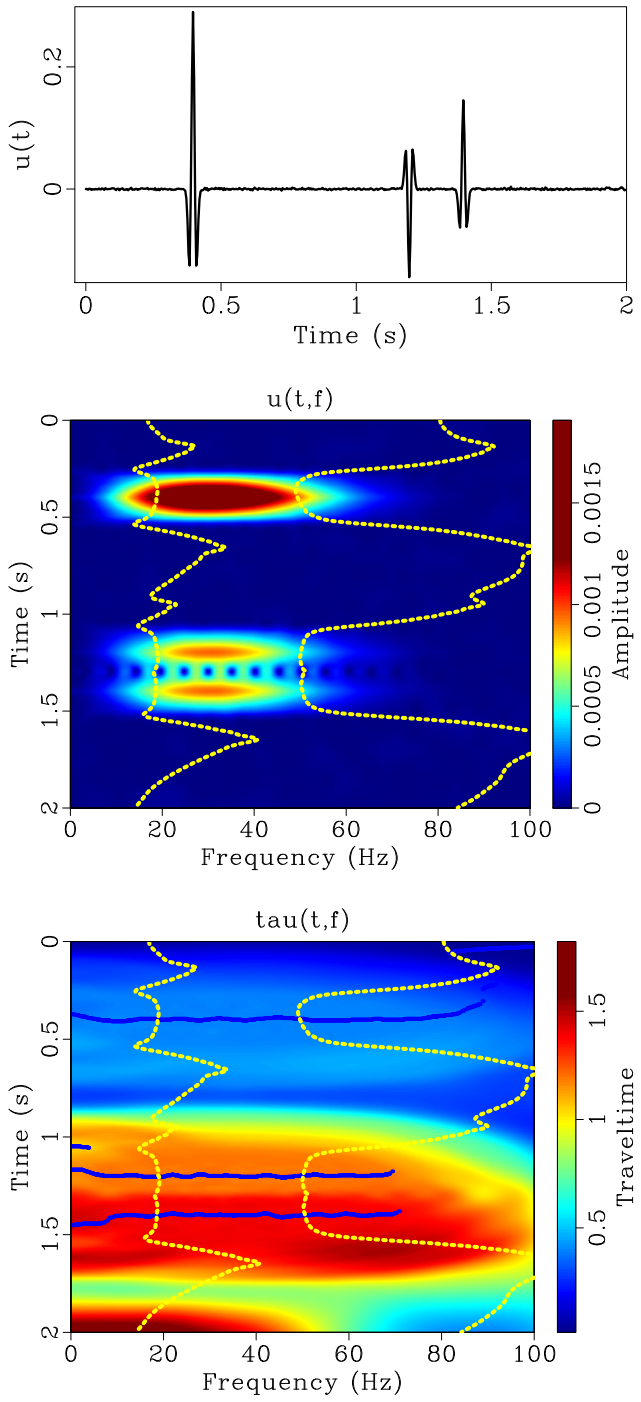

Figure 2: (a) Synthetic signal. (b) Local $t-f$ representation of the synthetic signal. (c) $\tau(t,f)$ using the local $t-f$ map. Contour lines denote values where $\tau(t,f)=t$ and the transition through zero is from positive to negative values.
The dashed lines in (b) and (c) indicate the effective bandwidth (estimated using equation 11). itime/syn syn,ltf0,tt0

employed, when dividing $\frac{dU}{d\omega}$ over U. Smooth division does not allow the result to vary erratically from sample to sample. Figure 3(c) shows the difference $\tau(t)-t$. This difference equals 0 at the times of arrival of the two spikes. However not all zeros of $\tau(t)-t$ are of interest; rather, only the zero crossings from positive to negative values yield valid traveltimes. Positive maxima of $\tau(t)-t$ (as in $t \approx 0.3, 1.1, 1.3$) denote an imminent arrival of a signal. Let's assume a strong (compared to neighboring events) event at some time t_0. According to equation 3, $\tau(t)$ is a weighted some of the times of arrivals around t. The closer t is to the imminent arrival at $t_0 > t$, the more the value of $\tau(t)$ will be biased towards the value t_0. Therefore $\tau(t)$ will be greater than t, i.e., $t < \tau(t) < t_0$. For $t > t_0$, the value of $\tau(t)$ will still be biased towards t_0, therefore $t_0 < \tau(t) < t$. In fact, the higher the energy of the arriving signal at some time t_0 compared with that of neighboring events, the closer the value of $\tau(t_0)$ to t_0 will be. Accordingly, an event is identified by the non-zero values of the function

$$d(t) = H\left(-\frac{d\tau}{dt}\right)\delta(t-\tau(t)), \tag{12}$$

where H is the Heaviside step function and δ is the Dirac delta. This function is zero if $\tau(t) \neq t$ as imposed by the Dirac delta factor as well as if $\tau(t) = t$ but $\tau(t)$ is increasing as imposed by the Heaviside step factor.

APPLICATION TO FIELD DATA

We used the instantaneous traveltime attribute to pick events from two field datasets. The first dataset is dataset 6 from Yilmaz (2001) shown in Figure 4. This is a 48-trace shot gather with 100 m trace spacing and sampling interval 4 ms. The source used to acquire this dataset was dynamite. We applied the proposed method to the raw data without performing any type of preprocessing to evaluate our method's behavior and consistency across offsets in raw and noisy data. Indeed, there are more than one different refraction arrivals close to the first breaks like the strong linear event with a velocity of about 1.5 km/s, which looks like a refraction from a deeper layer, and two reflections at about 1.5 s and 2.7 s. The arrivals computed using the instantaneous traveltime attribute are shown as red spikes in the figure.

In this application, we effectively applied an automatic picking tool to raw two-dimensional seismic data without imposing any consistency requirements over offset. Our objective was to measure the capability of this attribute in mapping reflections. The figure shows that the instantaneous traveltime attribute misses many of the first breaks due to the complexity of the waveforms of the early arrivals. The proposed method is therefore not suitable for picking first breaks, although the instantaneous traveltime can be used for automatic first-break picking, if applied appropriately (Saragiotis and Alkhalifah, 2012). Nevertheless, the first reflection is clearly well picked at most traces as is the 1.5 km/s refraction. The second reflection is picked only at traces 18 to 30. Overall, the trends of the different arrivals are present in Figure 4 despite the raw nature of the data.

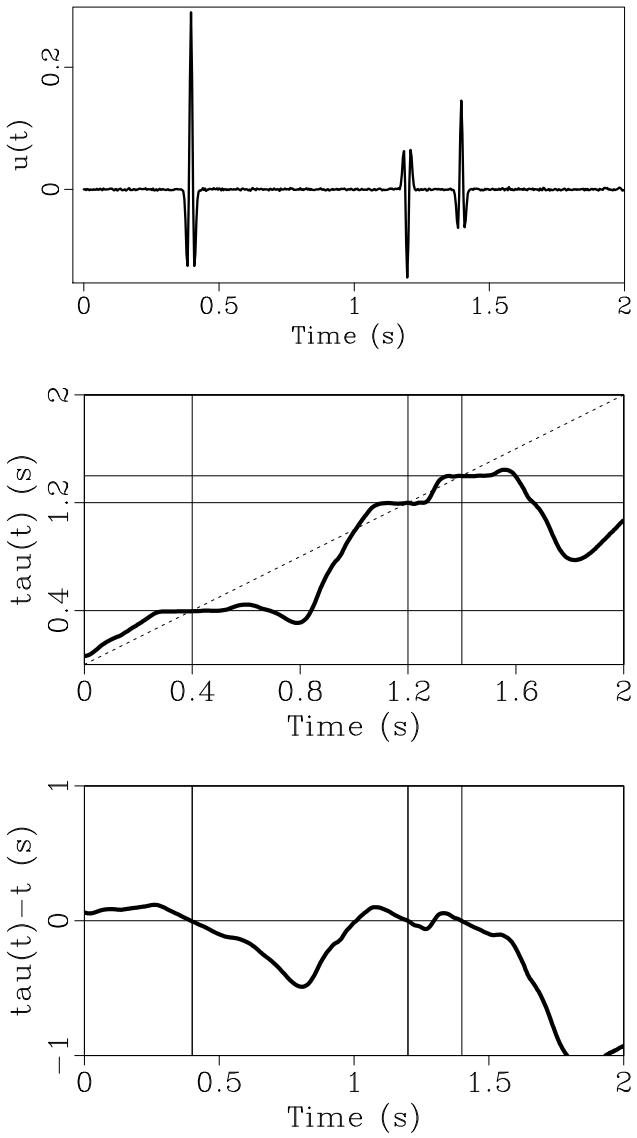

Figure 3: (a) Synthetic signal (sampling period is 4 ms). Arrivals are at 0.4, 1.2 and 1.4 s. (b) $\tau(t)$ after averaging over the frequencies in the effective bandwidth. The dashed line indicates the recording time. (c) $\tau(t) - t$. Zero crossings occur at 0.3996, 1.1991 and 1.3978 s. itime/syn syn0,taut0,tau-t0

The second dataset is dataset 2 from Yilmaz (2001) and is shown in Figure . It is a 120-trace shot gather with 100 ft trace spacing and sampling interval 4ms. The source used to acquire this dataset is Vibroseis. Regarding this second dataset, we can make almost the same remarks as about the first one. Although the first breaks are identified, they are not accurately determined. As mentioned previously, first breaks can be identified accurately even in Vibroseis data (Saragiotis and Alkhalifah, 2012). However, other events are properly picked, including the reflections at about 1.5 and 1.8 s.

We reiterate that for both datasets, picking is performed without any preprocessing of the data and by applying the method to each trace separately, without taking into account information from neighboring traces. Such information is expected to enhance the picking performance significantly and is the subject of ongoing research.

Finally, the computational efficiency of the proposed method depends largely on the computational efficiency of the time-frequency transform and the operator that maps the time-frequency domain to the time domain. The algorithm by Liu et al. (2011) has the advantage of being easily parallelizable. Recently, efficient algorithms for computing time-frequency transforms, as for example in (Brown et al., 2010), have been introduced. Such efficient algorithms are expected to increase the computational efficiency of the proposed method.

Dataset 6 from (Yilmaz, 2001) and picked events (red). For displaying purposes, AGC has been applied on the data.

CONCLUSIONS

We have presented a novel approach to automatic event picking in seismic data. This method does not require a specification of optimal empirical parameters, such as window lengths or reference waveforms. It is based on the instantaneous traveltime, a new attribute. The instantaneous traveltime is computed from the seismic data by first transforming the data into a time-frequency domain to capture the nonstationary behavior of the data. Then, the time-frequency representation of the data is mapped back onto the time domain. The time-frequency transform as well as the mapping operation may be chosen depending on the data at hand. Furthermore, the time-frequency transform need not have an exact inverse transform, a fact which allows for a wider range of choices on such transforms.

We have applied this approach to synthetic and field data (dynamite and Vibroseis) to investigate the behavior of the algorithm. We find that its performance is promising. Although the presented method cannot be used for first-break picking per se, the instantaneous traveltime attribute can be used for such a task. To improve the accuracy of the proposed method, information on adjacent traces may be used to further constrain the event-picking and/or edge-linking algorithms.

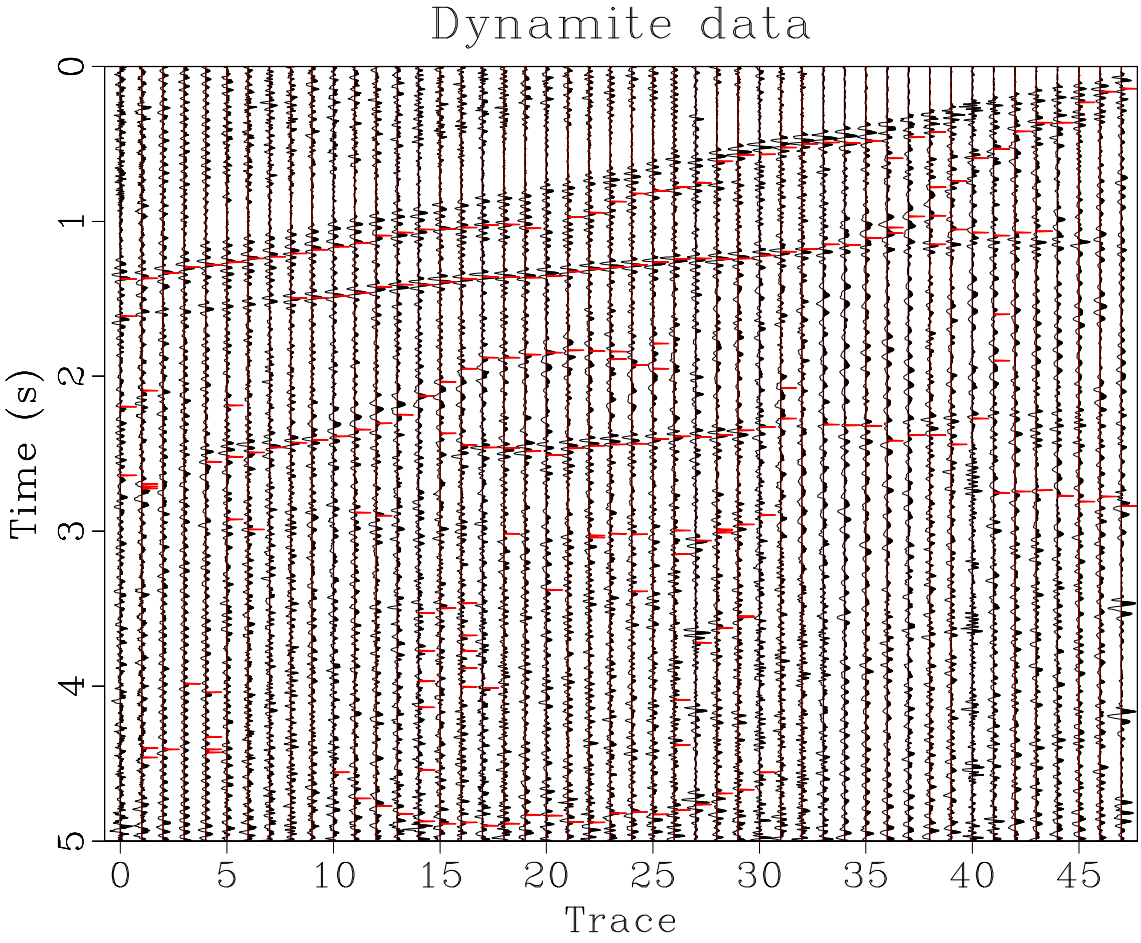

Figure 4: oz6 itime/oz6 oz6

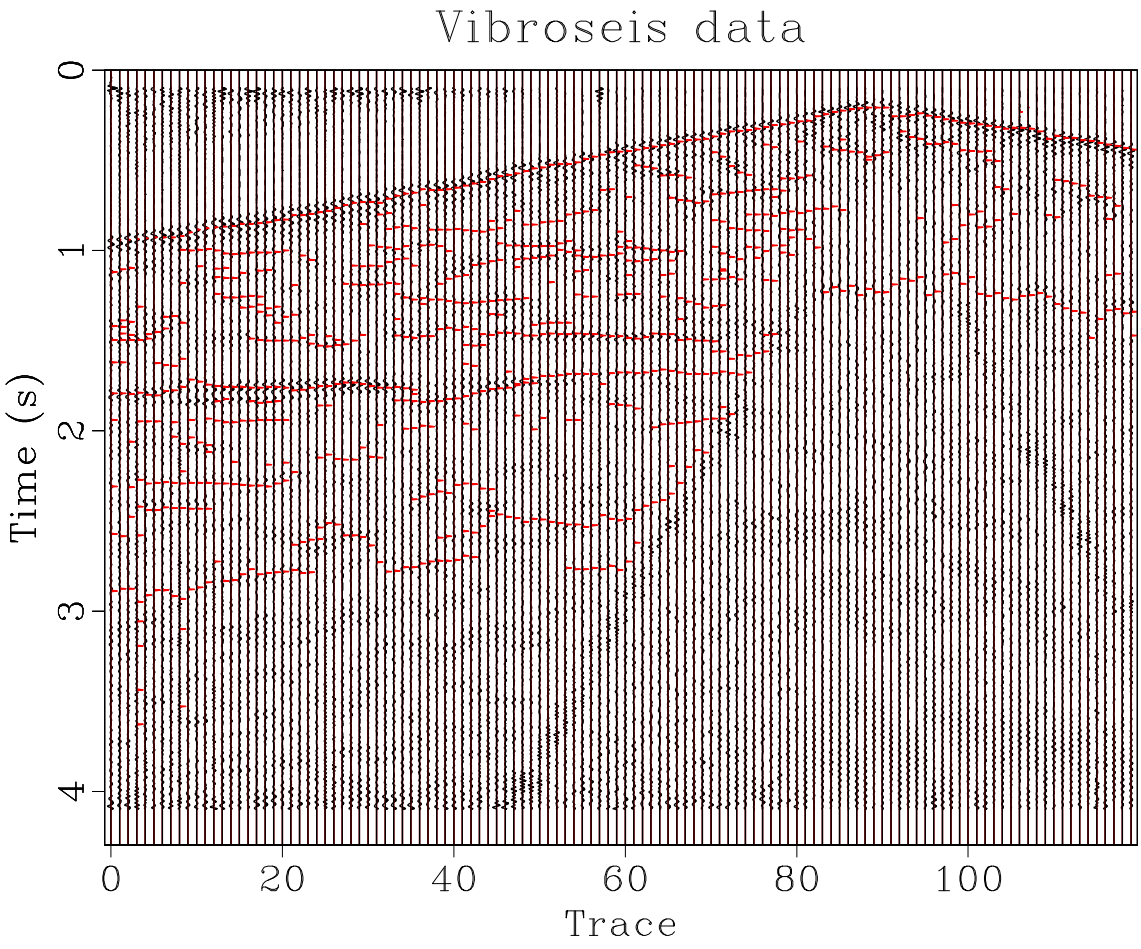

Figure 5: Dataset 2 from (Yilmaz, 2001) and picked events (red). For displaying purposes, AGC has been applied on the data. itime/oz2 oz2

ACKNOWLEDGMENTS

We would like to thank Yunseok Choi and Mohammed A. Zuberi for useful discussions. We also thank the King Abdullah University of Science and Technology for its financial support. This work was partially funded by Saudi Aramco, under Project FSD-016/2010.

REFERENCES

Barnes, A. E., 1992, The calculation of instantaneous frequency and instantaneous bandwidth: Geophysics, **57**, 1520–1524.

Bienati, N., and U. Spagnolini, 1998, Traveltime picking in 3D data volumes: 60th EAGE Conference & Exhibition, Extended Abstracts.

Bondár, I., 1992, Seismic horizon detection using image processing algorithms: Geophysical Prospecting, **40**, 785–800.

Brown, R. A., M. L. Lauzon, and R. Frayne, 2010, A general description of linear time-frequency transforms and formulation of a fast, invertible transform that samples the continuous S-transform spectrum nonredundantly: Signal Processing, IEEE Transactions on, **58**, 281–290.

Fomel, S., 2007a, Local seismic attributes: Geophysics, **72**, A29–A33.

———, 2007b, Shaping regularization in geophysical-estimation problems: Geophysics, **72**, R29–R36.

Garotta, R., 1971, Selection of seismic picking based upon the dip, move-out and amplitude of each event: Geophysical Prospecting, **19**, 357–370.

Liu, G., S. Fomel, and X. Chen, 2011, Time-frequency analysis of seismic data using local attributes: Geophysics, **76**, P23–P34.

Lovell, B. C., R. C. Williamson, and B. Boashash, 1993, The relationship between instantaneous frequency and time-frequency representations: Signal Processing, IEEE Transactions on, **41**, 1458–1461.

Marfurt, K. J., R. L. Kirlin, S. L. Farmer, and M. S. Bahorich, 1998, 3-D seismic attributes using a semblance-based coherency algorithm: Geophysics, **63**, 1150–1165.

Maroni, C. S., A. Quinquis, and S. Vinson, 2001, Horizon picking on subbottom profiles using multiresolution analysis: Digital Signal Processing, **11**, 269–287.

Saragiotis, C., and T. Alkhalifah, 2012, Automatic first break picking using the instantaneous traveltime attribute: 74th EAGE Conference & Exhibition, Extended Abstracts.

Stoffa, P. L., P. Buhl, and G. M. Bryan, 1974, The application of homomorphic deconvolution to shallow-water marine seismology — Part I: Models: Geophysics, **39**, 401–415.

Taner, M. T., F. Koehler, and R. E. Sheriff, 1979, Complex seismic trace analysis: Geophysics, **44**, 1041–1063.

Yilmaz, O., 2001, Seismic data analysis: Processing, inversion and interpretation of seismic data: SEG, volume **10** *of* Investigations in Geophysics.